POLITECNICO DI TORINO

Collegio di Ingegneria Chimica e dei Materiali

**Master of Science Course
in Materials Engineering for Industry 4.0**

Master of Science Thesis

Additive Manufacturing of Metallic Aircraft Spare Parts to Enhance Logistic Support

Supervisors

Alberta Aversa

Sara Biamino

Emilio Bassini

Company supervisor

Mathieu Terner

Candidate

Andrea Pochettino

December 2024

"An optimist will tell you the glass is half-full;
the pessimist, half-empty;
and the engineer will tell you the glass is twice the size it needs to be"
(Oscar Wilde)

Abstract

Leonardo is a global industrial group that builds technological capabilities in Aerospace, Defence & Security. In particular, the Customer Support of Leonardo's Aircraft Division is always attentive to the development of innovative solutions leveraging disruptive technologies to meet customer needs. Logistic Support and in particular the readiness of spare sparts is one of the critical factors to maximize aircraft availability. For this reason, there has been increasing interest in recent years on the utilization of Additive Manufacturing (AM) for the production of spare parts taking advantage on the flexibility of these technologies for manufacturing a wide variety of components on-demand. This master's thesis work studied the production by Laser Powder Bed Fusion (LPBF) of metallic components from several Leonardo's aircraft platforms and a deep characterization of the materials properties was carried out. Possible candidates for AM production are defined by several parameters to assess feasibility from a manufacturing standpoint and suitability from a logistic standpoint. An aluminum bracket, characterized by significant challenges in the supply chain, from the Main Landing Gear of the multi-mission transport C-27J aircraft was first selected. While the conventional material is not adapted to LPBF, the substitution with the attractive AlSi10Mg alloy was found encouraging. Two other components in LPBF favorite Ti-6Al-4V were also selected from the Advanced Jet Trainers' family of Leonardo: a complex clevis from the Environmental Control System of the M-346 and a connector to the hydraulic accumulator of the Leading Edge Flap Actuation System of the M-345. The complete characterization showed that the materials produced by LPBF had better mechanical properties than their conventionally wrought counterpart. In all the cases a series of prototypes together with control specimens were produced on an EOS M270 at the Integrated Additive Manufacturing infrastructure of Politecnico di Torino. Stress relieving treatments as well as aging were carried out. Specimens were prepared by standard metallographic procedures and porosity and microstructure were verified. Roughness was measured and accurate control of the dimensions was compared to the conventional parts. Standard specimens for tensile tests were also prepared and the mechanical properties were compared to design requirements. All results were conscientiously reported, discussed and suggested that Additive Manufacturing could be integrated in the supply chain of spare parts bringing about great benefits. The analysis presented in this thesis will support the already existing certification path for AM-produced components in Leonardo Aircraft.

Acknowledgments

Here we are, reaching the 'end' of my university journey at the Politecnico di Torino. It has been a difficult and challenging experience, but at the same time a stimulating and rewarding one, which has allowed me to acquire the necessary skills for my future work and, above all, to grow as a person.

Now I would like to express my sincere gratitude to all those who contributed to the completion of this thesis.

First, I would like to thank Leonardo S.p.A. for giving me the opportunity to work in such an important company on the national and international industrial scene. I would like to thank all the members of the Commercial & CSS&T team, Juri Barollo, Barbara Pralio, Andrea Di Filippo, Matteo Caracciolo and Roberto Diperna, who showed me kindness and friendliness. In particular, a big thank you goes to Mathieu Terner, for his thoughtfulness, valuable advice on the subject as a former professor of materials science and also for introducing me to this new reality.

I would like to thank Professors Sara Biamino, Emilio Bassini, and a special tribute goes to Alberta Aversa, who has been an absolute point of reference for me throughout this thesis, always available and very quick to answer all my doubts, who has shown great expertise in the subject and with whom, in addition to immense dedication, we have also shared some funny moments. I also thank all the people I met in the DISAT laboratories, who helped me in the use of scientific instrumentations.

Thanks to all the friends I have known all my life, to all those I met at university, with whom we shared joys and disappointments. You have all supported me and it is thanks to you that I have become what I am today.

Tender and loving thanks go to Sofia, who has given me unwavering support, sweetheart and encouragement during these months.

The sweetest thanks go to my Grandparents for introducing me to the joys of life at an early age. Unfortunately, two of them are no longer here, but I am sure they would be proud of me. With all of you I have shared wonderful moments that I will always carry in my heart.

And first and foremost a huge thank you goes to my Parents, you were the ones who believed in me the most as a student, but more importantly as a person. You are my reference point. I know that you will always be there for me and I will always be there for you.

Summary

List of Figures

List of Tables

List of symbols and acronyms

AM	Additive Manufacturing
AOCP	Aircraft Out of Commission for Parts
AOG	Aircraft on Ground
BCC	Body Centered Cubic
BD	Building Direction
BSD	Back-Scattered Diffraction
EDM	Electrical Discharge Machining
EDS	Energy Dispersive X-ray Spectroscopy
ERP	Enterprise Resource Planning
HCP	Hexagonal Closed Packed
HV	Hardness Vickers
IoT	Internet of Things
LT	Lead Time
MLG	Main Landing Gear
MRO	Maintenance Repair Overhaul
MS	Martensite Start
N	Newton
P%	Porosity percentage
P/N	Part Number
PDU	Power Drive Unit
Rpm	Rounding per minute
SCC	Stress Corrosion Cracking
SEM	Scanning Electron Microscope
SN	Serial Number
STL	Stereolithography standard
STOL	Short Take-Offs and Landings
UTS	Ultimate Tensile Strength
VED	Volumetric Energy Density
WP	Work Packages
YS	Yield Strength

Chapter 1
INTRODUCTION

© Leonardo S.p.A.

1. INTRODUCTION

The adoption of new digital technologies is pushing advanced manufacturing towards the model of 'Factory 4.0', characterized by the integration of multiple factors such as the Internet of Things (IoT), Cloud, 3D Printing, Robotics and Sensing Big Data. This is a well-known phenomenon, which is also gaining ground in Italy, starting with large companies, without any particular sector or market specificities. The innovation and the exploitation of new digital technologies are activities of constant interest also for the Armed Forces and Defence, which do not fail to stimulate and support national suppliers and strategic partners in investments aimed at finding new solutions.

In this big scenario the use of Additive Manufacturing (AM), which belongs to the big family of 3D printing technologies, is considered as a disruptive technology which has the possibility to improve the efficiency in lots of cardinal actual economic fields: defense and aerospace, automotive, biomedical, energy and so on and so forth. All of these industrial sectors, which consider technological development to be one of the priorities of their corporate policy, are increasingly attracted by these new additive manufacturing techniques, as they are able to produce complex near net shape components with high performance and low weight, with minor post processing machining. This could, reduce time-to-market, simplify the supply chain and provide greater flexibility for the company, allowing the production of highly customized objects with more integrated functions and tailored to customer requirements.

In this industrialized world, the ability to reduce prototyping time and actual production time has become crucial for all those hi-tech companies that want to develop products using new technologies in order to gain commercial advantages over their competitors.

It is important to emphasize that AM techniques offer a more conscious use of material, reducing waste and environmental impact compared to traditional subtractive manufacturing techniques. These aspects are becoming increasingly important for the policies of major manufacturing industries, as the recent climate change and raw materials shortage have prompted governments around the world to adopt green policies and the circular economy on a large scale.

Taking into account all these aspects, in recent years, the interest in rapid prototyping and additive manufacturing for metallic materials has increased because these techniques are capable of producing structural components with high mechanical properties, which in some cases are higher than those obtained with traditional techniques.

Specifically, in the military sector, additive technologies are particularly appreciated in the area of Maintenance, Repair and Overhaul (MRO) operations, exploiting the possibility of repairing components and producing tools on site, and in the digitization of the warehouse by exploiting the

possibility of producing objects 'on demand'. Two of the main problems for aircraft industries is the condition of 'Aircraft On Ground' (AOG) that means the airplane is unable to fly due to a technical issue or maintenance problem and 'Aircraft Out of Commission for Parts' (AOCP), describing a situation where the aircraft is non-operational due to the need for replacement parts. These two conditions are critical, as they result in the aircraft being grounded, often unexpectedly, and it is unable to continue its scheduled operation. In particular the AOG is a serious issue principally for the cost associated, that include the cost of replacement parts, labor, loss of revenues or potentially fines, and logistic, such as acquiring the necessary parts, that in most of cases need high lead times (LT), and finding experienced maintainers to fix the problem or in the worst-case scenario shipping parts form other locations, as quickly as possible, sometimes using highly cost charter flights.

AM stands as a solution to each of these problems enabling:

- On-demand and on-time production of spare parts
- Delocalized production of spare parts, possibly close to the end-user
- Reducing costs and delays associated with suppliers and distribution
- Simplify warehouse management.

1.1 Company overview

This thesis project was planned and conducted within a collaboration between Department of Applied Sciences (DISAT) of Politecnico di Torino with Customer Support of Leonardo Aircraft Division in Caselle, Turin, having previously established a mutual collaboration in research and development activities in the field of additive manufacturing, and now applying this topic to the field of logistics support. Leonardo is an Italian leading industrial company and one of the world's top Aerospace, Defence and Security (AD&S) companies, with an integrated range of multi-domain capabilities for military and civil applications. The company operates in the following sectors: aircraft, helicopters, aerostructures, space, unmanned systems and electronics for defence and security. Leonardo Aircraft produces the latest-generation aircraft and provides support to meet the requirements of the most complex operational scenarios: multi-mission defence and surveillance, tactical training and transport, and humanitarian assistance. With more than 30,000 aircraft produced, Leonardo Aircraft delivers and supports high-performance platforms around the world, backed by more than a century of know-how.

The company provides advanced services to support its partners' operational capabilities, maintenance and logistical support through a global network of service centers, and integrated training through simulation systems and live virtual constructive learning environments. Innovation,

continuous research, digital industry and sustainability are the pillars of Leonardo's business in the world.

The creation of the Leonardo Labs is also evidence of Leonardo's strong interest in looking to the future. Leonardo Labs are incubators for the research and development of innovative programs in specific technological areas. They form an ecosystem characterized by close collaboration with research centers, universities, polytechnics, companies and start-ups at a global level. The activities of the Labs have a significant impact on sustainability: from the electrification of helicopters and aircraft to industrial process innovation, and from the analysis of satellite observation data to advanced materials.

Leonardo Aircraft has been working with Additive Manufacturing for several years and has already introduced the technology into production with more than hundreds of parts produced by AM and already flying. At Leonardo Aircraft, additive manufacturing components have been flying on all platforms since 2015 and includes production in metal and polymer. For metal materials, Leonardo recently has signed a five-year contract with BEAMIT [1] to further strengthen the collaboration and supply a number of additively manufactured components over the coming years. Currently, Leonardo has over 100 metal parts qualified, installed and flying on C-27J, M-346 and M-345 platforms.

1.2 Aim of this thesis work

This Master's thesis project has the intention of confirming that AM processes can be effectively exploited from a logistic support point of view, being able to produce components with the required properties. To this end, during this thesis, the feasibility of the additive manufacturing process has been evaluated together with the mechanical and microstructural properties of the components obtained by Laser Powder Bed Fusion (LPBF).

In particular the activity is divides into 4 Work Packages (WP):

1. Job design and optimization for AM production
2. Production of prototypes and control samples via AM
3. Characterization and quality control
4. Study of possible post processing treatments

Each point is discussed in detail in Chapter 2.

1.3 Selection of the use cases

The use of AM technology to produce use cases has the aim of:

- Accelerating the delivery of the component
- Reducing the Aircraft On Ground (AOG) and Aircraft Out Of Commission for Parts (AOCP) events and dependency on suppliers.
- Saving material, energy and cost
- Optimizing resource allocation
- Making able to optimize the design

Certification, regulatory and airworthiness issues require special attention when introducing such innovative and disruptive technology.

The selection of an interesting AM use case is based on four main criteria, sum up in *Table 1.1*

Table 1.1 – 4 main criteria for selecting use cases.

Criteria	Description
(1) Safety	Safety critical / non-safety-critical
(2) Feasibility	Consideration of design and geometry, materials, production volumes and costs
(3) Lead Time (LT)	Time between spare parts order and its delivery to warehouse
(4) Unscheduled Removals Rate (URR)	Number of unscheduled removals (n) over 1000 flight hours $[\frac{n}{1000}]$

(1) The components produced by AM must be non-safety critical, whose failure could not cause significant harm to human life;

(2) AM used for components that would be particularly difficult and expensive to produce via traditional methods; use materials that guarantee the mechanical properties required by the project; be more cost effective than traditional manufacturing for small to medium scale production;

(3) The LT must be over 180 days (LT > 180dd);

(4) The URR must have a value comprised between 2 indices (0.050 < URR < 0.500).

Each aircraft component has a Serial Number (SN) that uniquely identifies it and it is useful for traceability. More generally, the individual component has a Part Number (P/N) that links all components that are the same but different for the SN. Each program, i.e. C-27J, M-346, M-345, has a Parts List Catalogue, a document that lists all the components of the aircraft under a form of Air

Transport Association (ATA) code [2], a standard aviation industry classification system used to categorize and organize all aircraft documentation. This code is useful to obtain information about the item identification of a component on the aircraft. The ATA has a three-level structure:

- First level: two-digit number which represents the major system on the aircraft.
- Second level: two-digit number that represents the component subsystem.
- Third level: two-digit number that represents the component sub-subsystem which provides more details about individual parts and maintenance procedures.

1.3.1　　Aircraft platforms

Among the aircraft platforms proposed by Leonardo Aircraft, three have been focused on in this thesis and for which Use Cases have been selected.

The C-27J (*Figure 1.1*), is a multi-role military transport aircraft featuring advanced avionics and aerodynamic developments for greater efficiency and improved operating performance.

Figure 1.1 – C-27J [3]

The M-346 (*Figure 1.2*) is a jet aircraft optimized for advanced military pilot training, offering a broad range of training capabilities combined with long-term reliability.

Figure 1.2 – M-346 [³]

The M-345 (*Figure 1.3*) is a jet aircraft designed for basic through advanced training of military pilots, equipped with modern avionics and characterized by operating costs comparable to those of a high-powered turboprop trainer.

Figure 1.3 – M-345 [³]

A Use Case has been selected for each of these platforms. Selecting appropriate candidate for AM production, focusing in particular on logistic support consideration, is not easy and several parameters shall be evaluated. As hinted previously, particular attention is paid both on feasibility (the component shall be producible by AM) and on convenience from a logistics standpoint (the component shall present challenges in the present supply chain). It is out of the scope of the present thesis to define accurately the candidate selection criteria and process. Leveraging on a previous Master's thesis work from a fellow student at Politecnico di Torino [4] as well as on the support of the experts within Leonardo Aircraft supported by internal data, Use Cases have therefore been selected and are briefly described in the following.

1.3.2   Bracket from C-27J aircraft

The first use case is a bracket in aluminum mounted on the lower door in the Main Landing Gear (MLG) bay of the C-27J platform (*Figure 1.4*) This part has been identified as "perfect candidate" for production in Additive Manufacturing for several reasons. First and foremost, while it is not safety critical or mission critical structurally, this part presents severe challenges from a logistics standpoint:

- Lead Time > 180 days: this part takes a long time to be supplied;
- Unscheduled Removal Rate (1/1000 FH) ~ 0.1: this part fails and needs to be removed from the aircraft;
- Cause of AOCP: this part must be replaced when failure occurs

This bracket is made of Al 2024-T3, according to specification AMS-QQ-A-250/5.

Discussion with experts in Leonardo from the Structure department of Engineering and from Operative Support of Customer Support highlighted that this part is not particularly solicited during normal conditions. It was not possible for this thesis to find the design requirements in terms of mechanical performance in particular. It is however safe to believe that Al 2024-T3 could be slightly overfit, and that lower mechanical properties could be sufficient. Although Failure and Analysis reports were not available for this thesis, it was assumed that one of the main causes of failure for this part could be an overload during landing. Among the capabilities of the C-27J, which makes it one of the best twin-engine airlifters of its class, is in particular its capability to operate from the most rudimentary airstrips in extreme environmental conditions (*Figure 1.1*). The aircraft is qualified in performing Short Take-Offs and Landings (STOL) on snowy, sandy and unprepared airfields. For this reason, overloading during rough landings can occasionally occur and can be suspected as the main cause of failure for this part. Fatigue properties are therefore hardly relevant and static strength properties are most important.

The above considerations are important because Al 2024, an alloy rich in copper (Cu) as a member of the 2000-series aluminum alloys, is hardly producible by AM. The main reason is the occurrence of hot cracking during the rapid solidification and more generally caused by the typical residual stress which characterized the LPBF process. Therefore, a substitute material shall be considered. As mentioned above, Leonardo Aircraft has introduced AM for years and additively manufactured components have been certified and are flying on most platforms. Leonardo certified in particular the aluminum alloy AlSi10Mg which is particularly attractive for LPBF thanks to a high content of Si which widens the solidification range of the alloy. Though this alloy does not compare favorably to Al 2024, there are reasons to believe that it could be sufficient in the present case.
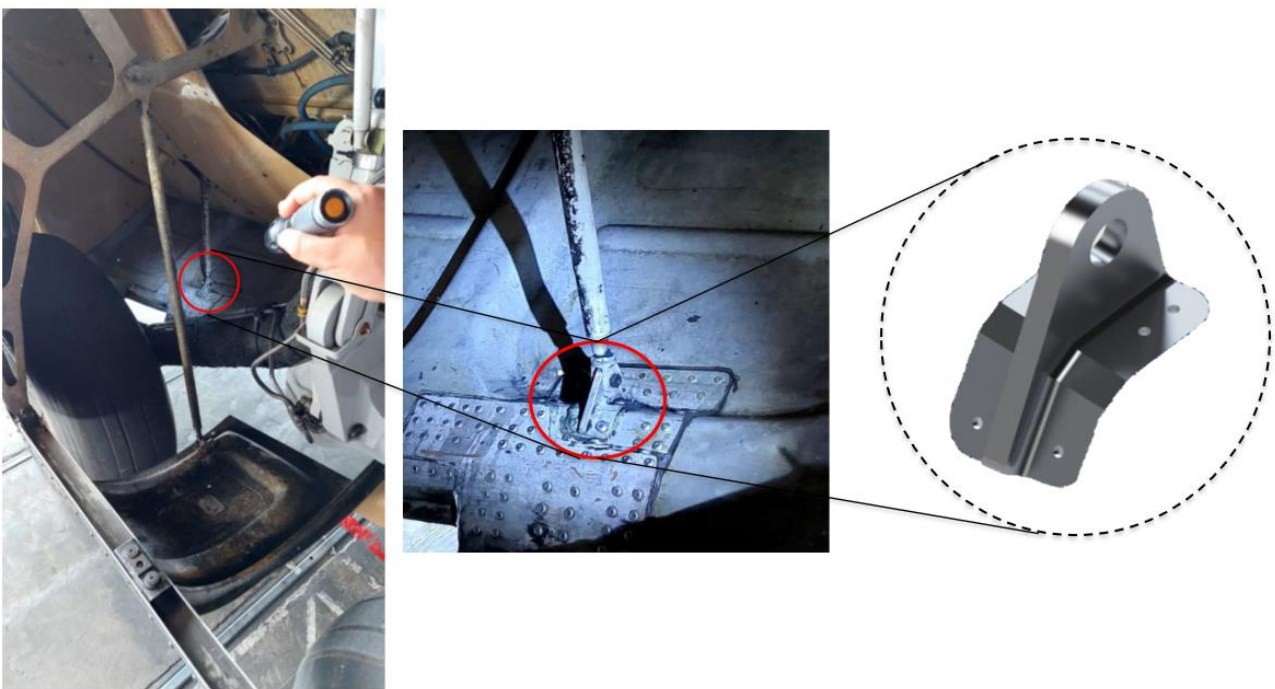
Figure 1.4 – Location of the use case within the main landing gear (© Leonardo S.p.A.).
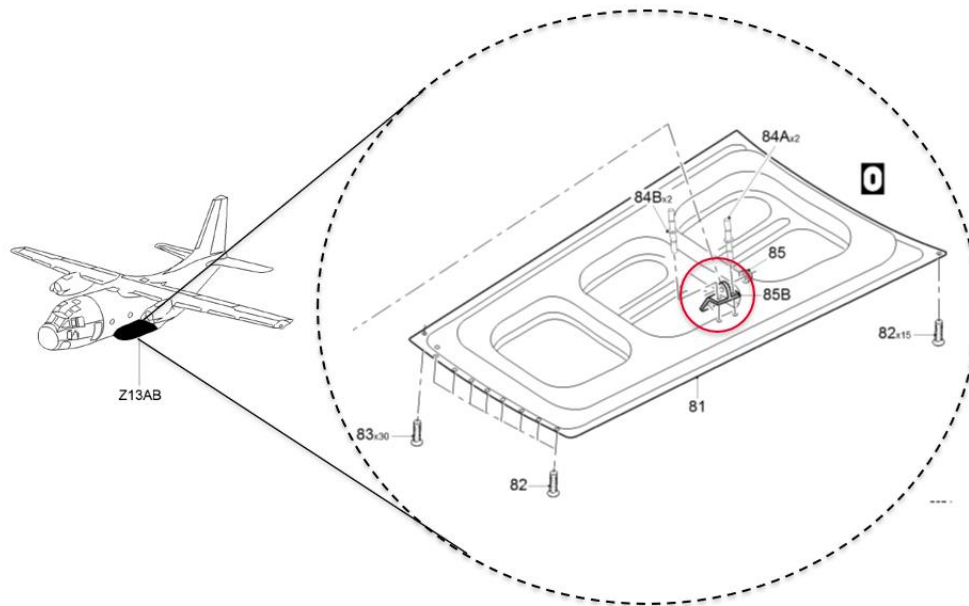
Figure 1.5 – Location of the use case (red circled) within the C-27 J platform (© Leonardo S.p.A.).

1.3.3   Clevis from M-346 aircraft

The second use case is a Clevis in titanium that connects to the fuselage of the aircraft a pipe assembly from the Environmental Control System (ECS) (*Figure 1.6*), a critical system designed to manage and maintain the appropriate environmental conditions for pilots during flight. Similarly to the Bracket, while this part is not structurally critical, it presents challenges from a logistic standpoint such as for example a lead time well over 180 days.

This Clevis is made of the well-known aerospace Ti6Al4V alloy. There is no evidence of failure issues due to significant loads applied of this part. However, as shown in *Figure 1.6*, this part is located in the area surrounding the engines therefore subjected to high temperatures. It could not be confirmed during the thesis but perhaps titanium was selected for this reason.

From a materials and manufacturing process point of view, this use case is interesting because Ti6Al4V is weldable therefore well-suited to the LPBF process which will be discussed in more details in *section 1.6.4*. Moreover, the geometry is similar to that of the Bracket, which presents benefits leveraging complexity-for-free of AM technologies.
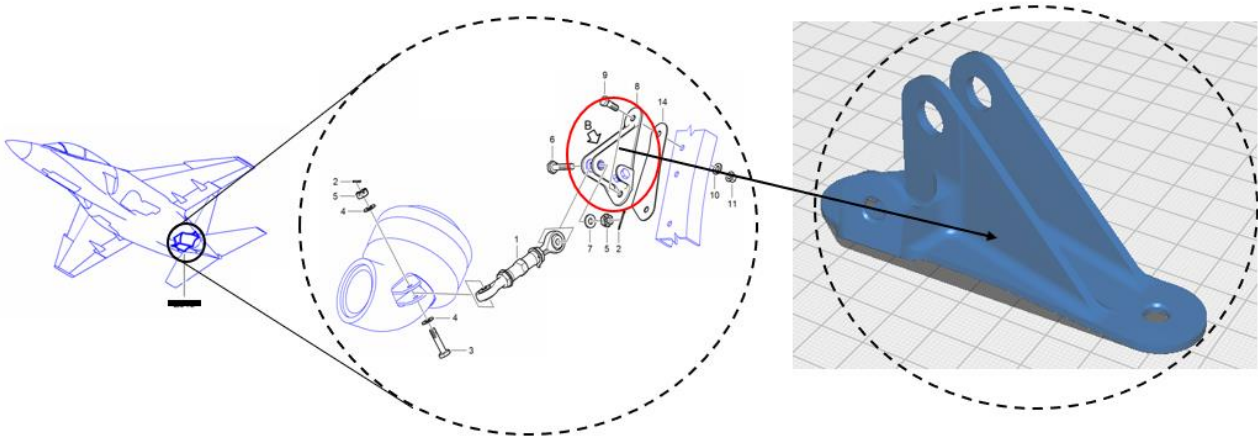
Figure 1.6 – Location of the Clevis within the M-346 platform (© Leonardo S.p.A.).

1.3.4   Connector from M-345 aircraft

The third use case is a Connector also in Ti6Al4V which connects the hydraulic system to the accumulator of the Leading Edge Flap Actuation System (LEFAS) (*Figure 1.7*), a fly by wire electro-hydraulic system that controls the position of the leading edge flap surfaces in response to electrical commands received from the Flight Control Computers (FCCs). In particular, the Power Drive Unit (PDU) of LEFAS receives the hydraulic pressure necessary to actuate the flaps during flight and the presence of an accumulator is necessary to maintain the right pressure within the system. As for the M-346 Clevis, this component suffers from supply chain issues (LT >> 180 days). This connector being integrated within the hydraulic system, it may be subjected to high temperatures, a corrosive atmosphere as well as high loads generated by hydraulic oil reaching pressures as high as to 200 bar, which could explain the use of titanium. Moreover, this cylindrical part (*Figure 1.7*) is yet another shape helpful to attest the capabilities of LPBF.
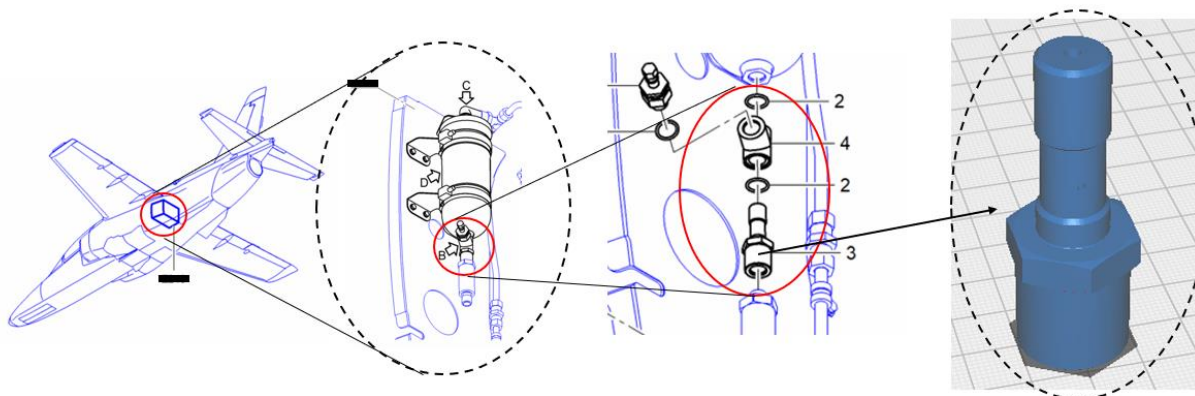
Figure 1.7 – Location of the Connector within the M-345 platform (© Leonardo S.p.A.).

1.4 Additive Manufacturing overview and the Laser Powder Bed Fusion process

The main difference between traditional subtractive methods and additive manufacturing processes is that in the first a tool is used to remove material from a block to achieve the desired shape whereas the latter builds the component layer upon layer. In particular, the second approach allows to produce complex shape components in a single manufacturing step. With AM, it is possible to build a part starting from a 3D model file; after removal from the building platform, the need for post-processing steps is reduced to a minimum so the material waste is close to zero [5]. There are a number of AM technologies available today that differ in how they work, how the layers are deposited to create the part and which materials are used. In particular, the AM technologies can be divided into two macro areas: melting processes and sintering processes (*Figure 1.8*). The aim of this thesis is not to go into the details of all AM technologies, so only the LPBF process, which was used to print the jobs, is discussed in detail.
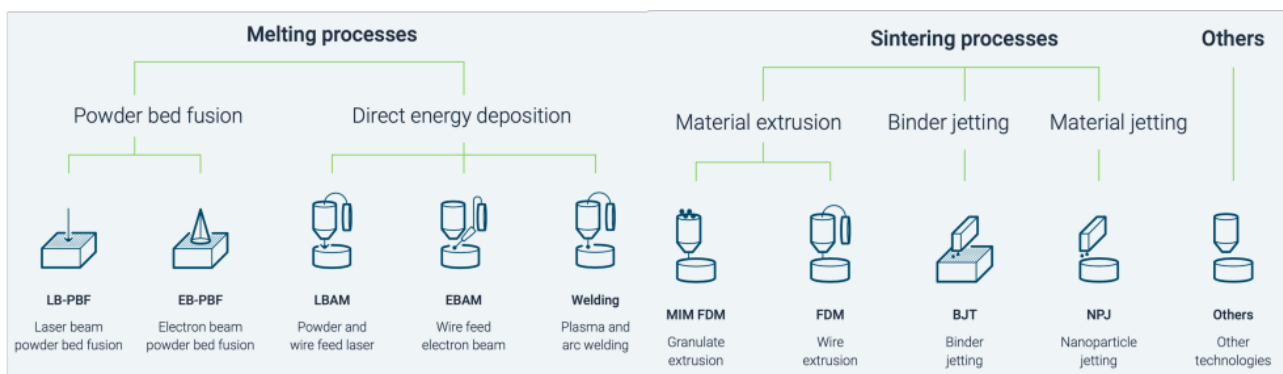
Figure 1.8 – AM technologies overview [6].

1.4.1 LPBF process

The LPBF process is considered to be a very complex process due to the many parameters involved. It is necessary to achieve the correct combination of these parameters during processing to obtain a fully dense part with high mechanical performances [7] . LPBF can be likened to a micro-welding process in which parts are consolidated by successfully joining laser-melted tracks both in the layer plane and in the direction perpendicular to the layer plane. The success of the process is therefore largely dependent on the correct melting and consolidation of the welding tracks [8].

The parameters with the greatest influence on the final properties of the components obtained in the process are:

- *Layer thickness (t)*: thickness of each layer [μm];
- *Hatching spacing (h)*: distance between two adiacent scanning stripes [μm];
- *Scanning speed (v)*: speed of the laser tracks [mm/s];
- *Laser Power (P)*: power of the laser beam [W].

The wrong combination of these parameters can lead to the formation of surface defects and, such as balling, which leads to the formation of spherical droplets instead of smooth tracks or lack of fusion wich is due to the insuficient energy provided to the powder bed. These defects severely affect the quality of the printed parts [9]. Here are a few considerations about these parameters: the layer thickness, which is regulated by the lowering of the build platform, must not be too high to avoid balling phenomena and incomplete melting; hatching spacing with too much overlap can cause the fabrication time to be too long, on the contrary, small overlap can result in not having a dense part; high scanning speed reduces the time of the process but increases the risk of not having a stable melt pool and finally the laser power must not be too low, as enough power is needed to completely melt the powder bed [10].

A schematization of these paramterers on the powder bed is shown in *Figure 1.9.*

The amount of energy for melting a given point is described by the equation of the Volumetric Energy Density (VED):

$$VED = \frac{P}{t \times h \times v}$$

Generally speaking, increasing the VED will increase the density and reduce the porosity of the parts; this is intuitive because the higher the energy, the more the melting and therefore the powder consolidation. However, too high energy density can lead to significant defects such as turbulent melt pool, sputtering of light elements, keyhole pores, high residual stresses that create microcracks [8].
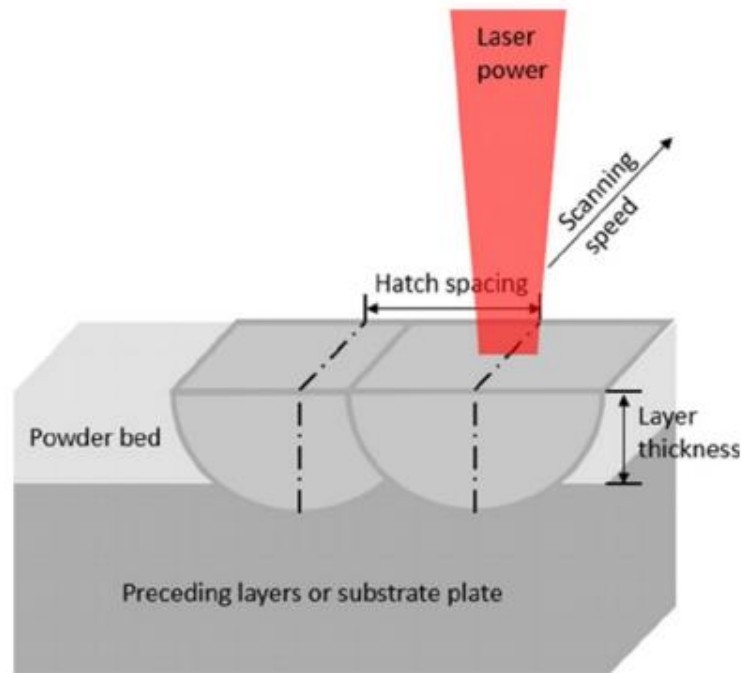
Figure 1.9 – Representation of the main printing parameters in LPBF process: layer thickness (t), hatching spaces (h), scanning speed (v), laser power (P). [10]

1.4.1.1   LPBF building chamber

The chamber inside an LPBF machine is a controlled environment specifically designed to facilitate the process of layer-by-layer melting of metal powders. *Figure 1.10* shows the configuration of the building chamber.
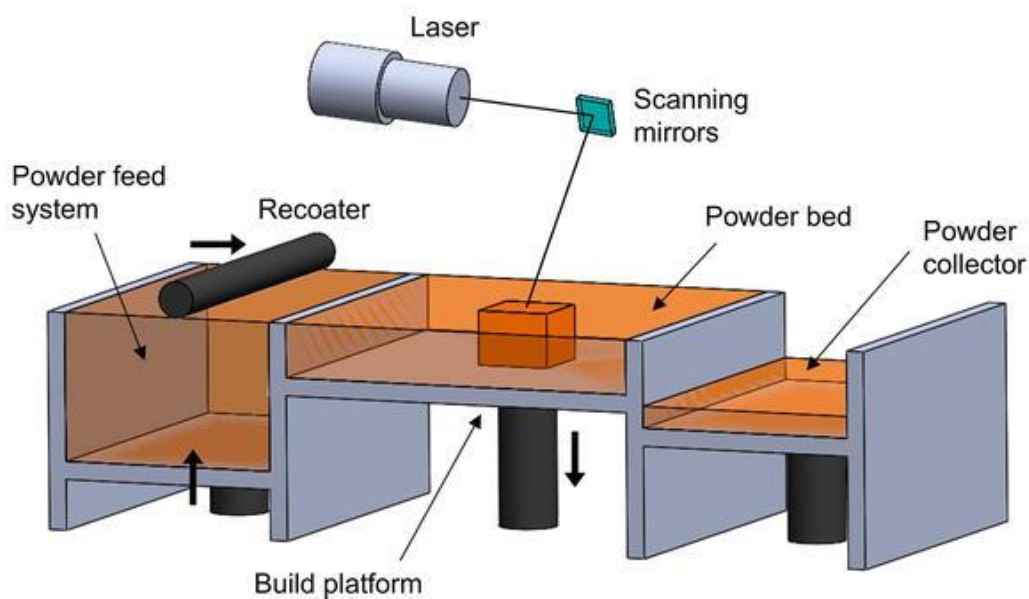
Figure 1.10 – LPBF building chamber layout. [11]

Here are the main components of the chamber.

- *Dispenser platform*: space filled by the row powders. The platform rises during the process.
- *Building platform*: space where the layers of powder are spread and the job is built. It lowers after each layer is fused and so it is ready for the next layer of powder. It can include a heating system to preheat the platform.
- *Collector platform*: the space where the unmolten powder is collected, it becomes used powder and it can be reused for another job.
- *Recoater blade* (*Figure 1.11*) moves the powder from the dispenser platform to the build platform. It can be made of carbon fibers or steel material.
- *Laser system*: consists of a high-power fibre laser, usually Yb fibre, a complex system of mirrors and lenses to direct the laser beam precisely to the powder layer according to the digital file.
- *Atmosphere system* (*Figure 1.12*) an inert atmosphere (Ar or N_2) is created and sensors control the amount of oxygen during the process.
- *Cooling system*: the chamber and components are equipped with cooling systems to dissipate the heat generated.

Figure 1.11 – Recoater blade (red circled).   *Figure 1.12 – The oxygen sensors (red circled)*

1.4.1.2   General process by which to operate the machine

Loading the LPBF machine with metal powders is a critical process and must be done correctly to ensure the quality of the printed job and to ensure operator safety. Here are the main steps that must be followed:

- Wear Personal Protective Equipment (PPE) such as protective clothing, gloves and respirator mask to avoid skin contamination and inhalation of fine powders.

- Ensure proper ventilation of the work area.

- Clean the machine from any residue powder from the previous build.

- Check that the recoater blade is not damaged to ensure smooth application.

- Load the powder by means of a hopper belonging to the feed system on the collector platform and use the calibration system to ensure that the first layer of powder is dispensed evenly and to the required thickness (*Figure 1.13*).

- Once this is done, ensure that the entire machine is sealed and start the inertisation.

- Set the machine parameters for the process.

- Start the process of building.

Figure 1.13 – Process of loading the LPBF machine.

1.5 Aluminium alloys

1.5.1 Al 2024 vs AlSi10Mg

The aluminium used on the C-27 J platform is an Al 2024 wrought alloy and it has been replaced with one in AlSi10Mg alloy LPBF manufactured; the choice of it is due to the company technical specification which refers to this material additively manufactured. In particular, the scope of this specification covers AM AlSi10Mg components produced by full melt powder bed fusion processes such as electron beam melting and laser melting. Components produced by these processes are

typically used in applications requiring mechanical properties similar to those of cast and wrought products.

In summary, in this thesis work, the material is different and the manufacturing process is different.

1.5.2   Introduction to Al alloys

The use of aluminum alloys was introduced in the early 1930s to produce structural materials for lightweight aircraft airframes. Without the use of high-strength aluminum alloys, it would not have been possible to develop aircraft components such as fuselages and wings that could fly at high speeds and altitudes. The main materials used for aircraft structural components are magnesium, titanium, steel and fiber-reinforced composites, but aluminum accounts for 60-80% of the total airframe. The amount of material varies considerably from passenger and military aircraft: as we see in *Figure 1.14* the amount of aluminum in military aircrafts is lower than in civil ones.
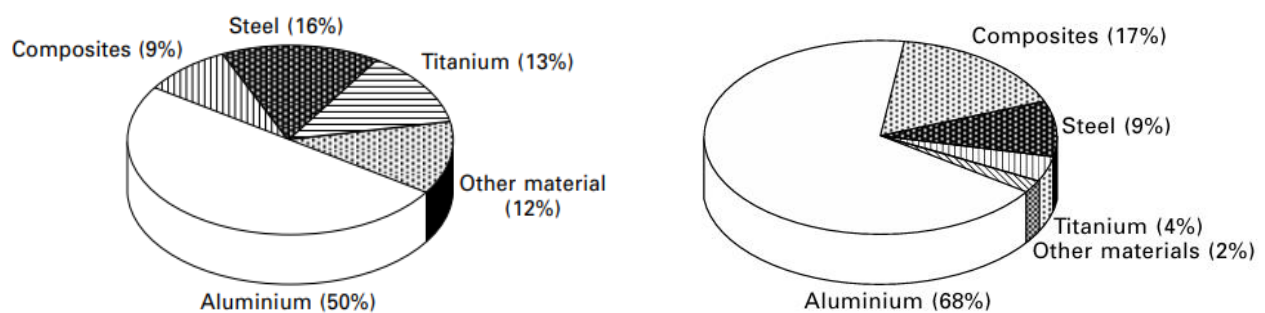
Figure 1.14 – Structural materials for Military (left) and Civil applications (right.) [12]

The main *advantages* for aluminum widespread in aerospace fields are:

- light weight (density of 2.7 g cm^{-3})
- high specific stiffness and strength
- easiness of production considering casting, forging and heat treatment
- good ductility, fracture toughness and fatigue resistance
- moderate cost

Some *disadvantages* of using aluminum must be considered:

- the drop of mechanical properties at temperature above 150°C
- risk of stress corrosion cracking (scc)
- corrosion when in contact with carbon-fibres composite

Aluminium alloys are generally divided into two macro-categories: cast alloys and wrought alloys. Cast alloys are not mechanically worked after the casting process; in fact, the mechanical properties are quite inferior to those of wrought alloys, which is why they are only used in small and non-structurally critical parts, such as in control systems.

Wrought alloys are subjected to plastic deformation to give shape and improve mechanical properties; they can be divided into non-heat treatable (non-aged hardened) alloys, which derive their strength from work hardening, solid solution strengthening and refinement of the grain size, heat treatable (aged-hardened) alloys, which strength is given mainly by precipitation hardening and secondarily from the aforementioned strengthening mechanisms.

To sum up the main possibilities to increase the strength (σ) of a given alloy is shown in the following equation:

$$\sigma = \sigma0 + \Delta\sigma wh + \Delta\sigma ss + \Delta\sigma g + \Delta\sigma ph$$

where:

$\sigma0$: intrinsic strength of materials due to crystalline lattice

$\Delta\sigma wh$: strength due to work hardening

$\Delta\sigma ss$: strength due to solution strengthening

$\Delta\sigma g$: strength due to grain size

$\Delta\sigma ph$: strength due to precipitation hardening

Non-heat treatable alloys can reach a maximum yield strength of 300 MPa, which is not sufficient for aircraft applications, whereas heat treatable alloys have yield strength in the range of 450-600 MPa, making them suitable for use in a wide range of aircraft structural components.

The majority of the aircraft aluminum components are made of wrought heat-treatable alloys. The post processing heat treatment is used to improve mechanical properties (yield and ultimate strength, fatigue resistance, fracture toughness) altering the metallurgical structure (grain size, precipitate, dislocations density), reduce residual internal stresses, dangerous for components integrity, and environmental durability (e.g. corrosion resistance).

1.5.3   Heat treatment of age-hardenable aluminum alloys

The heat treatment process that age-hardenable alloys undergo is necessary to improve their strength and achieve the mechanical properties required for aerostructures.

The most common heat treatment process consists of three operations carried out in sequence: solution annealing, quenching and artificial (or natural) ageing.

1.5.3.1 Solution annealing

During the molten metal casting process, the formation of coarse and brittle precipitates can seriously compromise the strength, fracture toughness and fatigue life of the aluminum alloy; so, it is essential that they are removed before the component is fitted to the aircraft structure.

Solution heat treatment consists of bringing the alloy to a sufficiently high temperature to dissolve the particles formed during casting, without reaching the melting point of the alloy.

It is recommended that the alloy is heated to the highest possible temperature, which varies depending on the alloy, as solubility increases with this parameter. If the temperature is not high enough, the precipitates will not dissolve completely, whereas if it is too high, local melting may occur, affecting the final properties of the component. Typical treatment temperatures for aluminum alloys are in the range of 450-600°C; this temperature is maintained for a certain period, called "soaking time", which varies from a few minutes to one day depending on the specific alloy, in order to completely dissolve the precipitates and allow a homogeneous dispersion of the element in the matrix.

1.5.3.2 Quenching

Quenching is a rapid cooling process that suppresses the reformation of coarse intermetallic precipitates. The process is carried out by immersing the hot part or spraying it with cold water. The component with a complex shape is particularly critical during this step as there is a risk of internal residual stresses being generated, leading to unwanted distortions so it is necessary to reduce the cooling rate by using hot water or other fluid such as oil or brine. Conversely, slow cooling rates can sometimes lead to precipitation which reduces the strength efficiency of the ageing step. At the end of the quenching step, the material is soft and ductile, which is why the forming processes take place immediately afterwards, before the ageing process.

Figure 1.15 shows the effect of the quenching rate on the final yield strength of the most used aerospace alloys, the 2024 Al and 7075 Al: increasing the quenching rate will result in better properties.
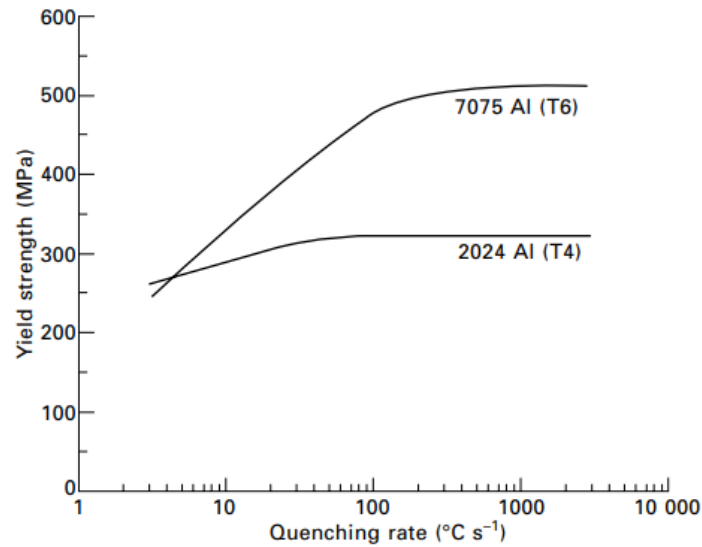
Figure 1.15 – Effect of the quenching rate on the final YS of Al 2024 and Al 7075 alloys. [12]

1.5.3.3   Ageing

The ageing process is the step which leads to the formation of precipitates that enhance the mechanical properties of the final component. Natural aging, which results can be effective even after months or years, is conducted at room temperature whereas artificial aging at elevated temperature.

Figure 1.16 shows the increase of the yield strength values for the most common aluminum alloys used in the aircraft field, the 2024 Al and the 7075 Al. It is noticeable the different effect of the aging time of one year on the two types of alloys: the 2024 Al reaches in 5 hours approximately the final value of the yield strength, whereas the 7075 Al yield strength value continues to increase throughout the entire period.
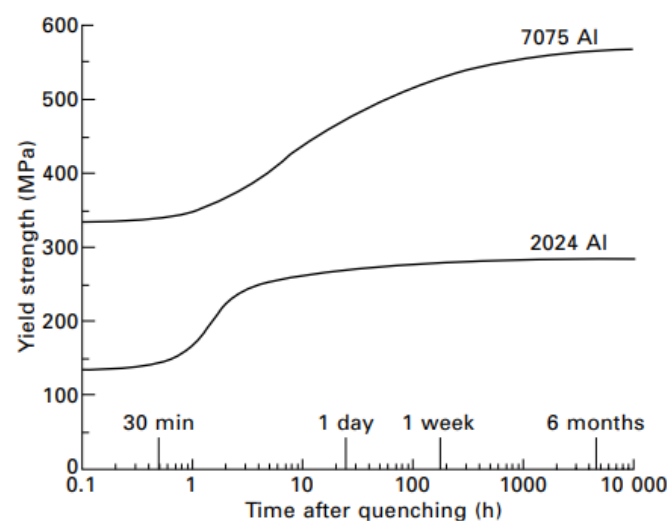
Figure 1.16 – Effect of the natural aging on the yield strength of Al 2024 and Al 7075. [12]

Natural ageing can occur at low temperature, so in some cases, such as in the application of 2024 Al rivets, it is necessary to delay the process of cooling the component at very low temperatures to maintain its softness and allow the deformation of the component into the rivet hole.

Now it has been chosen to describe artificial ageing, which is the most widely used and more controllable ageing process. It is typically carried out at 150-200 °C and lasts from a few minutes to several hours, depending on the size of the piece and the strength required. During the aging step the alloy changes its microstructure and chemical composition and consequently mechanical and corrosion properties. In particular, the steps of transformations are the followed:

- Supersaturation condition: solute exceeds the solubility value.
- Clustering: solute particles gather together and form the Guinier-Preston (GP) zones, they generate stress fields due to lattice distortion.
- Formation of coherent and incoherent precipitates: θ'' and θ' which are coherent with the matrix, θ after which is incoherent with the matrix.

After reaching the supersaturation condition, the solute atoms move to form solute-rich region called GP-zones, which composition depends on the alloy considered, the 2024 Al GP zones are, for example, rich of copper due to the high amount of this element in the alloy. At the beginning of the process, the cluster is composed of atoms arranged randomly in the lattice structure; progressively, the elements adopt a more ordered pattern that is more coherent with the matrix lattice.

The number density of GP zones is about 10^{23} - 10^{24} m^{-3}, depending on the temperature and time of aging. Their dimensions are very small, usually a few tens of atoms in length and two atomic layers thick. During ageing, the GP zones are transformed into plate- or needle-shaped precipitates with a size of about 0.1 μm; for example, in the 2024 Al alloy, the $CuAl_2$ precipitates is formed and, during the process, change their degree of coherence with the matrix. Finally, the precipitates reach the equilibrium and the mechanical properties are maximized. If the piece is kept at a high temperature for a long time, ageing phenomena occurs: the particles increase in size and the good properties previously obtained disappear (*Figure 1.17*)
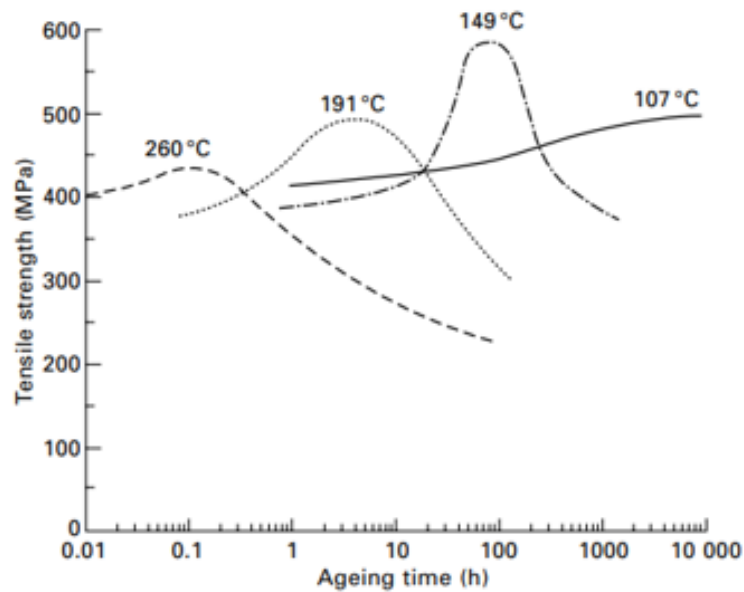
Figure 1.17 - Effect of the aging time on the tensile strength of aluminum alloy. [12]

The ageing treatment improve strength and fatigue properties but it is damaging in terms of ductility, which elongation-to failure reaches the value of 5-10% for fully-aged alloys; stress corrosion cracking (SCC) is also affected by heat treatment: the higher the hardness achieved, the lower the resistance of the alloy to SCC.

1.5.3.4   Properties of age-hardened aluminum

The improvement in strength caused by the formation of GP zones is due to the formation of an elastic stress field which distorts the alloy lattice and provides a resistance to dislocations slip. The formation of coherent particles improves the mechanical properties of the alloy because the internal strain is increased and it hinders dislocations motion.

The strength achieved during the heat treatment depends on the temperature of the process. High temperatures reduce the time to reach the maximum strength, but this is lower than the values reached by a lower temperature, but in longer time, this tendency is shown in *Figure 1.17*. It is not practical doing an ageing treatment on the alloy for many days, so it is important to choose a good compromise between strength reached and the time of heat treatment.

1.5.4   Temper designation system

Temper is an alphanumeric designation that defines how the alloy has been mechanically and/or thermally treated in order to achieve the desired metallurgical properties.

The temper designation consists of capital letters: F' for as fabricated and 'T' for age-hardened. The temper designation follows the alloy designation, and it is separated by a hyphen. For example, 2024 alloy, one of the most widely used alloys in aerospace applications, which in most cases undergoes T6 treatment to improve its mechanical properties, is defined as 2024 Al-T6. *Table 1.2* sums up the age-hardened heat treatments applied on aluminum alloys.

Table 1.2 - Age-hardened heat treatments on aluminum alloys [12]

Age-hardened
T1 – cooled from fabrication temperature and naturally aged
T2 – cooled from fabrication temperature, cold-worked and naturally aged
T3 – solution treated, cold-worked and naturally aged
T4 – solution treated and naturally aged
T5 – cooled from fabrication temperature and artificially aged
T6 – solution-treated and artificially aged
T7 – solution-treated and stabilised by over-ageing
T8 – solution-treated, cold-worked and artificially aged
T9 – solution-treated, artificially aged and cold-worked
T10 – cooled from fabrication temperature, cold-worked and artificially aged

1.5.5   Aluminum alloys designation system

The International Alloy Designation System (IADS) uses a classification to categorize the more than 500 aluminum alloys that exist in the academic and industrial scenario, according to their technological production process and chemical composition. In particular, as wrought aluminum alloys are the most widely used in the aerospace industry, only their classification is considered in this thesis.

Each alloy is defined by a four-digit number: XXXX. The first one indicates the alloy series, for example, 1XXX belongs to the 1000 series, 2XXX to 2000 series and so on and so forth. The second digit indicates the number of modifications the alloy is subjected to; for example, 5353 has been modified three times but the composition is similar to 5053 Al alloy. The last 2 digits have no meaning except the 1000 alloy series; for example, the 1145 alloy means that Al must be 99.45% pure.

The wrought aluminum alloys classification is shown on the *Table 1.3*.

Table 1.3 - Wrought aluminum alloy series. [13]

Aluminum Alloy Series, Alloying Elements, and Category		
SERIES NUMBER	ALLOYING ELEMENT	ALLOY CATEGORY
1XXX	Aluminum	Commercially Pure
2XXX	Copper	Heat-Treatable
3XXX	Manganese	Non Heat-Treatable
4XXX	Silicon	Non Heat-Treatable
5XXX	Magnesium	Non Heat-Treatable
6XXX	Magnesium & Silicon	Heat-Treatable
7XXX	Zinc	Heat-Treatable

1.5.6   Non-heat treatable aluminium alloys

The use of non-heat treatabel wrought alloys is limited because structural components require high performance in terms of strength, fatigue resistance and ductility which this type of alloy cannot provide. The 1000, 3000, 5000 and most of the 4000 alloys cannot be age-hardened by heat treatment. The improvement in strength due to the solution strengthening mechanism is not very effective due to the inability of aluminium to dissolve large amounts of alloying elements at room temperature, either in substitutional or interstitial sites, this is shown in *Figure 1.18*.
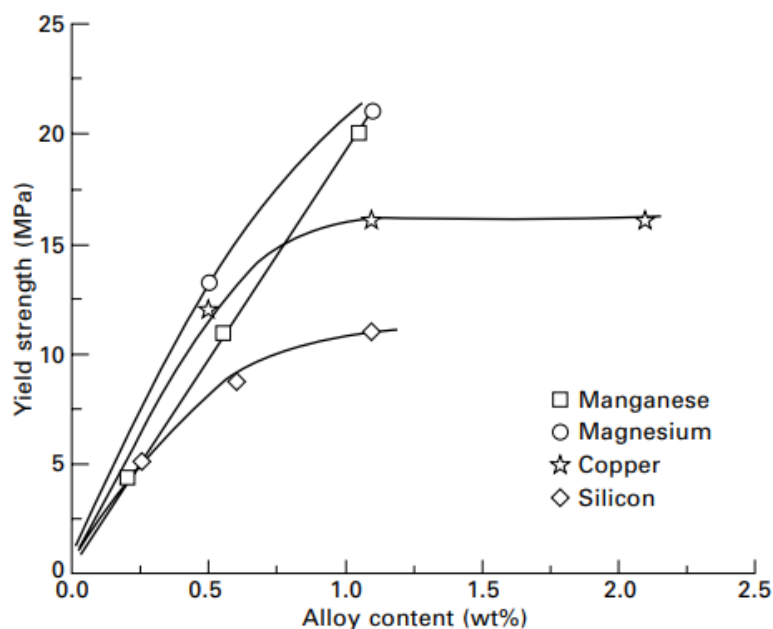
Figure 1.18 – Effects of different alloying elements on solid solution strengthening of aluminum. [12]

The strengthening mechanisms of strain hardening and grain size control are more effective for non-heat treatable alloys. *Figure 1.19* shows the improvement of yield strength and ultimate tensile strength as a function of the percentage of cold working (strain hardening).
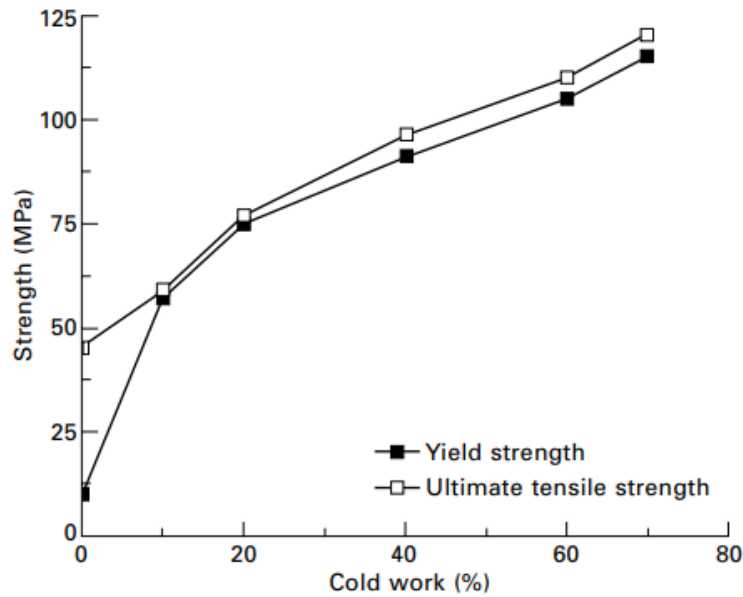
*Figure 1.19 - Influence of cold working percentage on the strength improvement
of pure aluminum. [12]*

A brief description of non-age hardenable aluminum alloys is given below.

1.5.6.1   1000 series

The highest purity (Al > 99%) form of aluminium alloy belongs to this category. These alloys are characterised by low strength (most of them do not exceed 40 MPa yield strength), low fatigue resistance and high ductility, making them unsuitable for structural use in aircraft. They can be used for non-structural parts where low weight is required. In general, they can be exploited where corrosion resistance is important, as in chemical plants, or where good thermal and electrical conductivity is required, as in heat exchangers.

1.5.6.2   3000 series

The main alloying element is manganese (Mn), which does not precipitate during heat treatment. The yield strength does not exceed 200 MPa, which is why they are rarely used in aircraft applications, but are particularly suitable for automotive components (e.g. radiators and interior panels).

1.5.6.3   4000 series (Al-Si)

This type of alloy is characterized by a high amount of Si which limits its application in aerospace field due to the formation of a particular silicon dendritic structure which is brittle and reduces the ductility and the toughness of the alloy.

1.5.6.4   5000 series (Al-Mg)

The alloy is characterized by the formation of a specific precipitate (Mg_2Al_3) which increases the strength of the alloy, but its structure cannot be controlled by heat treatment, which is why it is classified as a non-aged hardenable alloy. The 5052 Al alloy, which contains 2.5% Mg and 0.25% Cr, is one of the highest strength non-tempered alloys used in aerospace applications, in fact it is often used in aircraft frameworks as wing ribs or stiffeners.

1.5.7   Heat treatable aluminum alloys

The use of aluminum alloys in aerospace application is largely limited to heat treatable Al alloy, in fact the 2000, 6000, 7000, and 8000 are strengthened with a specific heat treatment make the components able to resist to the high loads typically present on aircraft parts. A description of heat treatable aluminum alloys is given in the following rows.

1.5.7.1   2000 series (Al-Cu)

This class of Al alloys is the most widely used for structural components in aircraft applications. The main alloying element is copper, which forms Al_2Cu precipitates during age-hardened heat treatment, significantly increasing the strength of the alloy. In addition to high strength, 2000 alloys are characterized by good fatigue resistance and toughness. Moreover, this class of Al alloys are particularly suitable for damage-tolerant applications, i.e. the ability to sustain defects in a safety manner until repair can be carried out, e.g. in components which are particularly subjected to high fatigue loads.

In particular, the 2024 Al alloy (Al-4.4Cu-1.5Mg) has been used for aircraft for many years due to high tensile strength, making it ideal for structural applications; newer alloys are now being introduced, such as 2054, which has better fatigue and fracture toughness properties, but 2024 is still one of the most widely used.

In *Table 1.4* and *Table 1.5* chemical compositions and mechanical properties of the main 2000 alloys used in aircrafts, are reported.

Table 1.4 – Chemical composition of the main 2000 aircraft alloys. [12]

Alloy	Cu	Mg	Zn	Mn	Cr (max)	Si (max)	Fe (max)
2017	3.5–4.5	0.4–0.8	0.25	0.4–1.0	0.1	0.8	0.7
2018	3.5–4.5	0.45–0.9	0.25	0.2	0.1	0.9	1.0
2024	3.8–4.9	1.2–1.8	0.3	0.3–0.9	0.1	0.5	0.5
2025	3.9–5.0	0.05	0.3	0.4–1.2	0.1	1.0	1.0
2048	2.8–3.8	1.2–1.8	0.25	0.2–0.6		0.15	0.2
2117	2.2–3.0	0.2–0.5	0.25	0.2	0.1	0.8	0.7
2124	3.8–4.0	1.2–1.8	0.3	0.3–0.9	0.1	0.2	0.3

Table 1.5 – Mechanical properties of the main 2000 aircrafts alloys. [12]

Alloy	Temper	Yield strength (MPa)	Tensile strength (MPa)	Elongation (%)
2017	T4	275	425	22
2018	T61	320	420	12
2024	T4	325	470	20
2024	T6	385	475	10
2024	T8	450	480	6
2025	T6	255	400	19
2048	T85	440	480	10
2117	T4	165	300	27
2124	T8	440	480	6

1.5.7.2   6000 luminium alloys (Al-Mg-Si)

The main alloying elements of 6000 series are magnesium and silicon which form Mg_2Al_3 and Mg_2Si precipitates during age-hardened heat treatment. These alloys are rarely used in aircraft applications due to their low fracture toughness.

1.5.7.3   7000 aluminum alloys (Al-Cu-Zn)

The 7000 series alloys, together with the 2000 series aluminum alloys, are the most widely used in the aircraft industry. The main alloying elements are copper, zinc and magnesium, forming $CuAl_2$, Mg_2Al_3 and $Al_{32}(Mg,Zn)_{49}$, which give the 7000 alloys a higher yield strength (470 - 600 MPa) than the 2000 alloys (300 - 450 MPa).

1.5.7.4   8000 aluminum alloys

Many 8000 alloys contain lithium, which has a very special property: it reduces density while increasing the elastic modulus and tensile strength. *Figure 1.20* shows the effect on Young's modulus

and density with the percentage of lithium content; the modulus increases by 5% whereas the density decreases by 3% for every 1% of lithium added. Although the promises were others, there was not a widespread use of 8000 alloys, due to the high cost of lithium, which is a strategic element for other technologies, e.g. battery industry, and high processing costs, they are considered only a niece.
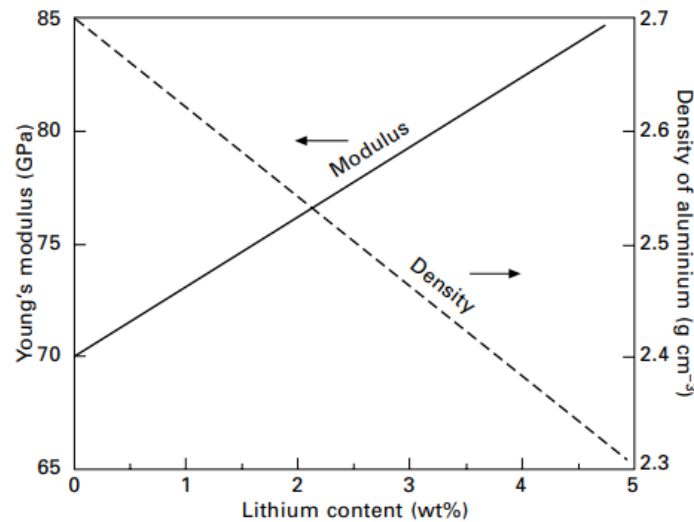
Figure 1.20 - Effect of lithium content on the Young's modulus and density of aluminum. [12]

1.5.8   AlSi10Mg via AM

AlSi10Mg components have a very high strength to weight ratio, so this alloy is widely used in the aerospace industry. Physical properties such as density and consequently mechanical properties depend on the VED, as said in *section 1.4.1*, so optimizing the process parameters is fundamental to obtain a component with the highest properties.

The level of porosity strongly depends on the VED applied during the process. In the following rows are reported the results obtained by [14]. *Figure 1.21* shows at OM micrographs along the Building Direction (BD) of samples produced with different VED: 43 (a), 56 (b), 66 (c) J/mm^3.
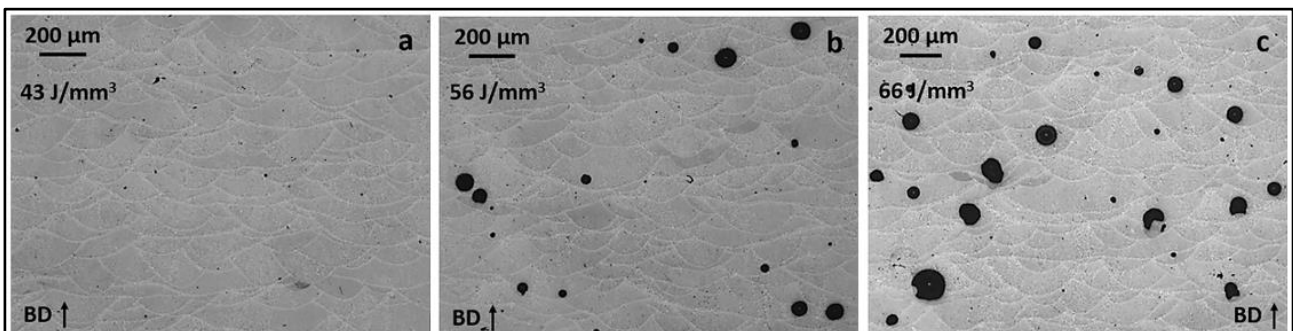
Figure 1.21 – OM micrographs of samples produced at different VED:

(a) 43 J/mm^3 , (b) 56 J/mm^3 , (c) 66 J/mm^3.

The AlSi10Mg shows a hierarchical microstructure with the presence of melt pools along the layers (*Figure 1.22a*) and large columnar grains elongated towards the BD (*Figure 1.22b*). Each grain is made up of a continuous network of fibrous eutectic Si that surrounds α-Al matrix (*Figure 1.22c*). Nano-sized Si-particles that exhibit both globular and acicular morphology are also present (*Figure 1.22d*). These particles are due to the reduced solubility of Si inside the α-Al matrix.
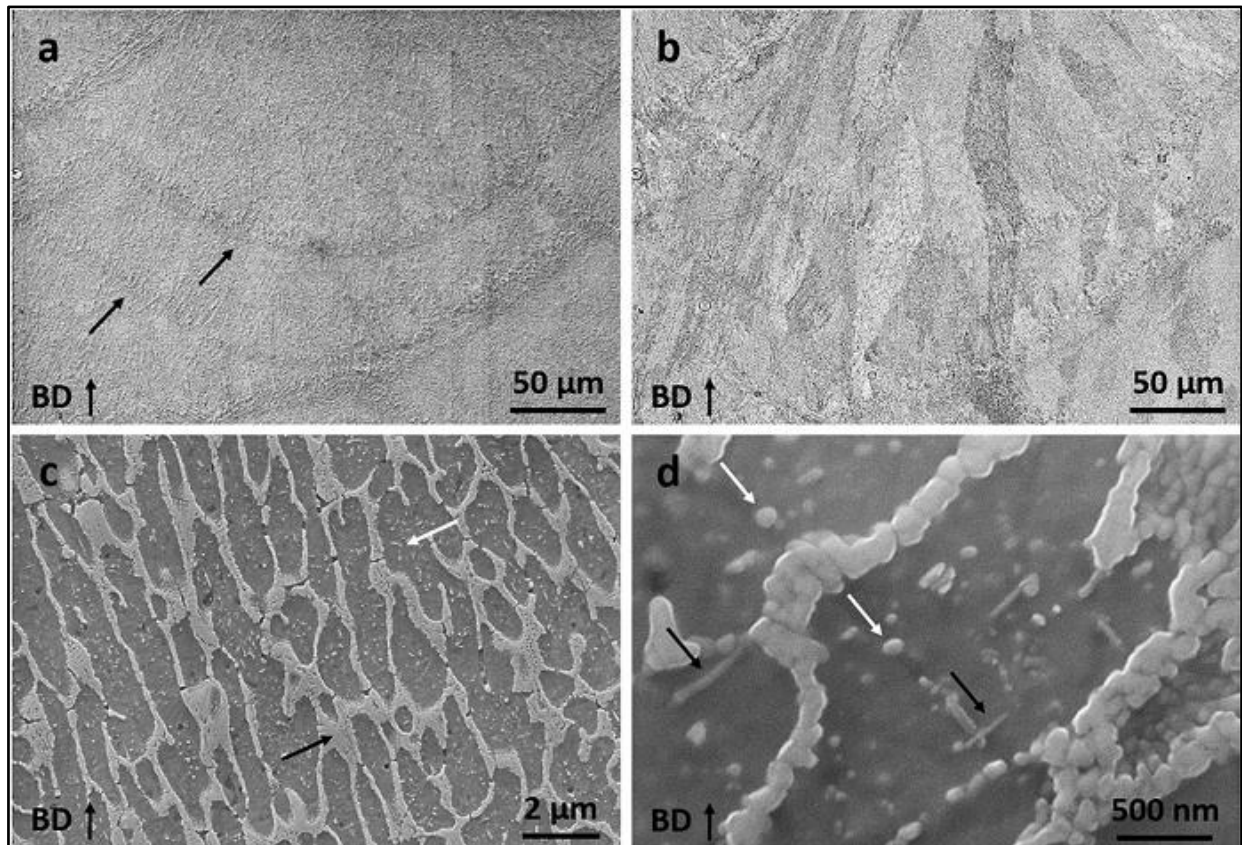
Figure 1.22 – (a) Melt pools highlighted by the black arrows. (b) Columnar grains.
(c) Fibrous eutectic Si (black arrow) surrounds by α-Al matrix (white arrow).
(d) Globular (white arrow) and acicular (black arrow) nano-sized Si precipitates.

As reported by [15], the T6 heat treatment modifies the properties of the material to provide an attractive compromise between material strength and ductility. In particular, after T6, the microstructure is no longer characterized by fibrous eutectic Si, but there is the formation of Si spheroids which strengthen the material by Orowan strengthening (*Figure 1.23*).
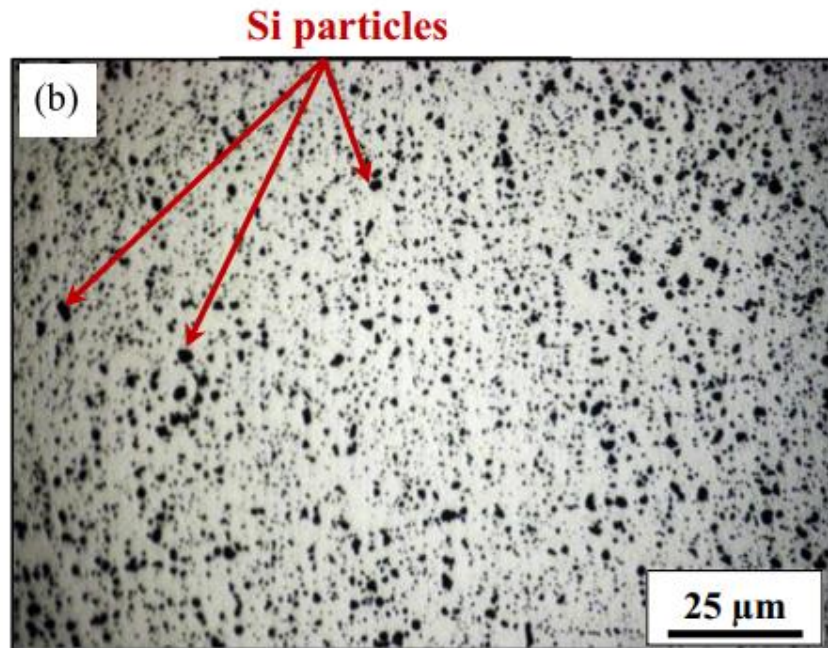
Figure 1.23 – T6 heat-treated AlSi10Mg microstructure at optical microscope.

1.5.9   Al 2024 vs AlSi10Mg properties comparison

Considering that for the C-27J Bracket there is the intention to further change the technology of production and also the material, it is useful to show a primary comparison between these materials' main properties:

- YS_xy: Yield Strength along xy-plane
- YS_z: yield Strength along xz-plane
- UTS_xy: Ultimate Tensile Strength along xy-plane
- UTS_z: ultimate tensile strength along xz-plane
- A %: percentage elongation at break along xy and xz planes.

All these properties have been taken from 3 different sources:

- PN: Al 2024 sheet and plate properties from Al2024-T3 for AMS-QQ-A-250/5 [16].
- EOS: AlSi10Mg LPBF and heat treated manufactured properties from EOS Aluminum AlSi10Mg material datasheet [17].
- PoliTO: AlSi10Mg LPBF manufactured properties from Politecnico literature [15].

The properties are shown in *Figure 1.24*.
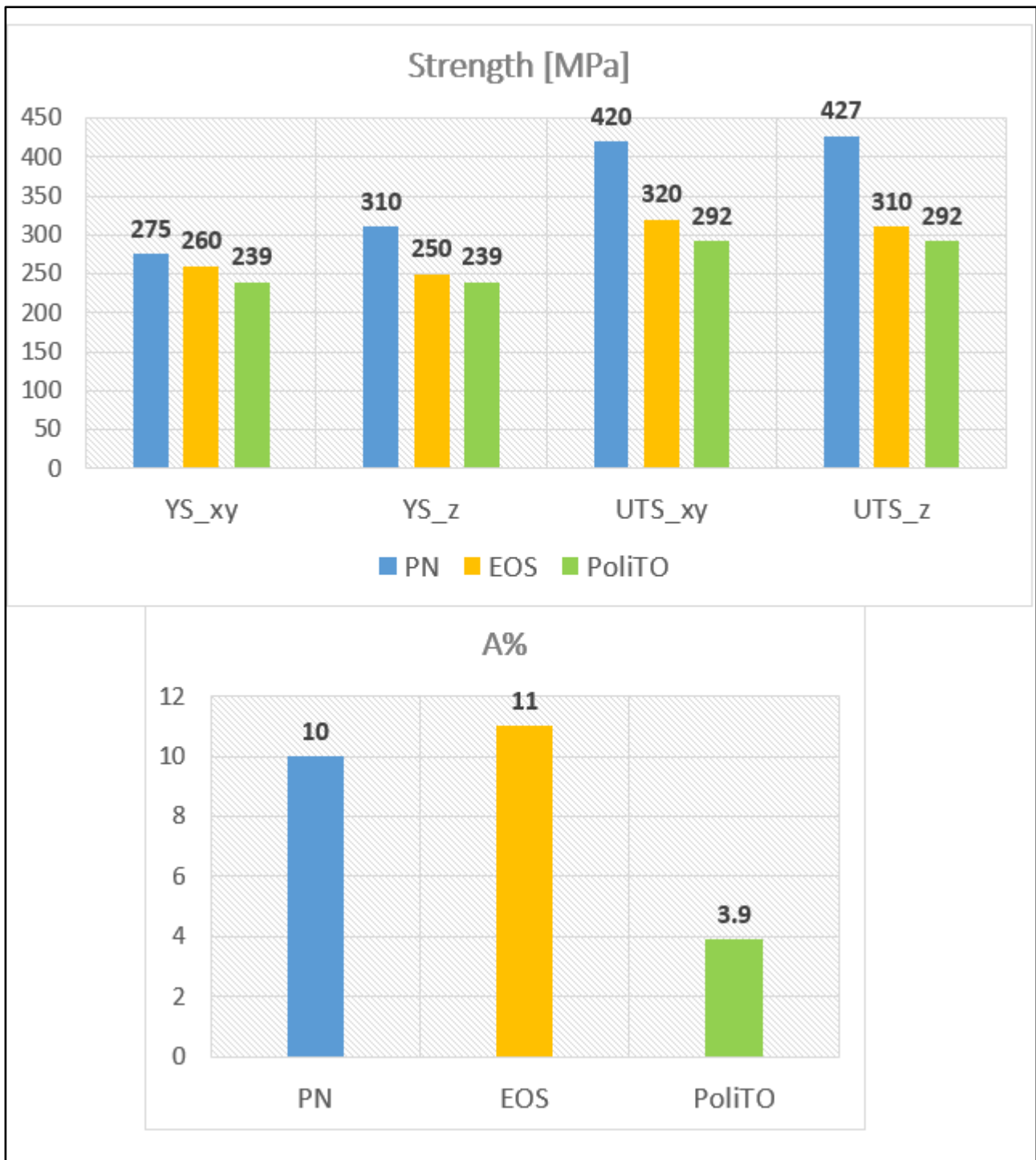
Figure 1.24 – Histograms of the main Aluminum properties.

As can be seen from the histograms, Al 2024 sheet and plate has better properties than AlSi10Mg LPBF manufactured. The EOS datasheet gives values that are in line with those of the PoliTO paper. A company technical specification, which is not quoted for reasons of intellectual property of Leonardo S.p.A., defines the minimum requirements for AlSi10Mg obtained by the LPBF process.

The requirements for YS are lower than those guaranteed by EOS and found by PoliTO, whereas those for UTS are higher than both. However, the value of YS should be given more importance.

To sum up as a first analysis, changing the technology, from sheet and plate to LPBF, and the material, from Al 2024 to AlSi10Mg, allows to obtain lower properties. A more in-depth analysis could be necessary if the required properties of the use case have a tolerance and AlSi10Mg can effectively replace the Al 2024 or in case the design of the component must be modified.

Compare these values with those obtained in *section 3.1.2* following the tensile tests.

1.6 Titanium alloys

1.6.1 Ti6Al4V

The titanium used in the M-346 and M-345 platforms is the Ti6Al4V alloy, which complies with the Aerospace Materials Specifications (AMS), in particular the 6931 specification for wrought products. The choice of this material is based on the company's technical specification which refers to this additive manufactured material. In particular, the scope of this specification covers AM Ti6Al4V components produced by full melt powder bed fusion processes. Components produced by these processes are typically used in applications requiring mechanical properties similar to those of cast and wrought products.

1.6.2 Introduction to Ti alloys

Titanium is a widely used alloy in the aerospace industry. This is mainly due to the fact that it retains its mechanical properties at high temperatures up to 500-600 °C, which is why it is used in engine components such as compressor blades, shafts and ducts, which are particularly exposed to these temperatures. Titanium alloys are also used in highly stressed airframe structures such as transmissions, wing sections and landing gear. The high specific strength allows smaller structural components to be used to carry the same load.

To sum up, titanium alloys are used in the aircraft structure for their unique combination of properties:

- high strength
- moderate density
- good creep strength
- elevated fracture toughness
- long fatigue life
- excellent resistance to oxidation and corrosion.

However, there are some disadvantages to using titanium:

- cost

- processability

- limited joining applications.

1.6.3   Phases of titanium

The titanium is characterized by the property of allotropy (*Figure 1.25*), therefore it exists in two different crystalline structures. In particular, titanium alloys can assume a Hexagonal-Close-packed (HCP) Structure, the α-Ti phase, and a Body Centered-Cubic (BCC), β-Ti phase, or the simultaneous presence of both, α+β-Ti phase. The α-stabilizing elements can be both substitutional (e.g. Al) or interstitial (e.g. C, N, O); the β-stabilizing are all the others, the most common are V, Mo. For pure titanium, the phase change happens at 882°C (1620°F) and the melting point is at 1670°C. The addition of alloying elements changes the phase transformation temperature and the melting temperature of the alloy. *Figure 1.26* shows how the β-transus temperature can change in function of the amount of α- or β- stabilizers. α-Ti alloys are particular idoneous for applications at high temperatures, such as aircraft engines, when the creep resistance is required whereas the β-Ti alloys have higher tensile strength and fatigue resistance and are therefore mainly used for airframe structures. The α+β-Ti alloys have generally properties between α-Ti and β-Ti alloys, so they can be used for both applications.
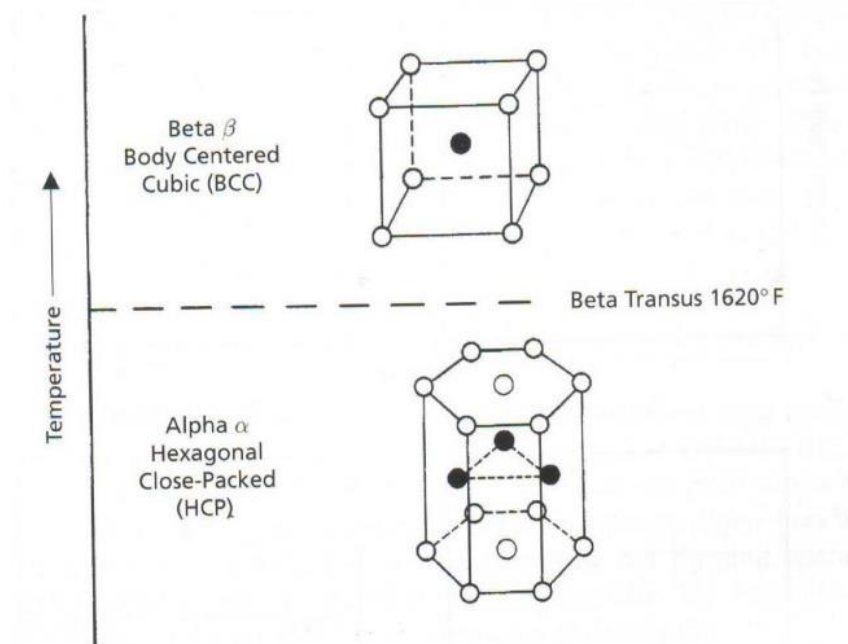
Figure 1.25 – Crystal structure allotropy of pure titanium. [12]
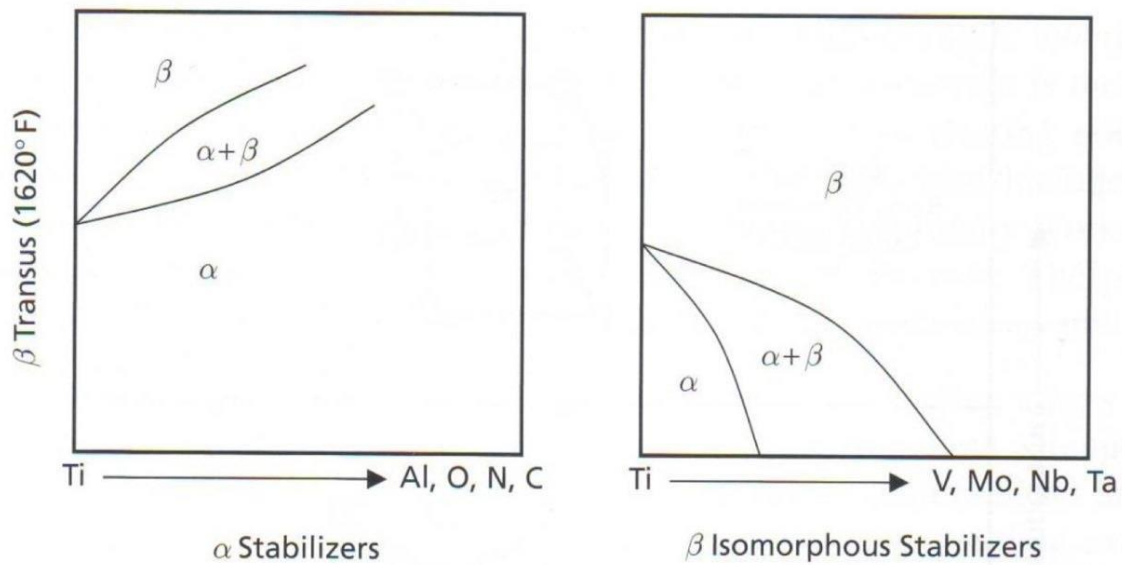
Figure 1.26 – The effect of α- & β-stabilizer elements on the β-transus temperature. [12]

1.6.3.1   Commercially pure Ti

Commercially pure titanium (>99% Ti) has low mechanical properties, the tensile strength is 450 MPa about so is not used in highly stressed aircraft structures but, because of its ability to form a passivating oxide layer, it is used only in non-structural elements where good corrosion resistance is required, such as storage tanks.

1.6.3.2   α-Ti alloys

There are 2 categories of alpha titanium alloys known as near-α and super-α.
Near-α Ti-alloys contain a greater proportion of α-stabilizer elements and a lesser proportion of β-stabilizers (<2% wt), which means that the microstructure is characterized by β-Ti grains dispersed in a higher proportion of α-Ti grains which act as a matrix. Super-α Ti-alloys contain a large amount of α-stabilizer elements (>5% wt) which means that the alloy is fully composed by α-Ti grains. The near-α-Ti alloys have higher mechanical properties (750-1000 MPa) due to the presence of the hard β-Ti phase, and they have good creep resistance properties, making them the better choice for gas turbine blades that reach 500-600°C for long periods of time.
Table 1.6 shows a mechanical properties comparison between typical near-α and super-α alloys.

Table 1.6 - Composition and mechanical properties of α-Ti alloys used in gas turbine engines. [12]

Alloy type	Composition	Young's modulus (GPa)	0.2% Yield strength (MPa)	Tensile strength (MPa)
Super-α	Ti–5Al–2.5Sn (IMI317)	103	760	790
Near-α	Ti–6Al–2Sn–4Zr–6Mo	114	862	930
	Ti–5.5Al–3.5Sn–3Zr–1Nb (IMI829)	120	860	960
	Ti–5.8Al–4Sn–3.5Zr–0.7Nb (IMI834)	120	910	1030
	Ti–2.25Al–11Sn–5Zr–1Mo (IMI679)	115	900	1000
	Ti–6Al–4Zr–2Mo (IMI685)	115	960	1030

Three possible methods that allow to strength the α-Ti alloys:

- work hardening / plastic deformation
- solid solution hardening
- grain size refinement

Plastic deformation, such as extrusion or rolling, allows them to double the tensile strength and reach a value of 800 MPa about. Solid solution hardening increases the tensile strength of about 35-70 MPa every 1% of alloying element; *Figure 1.27* shows the effect of aluminum, which is the main α-stabilizer element, on strength and ductility.
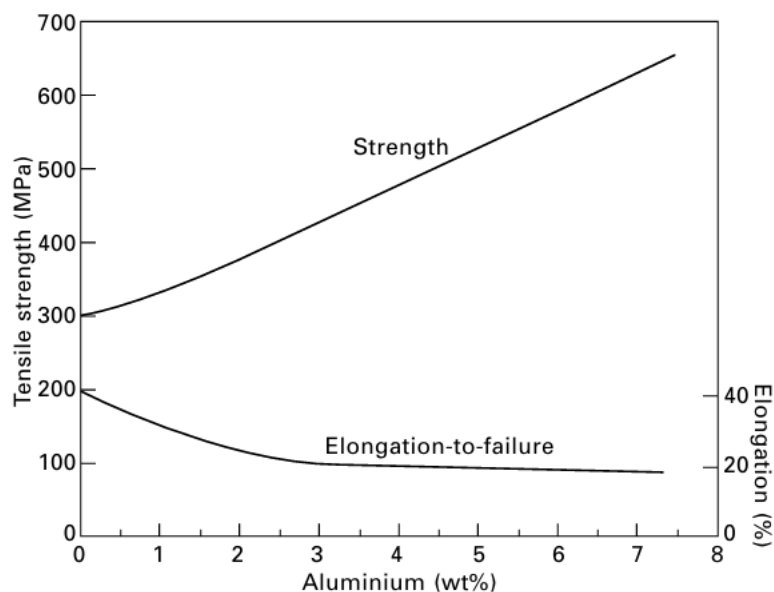
Figure 1.27 – Effect of Al content on tensile properties. [12]

1.6.3.3   β-Ti alloys

Beta-titanium alloys are produced by adding a large amount (10-20 wt%) of β-stabilizers elements, such as V, Mo, Fe, Cr. The strength of β-Ti alloys is higher than the α-Ti alloys, in fact the yield strength is between 1150 and 1300 MPa compared with the lower values of α-Ti alloys; fatigue resistance is better too but they are much less used because of their lower creep resistance which is the most important property required in the aerospace field.

These alloys can be strengthened by heat treatment thanks to the precipitation hardening. A typical heat treatment of β-Ti alloys is solutioning at 750°C, rapid cooling to room temperature and ageing at 450-600°C. The strength of the alloy can be increased by 30-50% with respect to the original value.

1.6.3.4   α+β-Ti alloys

The α+β alloys have intermediate properties between the previous two: the good mechanical properties at room temperature of β-Ti alloys and the modern high creep resistance at high temperatures of α-Ti alloys. Typical yield strength values are 900-1000 MPa, which is higher than near α-Ti alloys and lower than many β-Ti alloys. The strength of α+β-Ti alloys is due to several hardening processes such as work hardening, solution hardening and grain boundary strengthening.

The following chapters discuss Ti6Al4V, the workhorse alloy for aircraft applications and the subject of this thesis. A detailed comparison will be made between Ti6Al4V by traditional methods and AM properties.

1.6.4   Ti6Al4V via AM

Ti6Al4V is an α+β titanium alloy with an HCP α-phase stable at low temperatures and a BCC β-phase stable at high temperatures. The LPBF process in the Ti6Al4V manufacturing process involves:

1. Powder melting and extremely fast directional solidification with the formation of HCP martensite α' at the Martensite Start temperature (MS) in a wide temperature rate from 575°C to 800°C, depending on the cooling rate. It is the effect of strengthening the alloy.
2. Re-melting and re-solidification during the subsequent scan tracks and layers.

As reported by [18] the process can lead to different types of defects. The main is the porosity, strongly depending on the scan speed. *Figure 1.28* shows the influence of the scan speed, from higher to lower respectively, on porosity types with a fixed laser power of 175 W and a hatching distance of 100 μm.
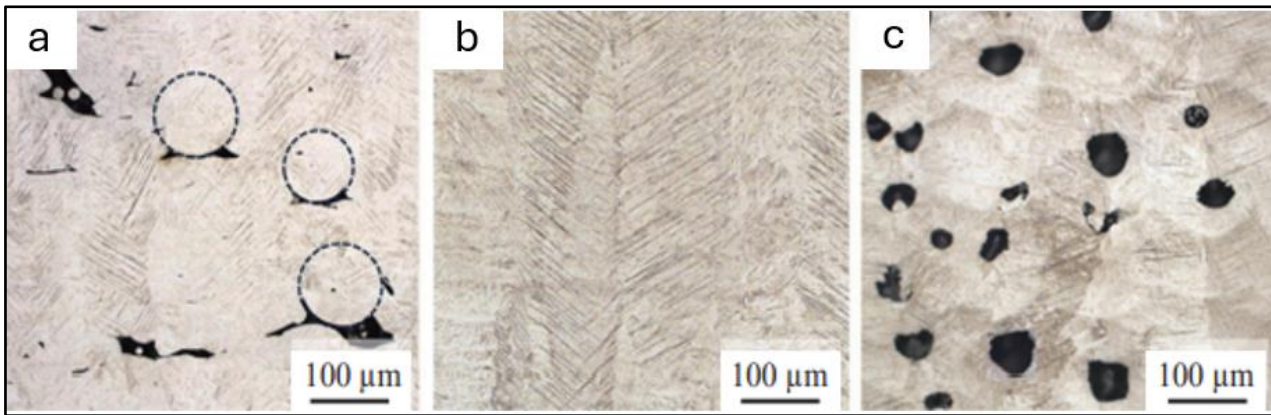
Figure 1.28 – Optical micrographs of Ti6Al4V samples-built a) at high scan speed b) at intermediate scan speed c) low scan speed.

It is possible to see the lack-of-fusion due to insufficient power penetration at high scan speed (a) a nearly fully dense microstructure at an intermediate scan speed (b) and keyhole type defects due to the overheating at low scan speed (c). In the fully dense microstructure, it can be seen that the typical elongated martensite α' microstructure grows along columnar grains.

During the process, the high cooling rate and large thermal gradients result in high residual stresses. In particular, there will be tensile residual stresses at the top and bottom of the component and compressive residual stresses in the intermediate region. These stresses are detrimental to fatigue properties because they can cause fatigue crack propagation. In addition, the process is the cause of high surface roughness, which is a typical defect of the Ti 64 LPBF produced. To reduce these residual stresses, the LPBF parts are subjected to a stress-relieving (SR) heat treatment, see *section 2.2.3*. After the SR there is a change of microstructure: from fully α' martensitic microstructure to α+β alternating lamellae.

1.6.5 Ti6Al4V traditional and AM properties comparison

For titanium use cases there is the intention to change the technology of production and, as in aluminum use case, a primary comparison of main mechanical properties is done.

All the properties have been taken from 3 different sources:

- PN: Ti6Al4V properties for AMS 6931 obtained with traditional methods [19].
- EOS: Ti6Al4V LPBF manufactured properties from EOS Aluminum Ti6Al4V material datasheet [20].
- PoliTO: Ti6Al4V LPBF manufactured properties from Politecnico literature [21].

The properties are shown in *Figure 1.29*.
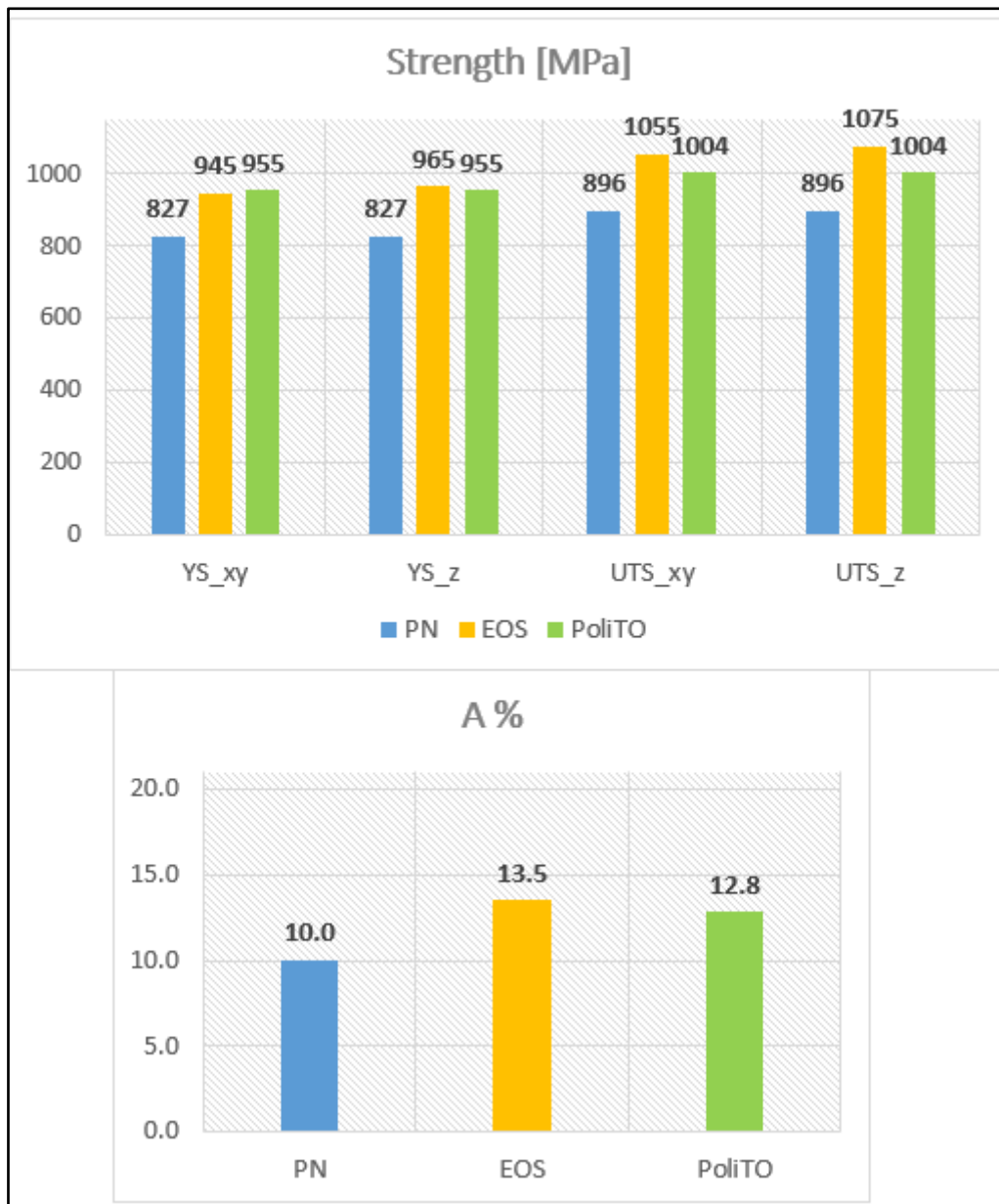
Figure 1.29 – Histograms of the main Titanium properties.

As can be seen from the histogram, Ti6Al4V for AMS 6931 has lower mechanical properties than Ti6Al4V LPBF manufactured. This provides an incentive to use LPBF technology to manufacture PN instead of traditional methods.

As for the aluminum case, a company technical specification, which is not quoted for reasons of intellectual property of Leonardo S.p.A., defines the minimum requirements for Ti6Al4V obtained by the LPBF process. The requirements of YS, UTS, A% of the specifications perfectly match those guaranteed by EOS and found by PoliTO.

Compare these values with those obtained in *section 3.2.2* following the tensile tests.

Chapter 2
MATERIALS AND METHODS
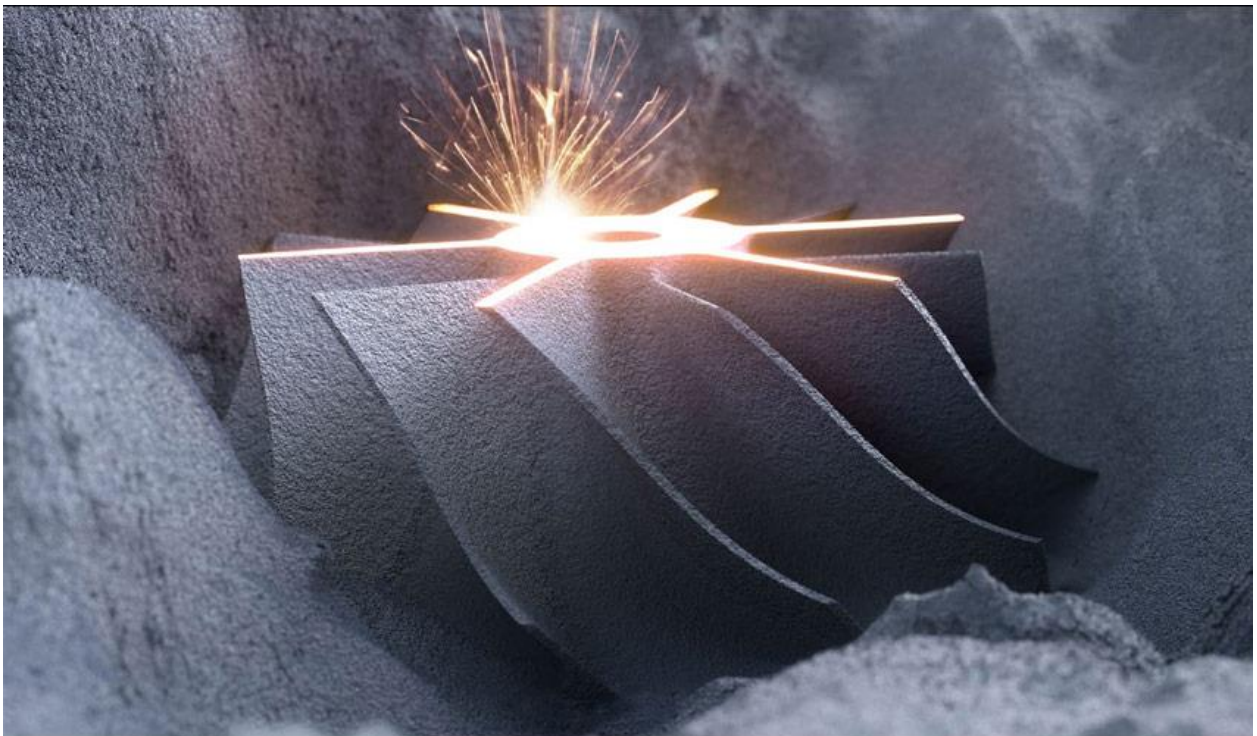
2. MATERIALS AND METHODS

The activity is divided into four WP, which describe the different steps that have been followed during this thesis work. Each is described in detail.

2.1 WP1: Job design and optimization for production via AM

This thesis work starts with the planification of the building platform of the job manufactured via LPBF. Two materials are considered, AlSi10Mg and Ti6Al4V, so two jobs have to be produced, one for each material.

Taking into account Leonardo's internal quality procedures, the use case considered must be replicated twice for each order: one component, which is considered as the model to be integrated, useful to demonstrate and then to be mounted on the vehicle, and the second, called the first article, which is potentially submitted both for dimensional and chemical-physical control, testing of mechanical properties and other tests necessary for approval and qualification.

The bracket, which belongs to C-27J platform, was previously realized using SolidWorks CAD software with reference to the dimensions and shapes of the component's drawing. *Figure 2.1* shows technical drawing and CAD drawing respectively.
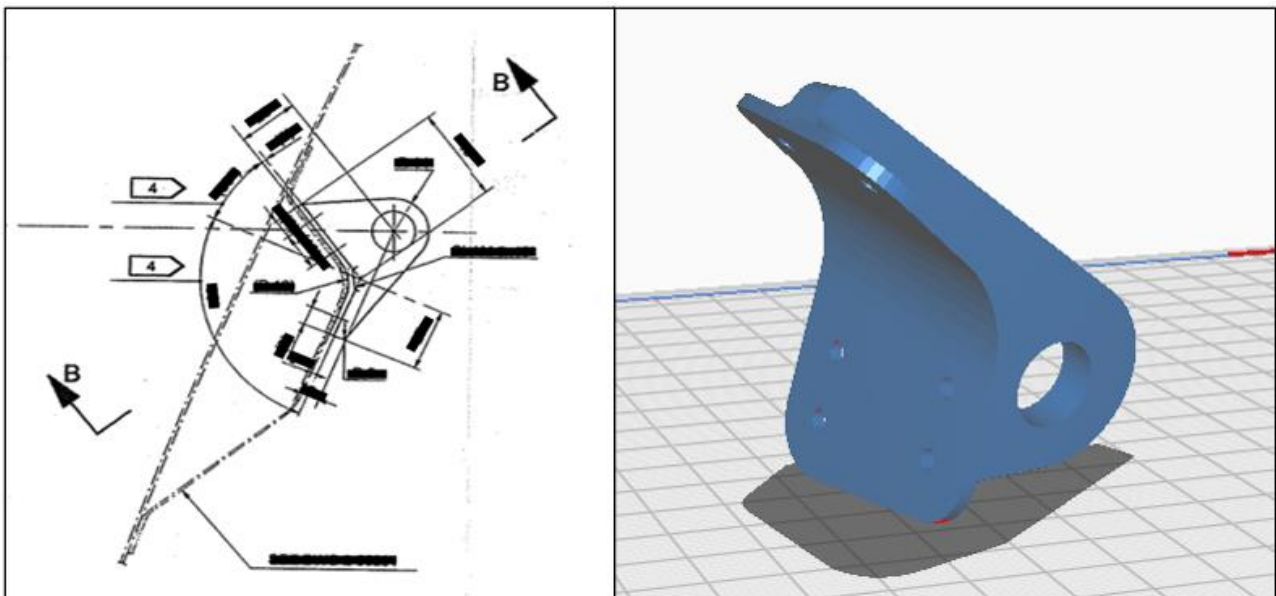
Figure 2.1 – Technical drawing (left) and CAD drawing (right) of C-27J Bracket. (© Leonardo S.p.A.)

For titanium, two use cases were selected, each belonging to two different systems of two different programs, the M-346 & M-345. For the M-346 Clevis both technical drawing and CAD drawing were present on the ERP of Leonardo Aircraft Division (*Figure 2.2*). Considering the M-345 Connector, only the CAD drawing was available on the portal, so this is the only one to rely on for shapes and dimensional tolerances (*Figure 2.3*).
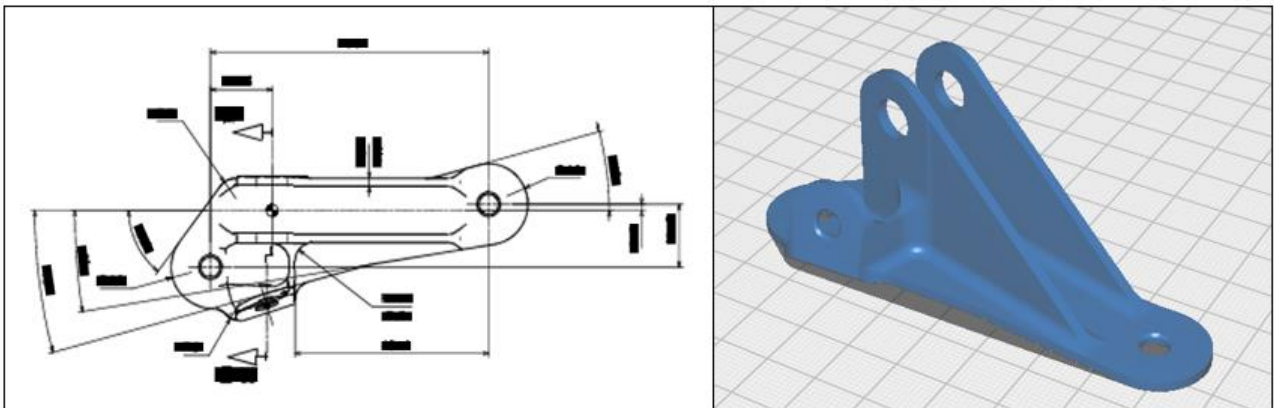
Figure 2.2 – Technical drawing (left) and CAD drawing (right) of M-346 Clevis. (© Leonardo S.p.A.)
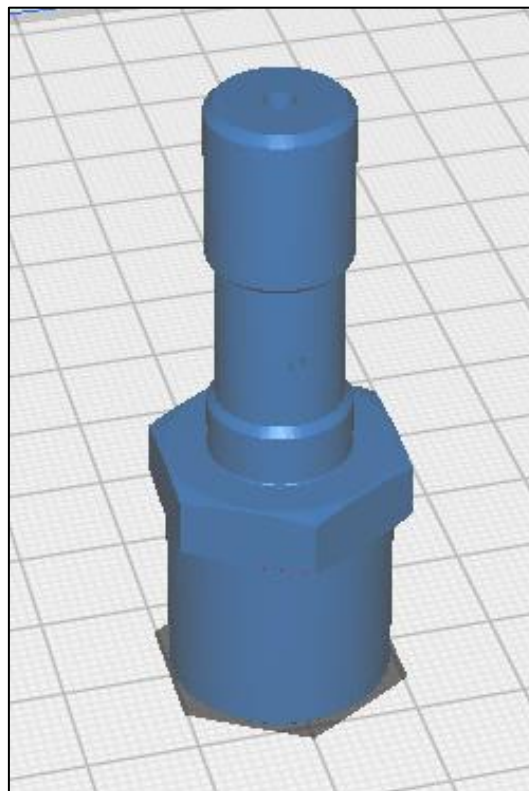
Figure 2.3 – CAD drawing of the M-345 Connector. (© Leonardo S.p.A.)

Considering research agreement, in addition to the use case, on the same job the following samples must be produced:

- tensile specimens (10 samples) manufactured as per standard ASTM E8/E8M (1.sdt) for AlSi10Mg:
  - 2 Horizontal tensile samples & Stress Relieved (Al_H_SR)
  - 2 Horizontal tensile samples & Stress Relieved & Heat Treated (Al_H_SR_HT)
  - 2 Vertical tensile samples as built & Stress Relieved (Al_V_SR)
  - 2 Vertical tensile samples as built & Stress Relieved & Heat Treated (Al_V_SR_HT)
  - 2 Vertical tensile samples machined & Stress Relieved & Heat Treated (Al_V_machined_SR_HT)
- tensile specimens (6 samples) manufactured with the same standard for Ti6Al4V:
  - 2 horizontal tensile samples & Stress Relieved (Ti_H_SR)
  - 2 vertical tensile samples as built & Stress Relieved (Ti_V_SR)
  - 2 vertical tensile samples machined & Stress Relieved (Ti_V_machined_SR)
- Cylindrical and cubic controlled samples for measuring density, roughness, porosity percentage and pore aspect ratio, hardness and chemical composition.

All the objects were converted to stereolithography standard (*.stl*), a file format commonly used in 3D printing technology. This was used because it is the standard used by Magics [22] the *.stl* editor software used to organize the printing platform prior to the LPBF process. The main functions of Magics are to repair files that have common problems such as holes, edges and angles, and to create the best support structures to hold the part and reduce the amount of material. Thanks to the software, it was also possible to create a base under each use cases to compensate for the loss of material during the Electrical Discharge Machining (EDM) cutting operation.
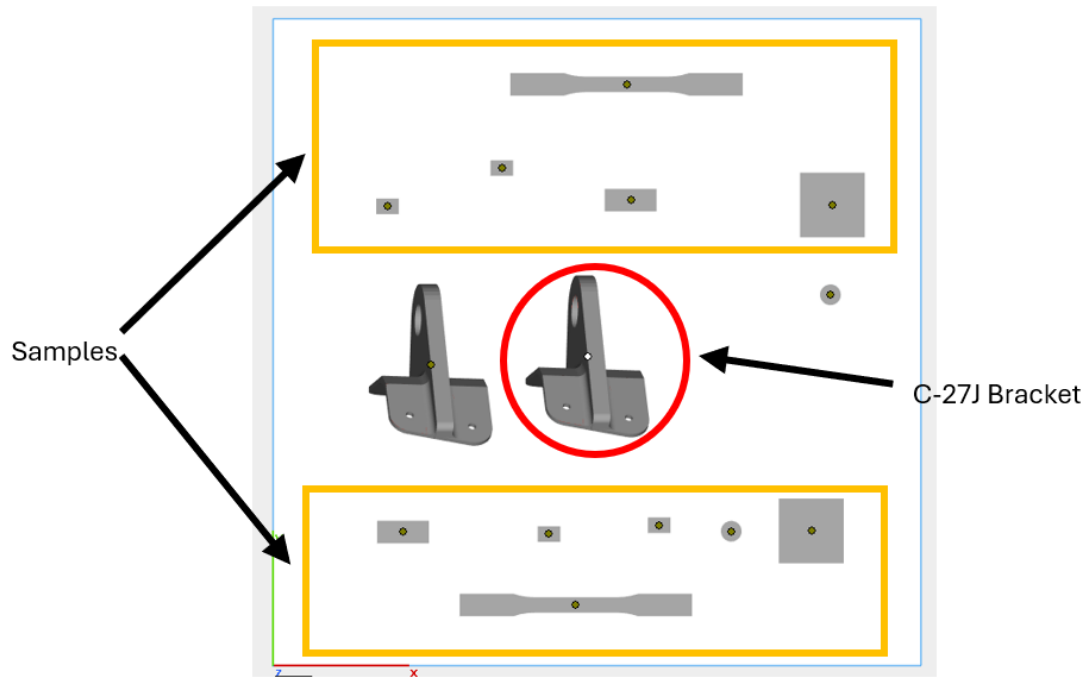
Figure 2.4 – AlSi10Mg job platform top view.
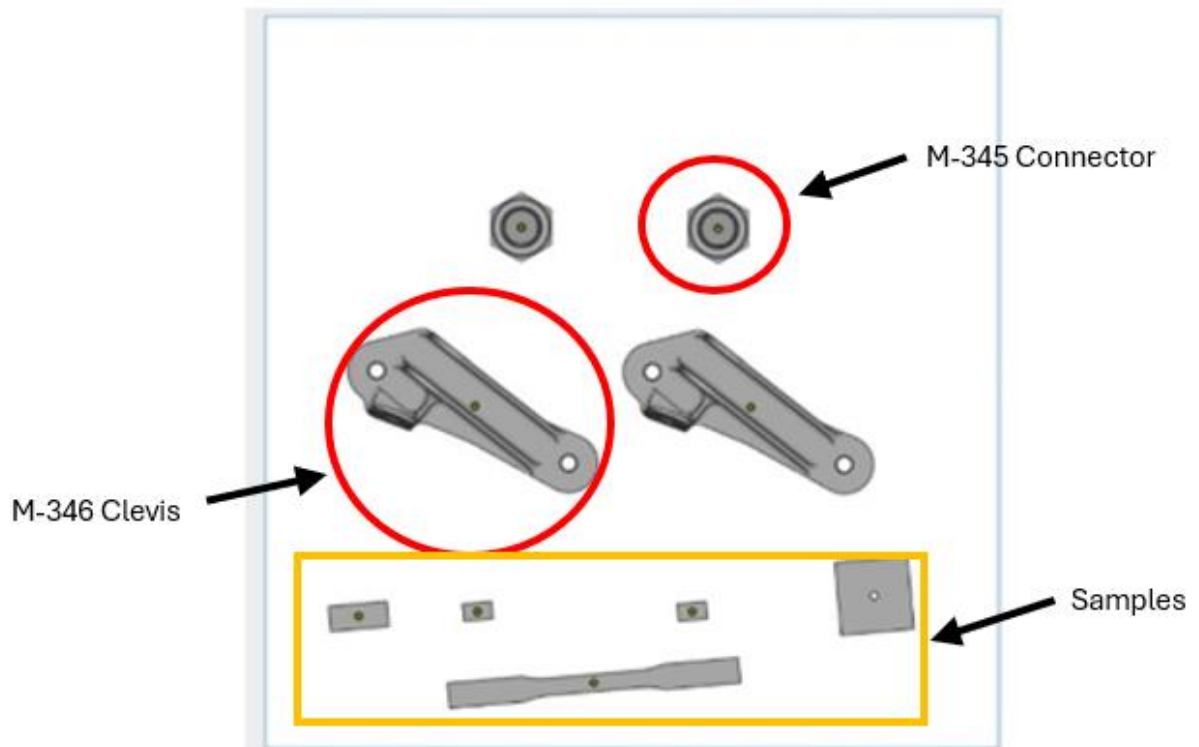
Figure 2.5 – Ti6Al4V job platform top view.

After transferring the use cases, which previously included support and base structures, and the samples in .stl file format from the Magics software to the EOS M270, the LPBF machine, software, the correct position on the print platform was selected for each component. Two main considerations were made:

- Positioning of all components to facilitate EDM cutting.
- Keeping the components at the right distance from each other so that the growth of one does not affect the growth of the other. Taking this into account, *Figure 2.6* and *Figure 2.7* show how the AlSi10Mg and Ti6Al4V use cases jobs have been organized respectively.
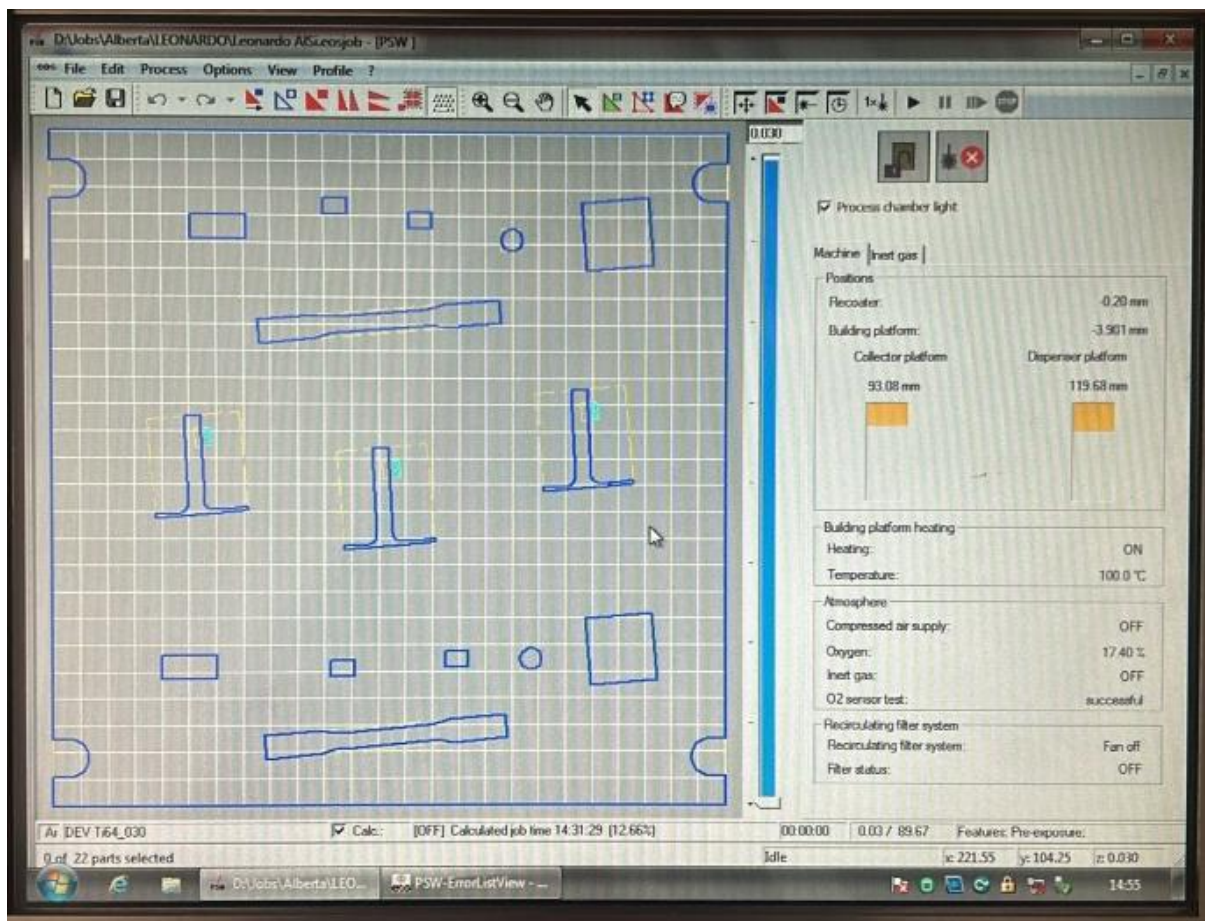
Figure 2.6 – AlSi10Mg EOS M 270 software.
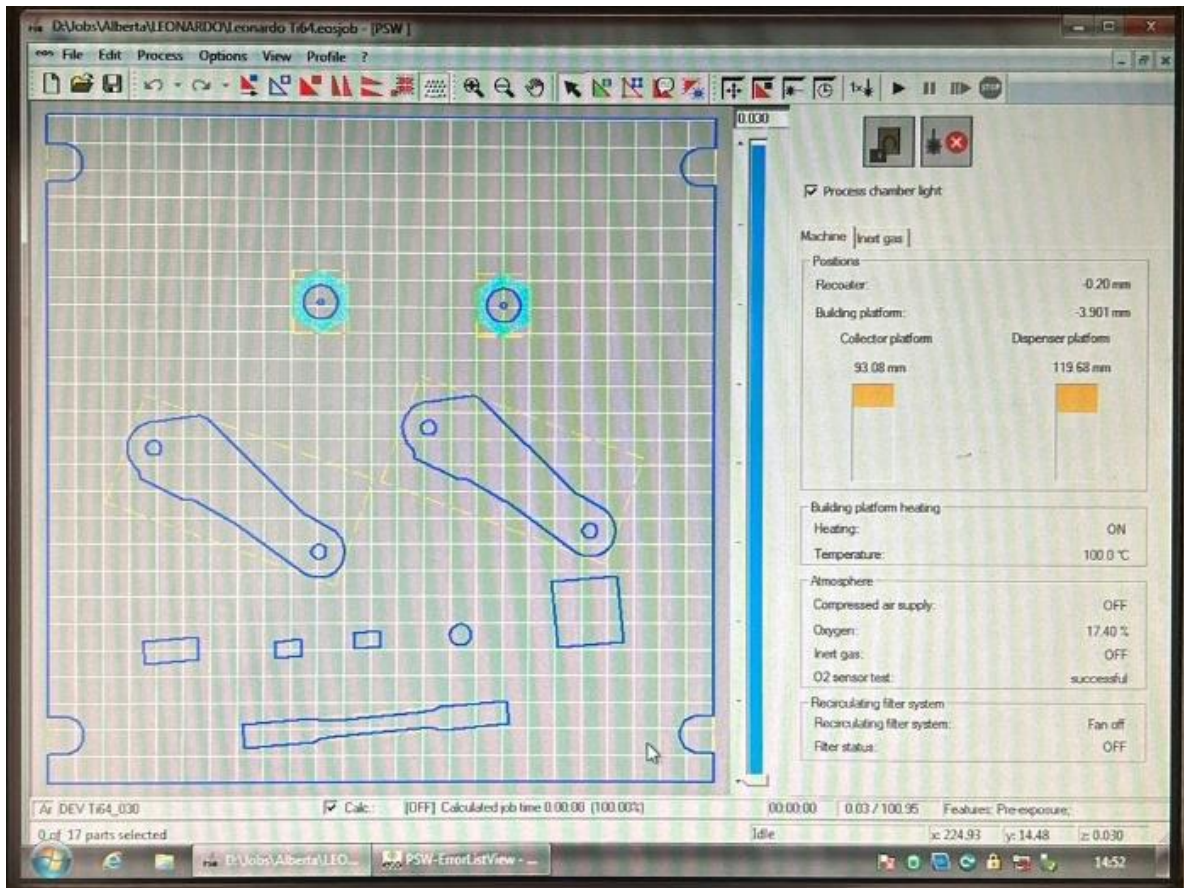
Figure 2.7 – Ti6Al4V EOS M 270 software.

2.1.1   Support structures

When a part is manufactured throughout the LPBF process, you have to take into account that not all parts are self-supporting, especially those with a very complex shape, presence of holes, so they need to be supported; in fact in LPBF process the presence and design of support structures play a critical role in the success of the 3D print. In fact, the main function of the support is structural in order to prevent the risk of the part movement compromising the precision and sustain parts characterized by very steep angles (typically 45° or more) called overhang angles, which would collapse under their own weight.

The are essentially two different types of structural support elements used in LPBF to support the part during the process:

- *Bulk / conventional support*: typically, a solid and dense structure that can provide maximum stability when the part is printed. A disadvantage is that they can be difficult to remove due to the high density of the material (*Figure 2.8*).

- *Lattice support*: porous and cellular structures that use less material than bulk support, saving an amount of powder, and are therefore easy to remove (*Figure 2.9*) [23].
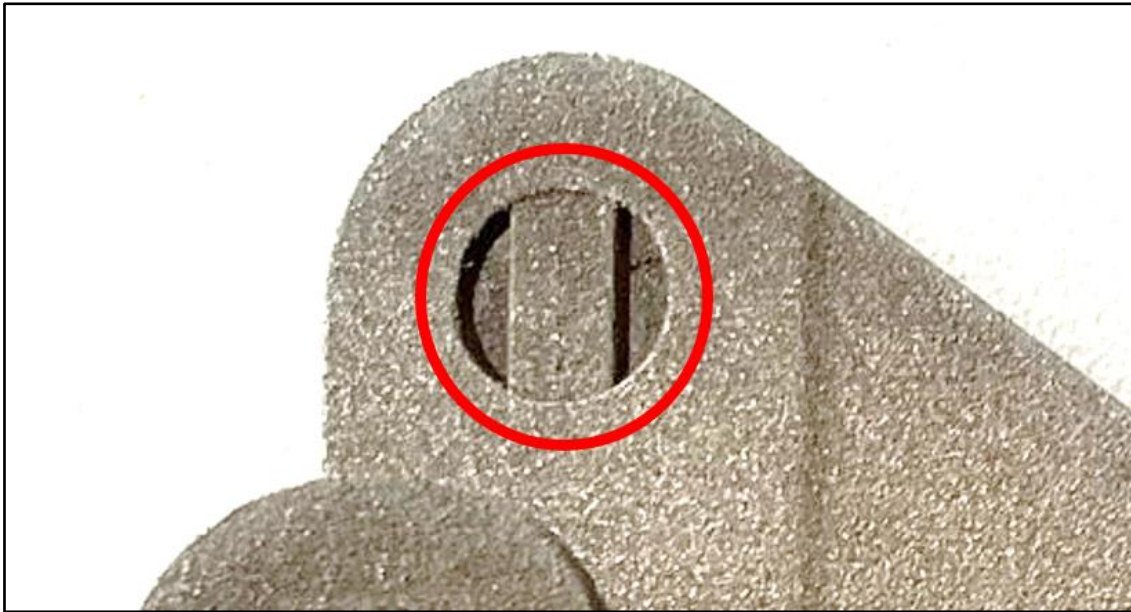
Figure 2.8 – Bulk support on M-346 Clevis.

Figure 2.9 – Lattice support on C-27J Bracket.

2.2 Production of prototypes and control samples via AM

2.2.1   EOS M 270

The jobs produced for this research have been manufactured on an LPBF EOS M 270 (*Figure 2.10*) machine (EOS GmbH, Krailling, Germany) by the Integrated Additive Manufacturing (IAM@PoliTo) Centre of Politecnico di Torino. This machine is equipped with a Yb fiber laser with a power of up to 200 W and a spot size of about 100 μm. The build plate has a build volume of 250 x 250 x 215 mm, the height including the build platform dimension [24].

Figure 2.10 – EOS M 270 LPBF machine.

For AlSi10Mg, the job was carried out with powders supplied by EOS GmbH using standard EOS parameters with a layer thickness of 30 μm in an Ar atmosphere. In the first job, the samples were produced with a steel recoater. It can be seen that two vertical tensile specimens are defective, and this has caused the job to be stopped. These defects are due to the impact of the recoater on the consolidated layer of the specimens during the application of the powder layer. For this reason, a second job was carried out with the same AlSi10Mg powder and the same standard parameters but with a carbon fibre recoater (*Figure 2.11*).

For Ti6Al4V, the job was carried out with powders supplied by EOS GmbH using standard EOS parameters with a layer thickness of 30 μm in an Ar atmosphere, and the use of a steel recoater caused the vertical samples to have defects. For this reason, a second job was carried out (*Figure 2.12*).

For AlSi10Mg the job lasted 18 hours (15 hours for Ti6Al4V job); a total of 25 kg of powder (50 kg for Ti6Al4V) was placed in the machine, which can be reused after sieving.
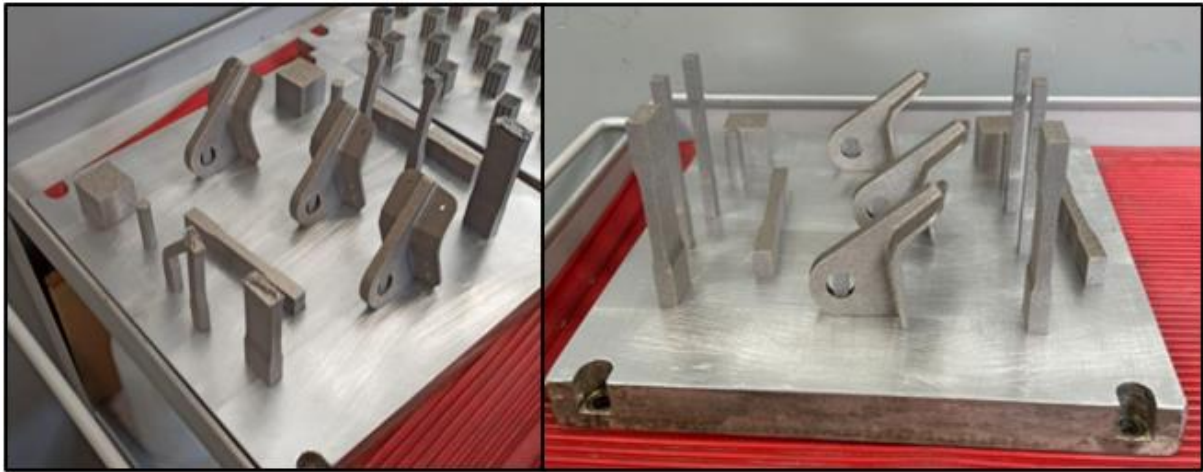
Figure 2.11 – AlSi10Mg job 1 built with steel recoater (left) & job 2 built with carbon fibers recoater (right).

Figure 2.12 – Ti6Al4V job 1 built with steel recoater (left)
& job 2 built with carbon fibers recoater (right).
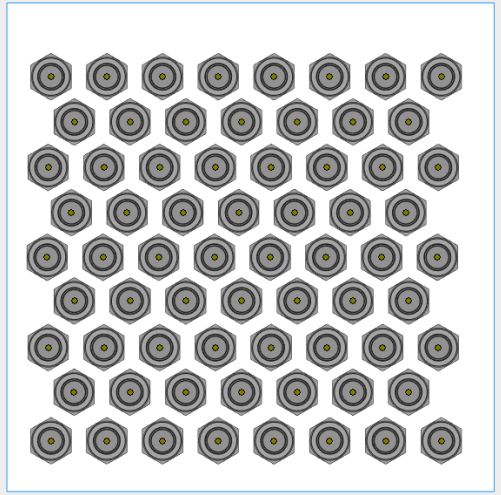
2.2.2   Cost

A cost estimation has been made, taking into account the full production and trying to optimize the AM production (occupying the building platform at best). A model to calculate the costs was used:

- AMOtool a cloud-based application which however does not show the details of the calculation used [25].

The results are shown in the *Table 2.1*.

Table 2.1 – Prevision of cost for the process and components.

	Bracket C-27J Parts: 16 Parts volume: 223.9 cm^3 Supports volume: 12.77 cm^3 Total volume = 236.77 cm^3 Cost bracket: 105 €
	Clevis M-346 Parts: 14 Parts volume: 137 cm^3 Supports volume: 15.2 cm^3 Total volume = 152.2 cm^3 Cost bracket: 96 €
	Connector M-345 Parts: 68 Parts volume: 671.6 cm^3 Supports volume: 296.8 cm^3 Total volume = 968.4 cm^3 Cost bracket: 69 €

2.2.3 Stress-relieving heat treatment

AlSi10Mg and Ti6Al4V were subjected to specific stress relieving and heat treatments in accordance with EOS guidelines. For the stress relieving treatment, the entire aluminium and titanium jobs were placed in the furnace. The aluminum was treated at 300 °C for 1 hour in an uncontrolled atmosphere in the Binder FP115 (TEquipement, Long Branch, New Jersey) heating chamber and the titanium was subjected by a stress-relieved in an ultra-high vacuum furnace (Pro.ba, Cambiano, Italy) (*Figure 2.13*) at 800 °C for 2 hours at a pressure of 10^{-5} bar, this can be considered a true heat treatment.

Figure 2.13 – Heating chamber (left) & Pro.ba furnace used for vacuum heat treatment (right).

Figure 2.14 shows AlSi10Mg and Ti6Al4V stress relieving treatment.
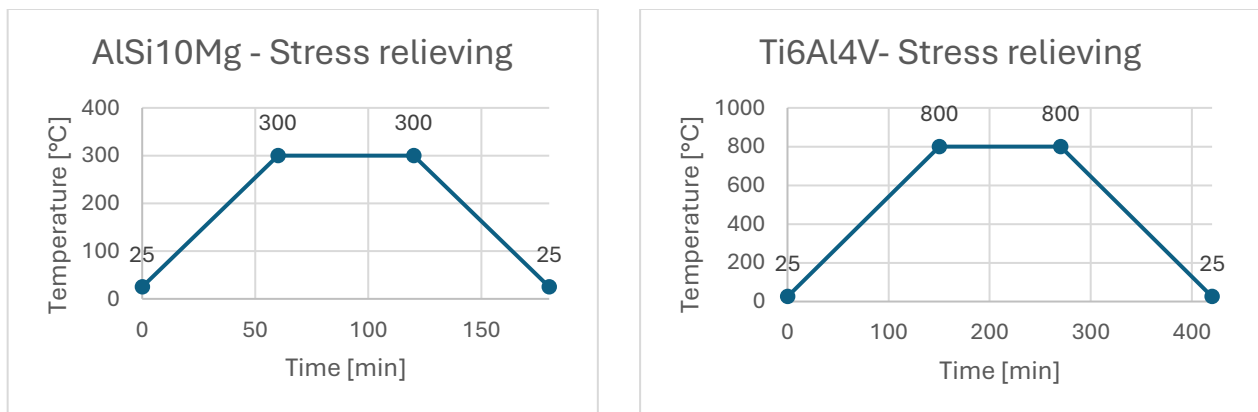
Figure 2.14 – AlSi10Mg (left) and Ti6Al4V (right) stress relieving treatment.

2.2.4   EDM process

EDM is the machining method used to remove the components from the building platform. In particular, a wire EDM machine, the BMW-3000 (Baoma, Suzhou, China) was used (*Figure 2.15*). The wire is an electrode that generates thermoelectric energy by means of a pulsed discharge, which can cut the material by melting and evaporating. The position of the building platform has been studied so that more pieces can be removed from it at the same time to speed up the process (*Figure 2.16*). The major drawback of the EDM process is the penetration of oxygen into the surface of the parts, especially for materials that are prone to oxidation, due to the high local temperatures at the point of discharge. In this thesis case studio, titanium has a high affinity for oxygen due to a reaction that is termodinamically favoured, forming a titania (TiO_2) layer. At high temperatures the oxygen penetrates into the titanium substrate, leading to a gradual increase in oxygen concentration. This leads to undesirable surface characteristics and increased brittleness [26].

Figure 2.15 – BMW-3000 EDM machine
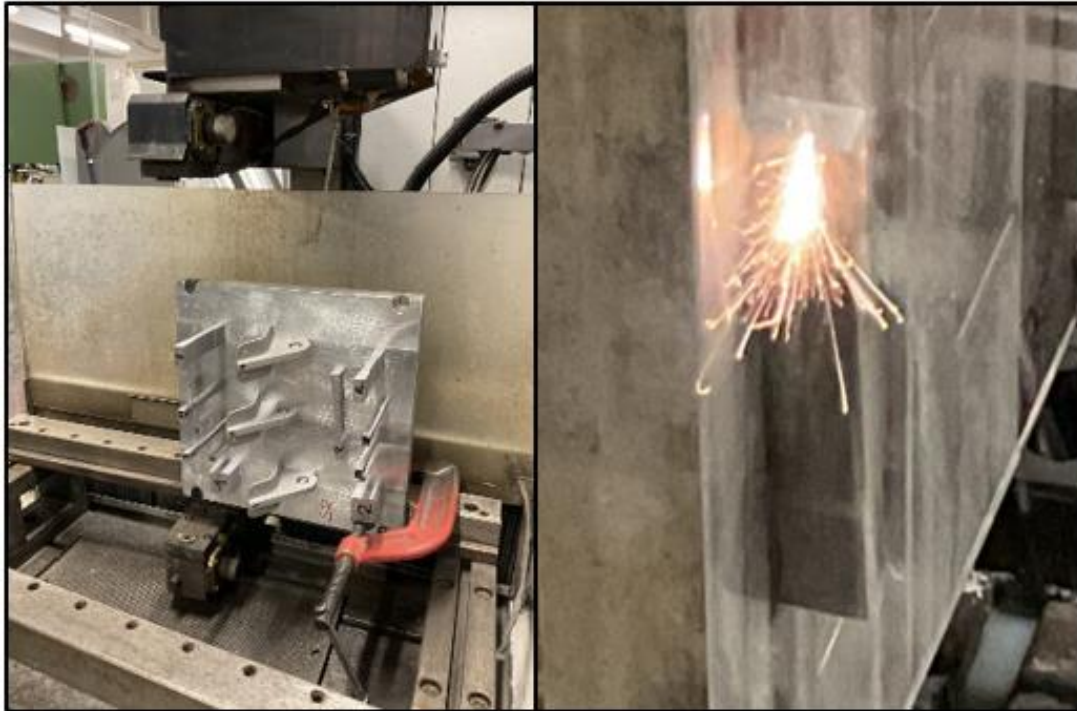
Figure 2.16 – Position of the building platform, in this case Al job, on the EDM machine (left); formation of the sparks during cutting operation (right).

2.2.5   Use cases dimensional control

After removing all the components from the building platform, the significative dimensions of the 3 use cases were measured to confirm the technical drawings. A caliber was used for this purpose (*Figure 2.17*).

Figure 2.17 – C-27J Connector and a caliber.

2.2.6   T6 aluminum heat treatment

Aluminium, in addition to the stress relieving treatment, has been subjected to the T6 heat treatment: annealing at 530°C for 30 minutes, water quenching and artificial ageing at 165°C for 6 hours, this cycle is shown in *Figure 2.18*.
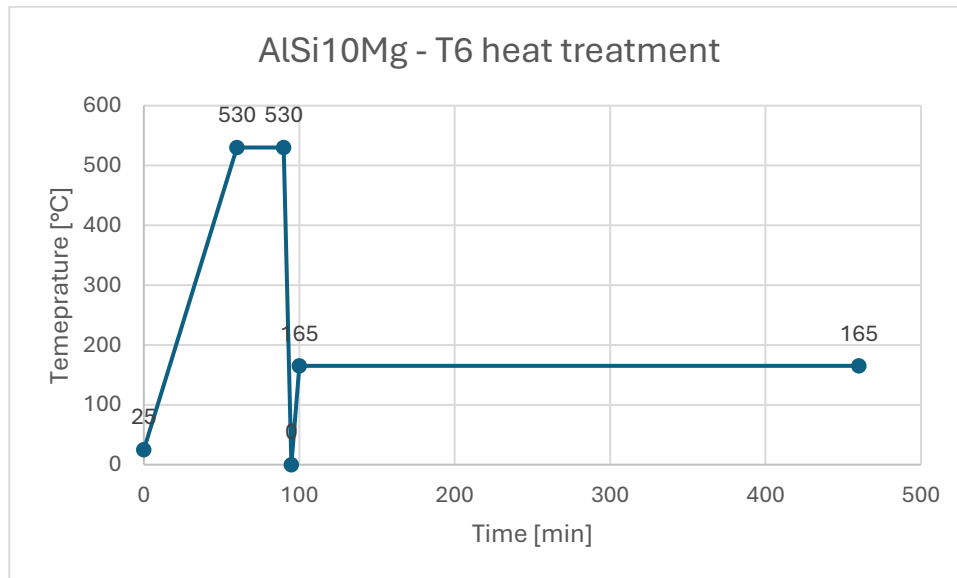
Figure 2.18 – AlSi10Mg heat treatment.

The samples that have been subjected to the heat treatment are the follow:

-   2 horizontal tensile specimens
-   2 vertical tensile specimens
-   2 vertical machined tensile specimens
-   1 cylinder
-   1 cube
-   1 use case

The 530°C is reached in the 30-3000°C tubolar furnace (Nabertherm, Lilienthal/Bremen, Germany) (*Figure 2.19*), after creating a controlled environment in an Ar atmosphere; the aging step is reached in the Binder FP115 heating chamber (*Figure 2.13*).
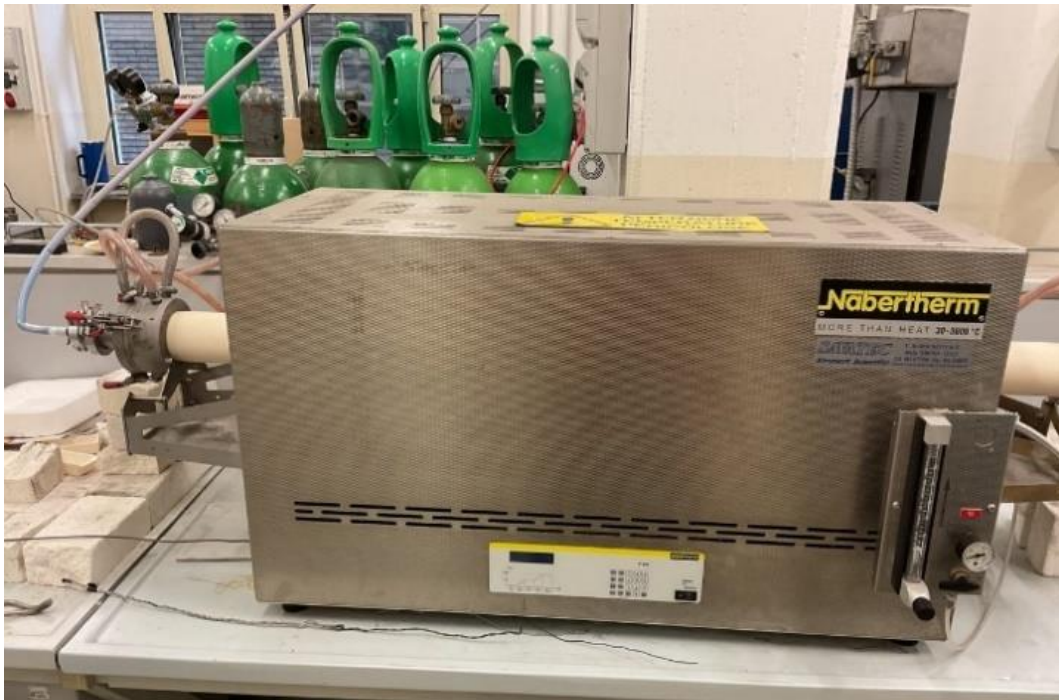
Figure 2.19 – Tubolar furnace.

2.3 Characterization and quality control

All metallographic characterization was carried out in the laboratories of the Department of Applied Sciences and Technologies (DISAT) of the Politecnico di Torino.

2.3.1   Density analysis: the buoyancy method

The buoyancy method was used to measure the density and residual porosity forming during the LPBF process. Residual porosity can also be studied by image analysis software, but this is described after.

For this aim three cubic samples and three cylinders were considered:

- 1 cube of aluminum AlSi10Mg not heat treated;
- 1 cube of aluminum AlSi10Mg heat treated;
- 1 cube of titanium Ti6Al4V;
- 1 cylinder of aluminum AlSi10Mg not heat treated;
- 1 cylinder of aluminum AlSi10Mg heat treated;
- 1 cylinder of titanium Ti6Al4V

The first step has been cutting the cubes into four parts:

- cube 1
- cube 2

- parallelepiped 3
- parallelepiped 4

The operation of cutting has been done by means of a precision cut-off machine, the Brillant 220 (Neurtek, Eibar, Spain) (*Figure 2.20*). The procedure began with selecting the correct specimen holder and then screwing it to the moving platform. The cutting blade was then taken and anchored to the spindle. The cermet blade was chosen to cut aluminum, while the diamond blade was chosen for the titanium due to its greater hardness. The blade must be fixed in such a way that it does not interfere with other objects, except the sample, during the cutting process. Thanks to the control panel it was possible to choose the cutting parameters: *rotation speed*, *feed rate* and *cut length*. Cutting parameters used for AlSi10Mg and Ti6Al4V are reported in *Table 2.2*. Before starting the process, it was necessary to check that the flow rate of the lubricant sprayed onto the blade was correct and that the lubrication was effective, finally the cutting operation started. When the cut was finished, the sample was removed and marked, ready for the next steps.
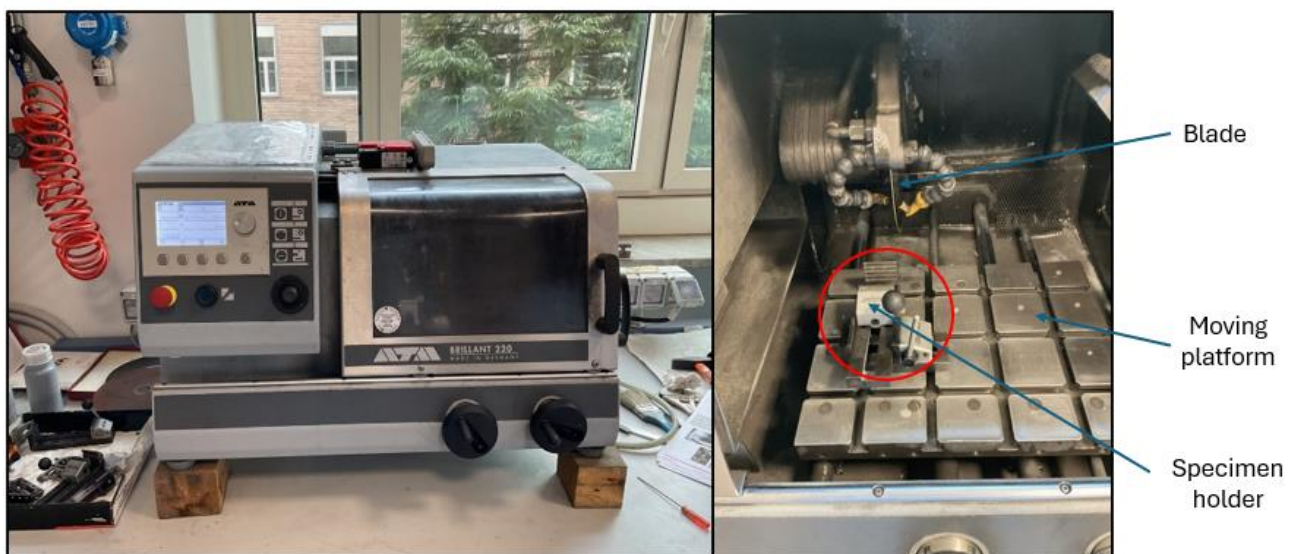
Figure 2.20 – The Brillant 220 cut-off machine (left), detail of the interior machine: blade, moving platform and specimen holder.

Table 2.2 – Cutting parameters.

Material	Rotation speed [rpm]	Feed rate [mm/s]	Cut length [mm]
AlSi10Mg	1600	0.5	150
Ti6Al4V	3200	0.02	150
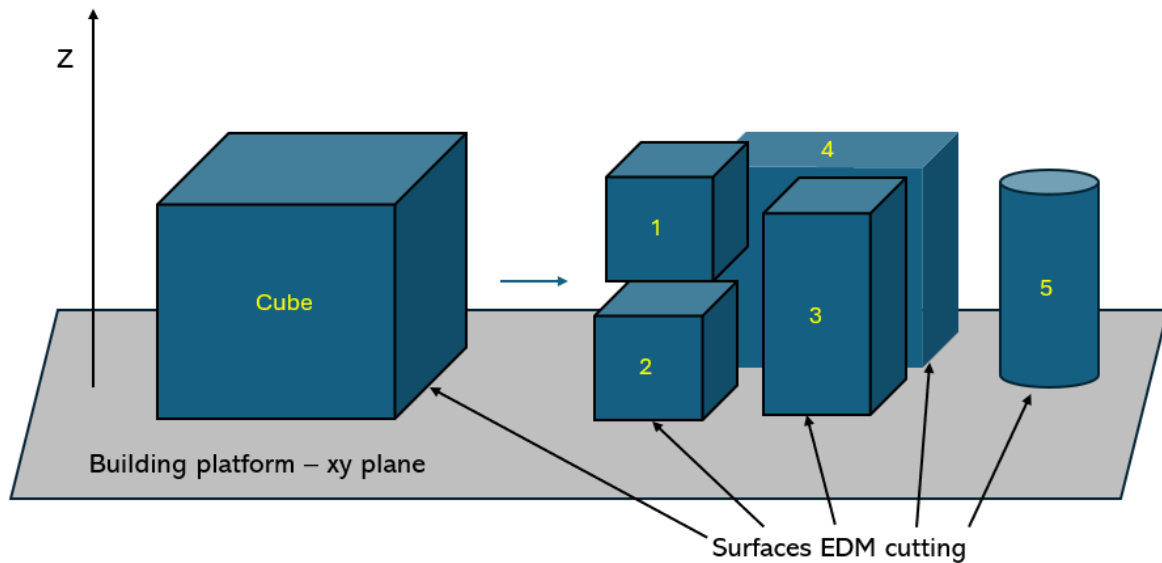
Figure 2.21 – Scheme of cutting to obtain the parallelepiped 3 and cylinder 5 for buoyancy method.

For this test only parallelepiped 3 and cylinder 5 have been considered to calculate density and porosity by buoyancy method, which makes it possible to calculate the *apparent density* (ρ_a), which takes into account the volume of the pores that are present in the material, as opposed to the *true density* (ρ_r), which excludes the voids and considers only the solid part of the material. This method follows the ASTM 962-15 standard method which defines the manner to measure the density of compacted or sintered powder metallurgy pieces using Archimede's principle, which follows the physics of buoyancy [27].

Parallelepipeds were polished beforehand to prevent the roughness from allowing the air molecules to adhere to the sample surface and alter the density measurements, resulting in a lighter component. Each individual sample was then weighed 3 times in air and 3 times in distilled water at room temperature (20°C) using a precision balance (0.1 mg). The ρ_a was calculated using the following formula:

$$\rho a = \frac{W}{W - W_{H2O}}$$

where W is the weight of the sample in air, W_{H2O} is the weight of the sample in the water. *Figure 2.22* shows the equipment used for the buoyancy method.
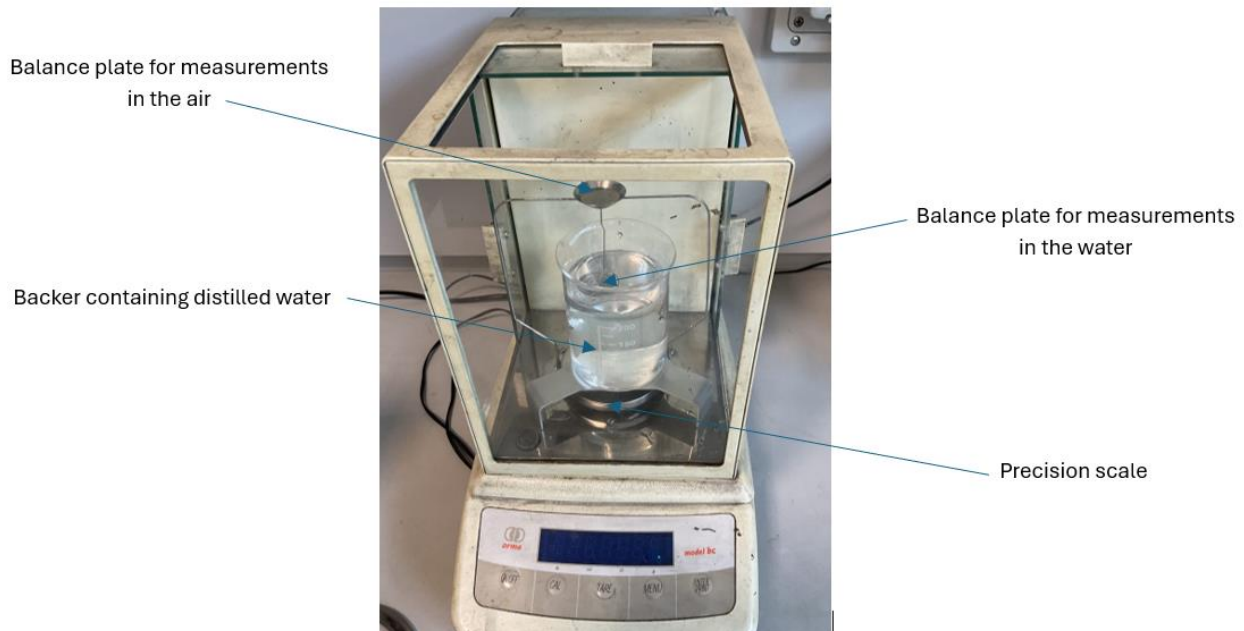
Figure 2.22 – Equipment for measuring the density by means the buoyancy method.

2.3.2 Metallographic preparation

In order to be analyzed by optical microscope (OM) and scanning electron microscope (SEM), the specimens are subjected to a careful metallographic preparation procedure that includes *mounting*, *polishing* and *chemical etching*.

Prior to these operations, the surfaces to be analyzed were selected: the surface perpendicular xy (S_{xy}) and parallel xz (S_{xz}), to the direction of growth of the LPBF process must be studied in order to compare the dependence of the microstructure from the direction considered. Cube 1 and Cube 2 have been selected for this purpose. To sum up 6 cubes have been considered:

- cube 1 of aluminum no heat treated for S_{xy} (*Al_SR_xy*)
- cube 2 of aluminum no heat treated for S_{xz} (*Al_SR_xz*)
- cube 1 of aluminum heat treated for S_{xy} (*Al_SR_HT_xy*)
- cube 2 of aluminum heat treated for S_{xz} (*Al_SR_HT_xz*)
- cube 1 of titanium for S_{xy} (*Ti_SR_xy*)
- cube 2 of titanium for S_{xz} (*Ti_SR_xz*)

2.3.2.1 Mounting

Hot mounting was carried out using an automatic hydraulic encapsulating press, the IPA 30 (Remet, Casalecchio di Reno, Bologna) (*Figure 2.23*).

Figure 2.23 – IPA 30.

The conductive resin was chosen for the mounting because the samples need to be analyzed by SEM microscope, and the conductive resin is able to dissipate the electrical charges from the electron beams, improving the quality of the images (*Figure 2.24*). Fully automatic, the cycle has been controlled by an easily programmable microprocessor, set at 7 minutes and 155°C to cure the resin and obtain the mounted sample. The thermic cycle used for the mounting process is reported in *Figure 2.25*. The mounting is a fundamental step that allows the samples to be handled better during the polishing phases, giving better results than hand polishing without mounting.

Figure 2.24 – Conduttive resin.
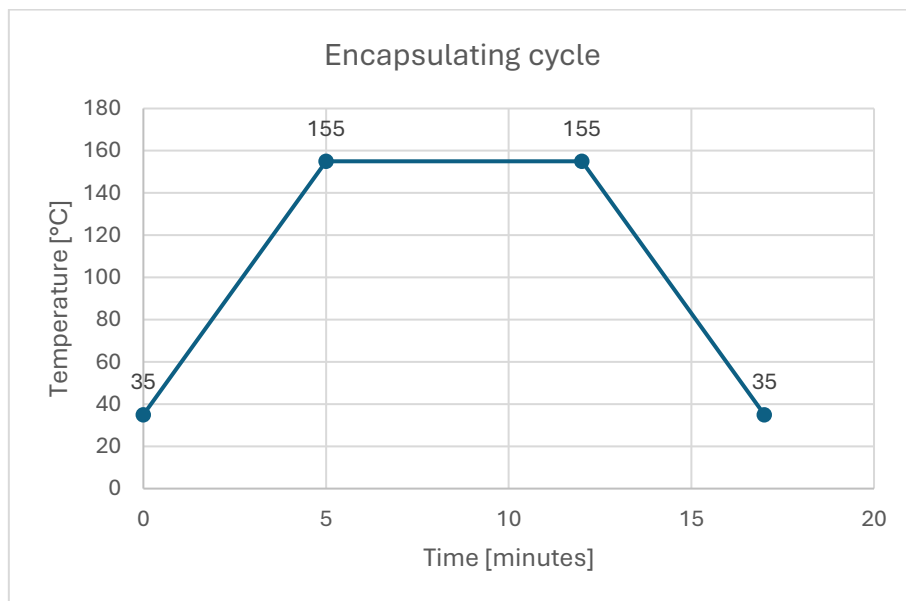
Figure 2.25 – Encapsulating cycle of the inglobation process.

2.3.2.2   Lapping and polishing

Lapping and polishing steps were carried out with the Mecatech 234 automatic polishing machine (Presi, Eybens, France) (*Figure 2.26*).

Figure 2.26 – Mechatech 234 machine.

The machine can be set up using these parameters:

- *head speed [rpm]*
- *plate speed [rpm]*
- *forced imposed on the samples [N]*

Considering that aluminum is softer than titanium, a lower force must be imposed; lapping parameters are reported in *Table 2.3*.

Table 2.3 – Lapping parameters.

Material	Head speed (rpm)	Plate speed (rpm)	Force (N)
AlSi10Mg	150	100	1
Ti6Al4V	150	100	2

During lapping step, on the machine, SiC abrasive papers with progressively smaller grits were mounted: 180, 400, 800, 1200, 2400, 4000, chosen according to the softness of the material and the condition of the surface. This allows to remove the lines on the metallographic surface and forms new ones of lesser depth with each pass. The polishing step was carried out using 2 different cloths for

each material, wetted with a colloidal silica emulsion. Two different emulsions were prepared for Al and Ti, the volume fraction (%V) of each as shown in *Table 2.4*.

Table 2.4 – Volume fraction of the emulsions used for the polishing step.

Material	Colloidal silica SiO_2 (V%)	Water H_2O (V%)	Hydrogen peroxyde H_2O_2 (V%)
AlSi10Mg	50	50	0
Ti6Al4V	35	35	30

After polishing operation, the samples were ready for the optic microscope images acquisition (*Figure 2.27*).
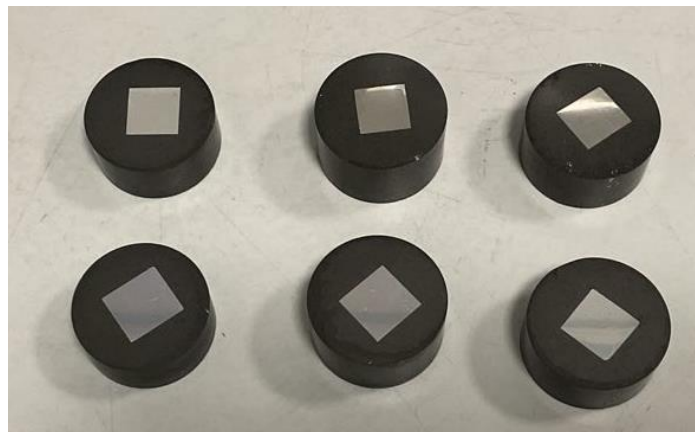
Figure 2.27 – AlSi10Mg and Ti6Al4V samples after the polishing step.

2.3.3   Optical microscope

For the acquisition of images at medium magnification it has been used the DMI 5000M (Leica Microsystems GmbH, Wetzlar, Germany) optical microscope (*Figure 2.28*) which allows magnification from 50x to 1000x. This instrument has been used at different moments during the thesis work for:

- Evaluate residual porosities and their shapes, see *section*s *3.1.5* and *3.2.5*.

- Assess morphology and microstructure before and after the etching step, see *sections 3.1.7* and *3.2.7*.

- Evaluate the porosity homogeneity on the use cases surfaces after cutting and polishing them, see *sections 3.1.10* and *3.2.11*.

Figure 2.28 – DMI 5000M Leica optical microscope.

2.3.4 Etching operation

The analysis of the microstructure is fundamental to understand the effects of the building process and of the heat treatment on the materials and to explain its mechanical properties. A sample, even if well-polished, cannot show its microstructure, so it must be subjected to an etching step, using an attaching reagent. For aluminum and titanium Keller's reagent and Kroll's reagent were used respectively. The compositions of the two reagents are the follows:

- Keller's solution: 90-95% Water (H_2O), 5-10% Nitric Acid (HNO_3), 5-10% Hydrogen Cloride (HCl), 1-5% Hydrogen Flouride (HF) [28].
- Kroll's solution: 90-95% Water (H_2O), 4-8% Nitric Acid (HNO_3), 1-5% Hydrogen Flouride (HF) [29].

These operations were carried out under a chemical hood to work in a ventilated and enclosed environment to limit exposure to toxic substances coming from the reactions.

The sample was immersed in the etching reagent for 10 seconds and then rinsed with water to remove any chemical residual (*Figure 2.29*).

Figure 2.29 – Etching agent and water inside the chemical hood.

2.3.5 Stereomicroscope

The utilization of the Leica EZ4W stereomicroscope (*Figure 2.30*), that is able to reach lower magnification (20x and 35x), has been useful for:

- Analyzing the microstructures, see *sections 3.1.7 and 3.2.7*.
- To control the fracture surface, see *sections 3.1.9 and 3.2.9*.
- Control of the overall internal porosities of use cases after cutting and polishing operations, see *sections 3.1.10* and *3.2.11*.

Figure 2.30 – EZ4W Leica stereomicroscope.

2.3.6 SEM analysis

For this research the Scanning Electron Microscope (SEM) Phenom XL (Alphatest, Cernusco sul Naviglio, Italy) (*Figure 2.31*) was used. The SEM analysis was conducted on the 6 mounted samples. The instrument was equipped with the Energy Dispersive Spectroscopy (EDS). Images were taken in Back Scattered Diffraction (BSD), Secondary Electron Diffraction (SED) and EDS modes to determine the chemical composition, surface topology and specific chemical composition of the samples.

Figure 2.31 – Phenom XL.

2.3.7 XRD analysis

XRD measurements were carried out using a Panalytical Empyrean diffractometer (Malvern Panalytical, Malvern, UK) (*Figure 2.32*) using a Bragg–Brentano geometry and Cu-Kα radiation at 40 kV and 40 mA. The measured was performed in a 2θ range between 30◦ and 110◦, with a step size of 0.013 ◦/s and a time step of 60 s.

The measurements were carried out on the xy-cross sections of *Al_SR*, *Al_SR_HT* and *Ti_SR* tensile vertical samples.
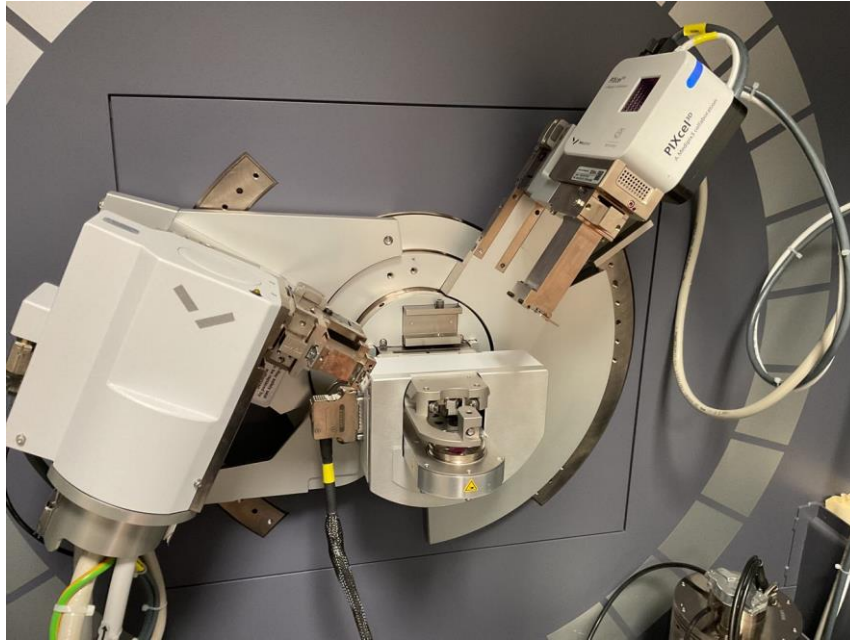
Figure 2.32 – Malvern Panalytical.

2.3.8   LECO analysis

The chemical composition of Ti6Al4V after the EDM process changes so the concentration of interstitial elements in the sample was measured using an inert gas fusion infra-red absorption LECO 736 O/N analyzer (LECO corporation, Michigan, USA), (*Figure 2.33*).

Figure 2.33 – LECO 736 O/N analyzer.

Considering *Figure 2.21* sample 4 was taken and 2 cubes test specimens were extracted (A,B) as shown in *Figure 2.34*. The dimensions of the specimens have been carefully chosen as the instrument is capable of analyzing a quantity of material in the range 200-500 mg and the density of Ti6Al4V is 4.5 g/cc.
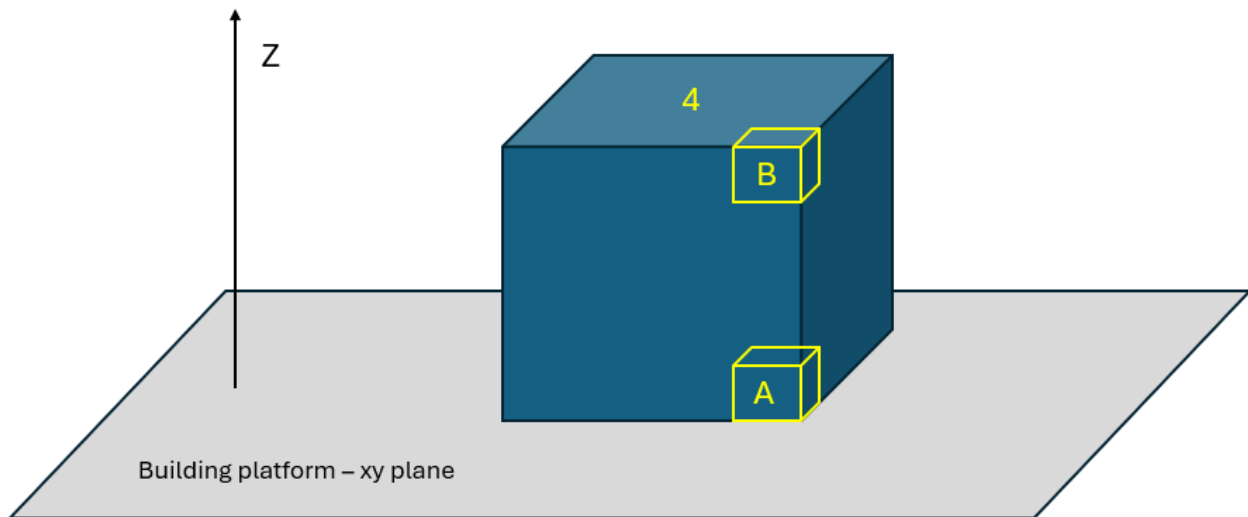
Figure 2.34 – Cube for LECO analysis.

2.3.9   Mechanical test

The mechanical tests were carried out in the laboratory of the Politecnico di Torino in Alessandria Campus. In particular, the experimental tests were:

- Tensile tests
- Hardness tests

2.3.9.1   Tensile tests

The mechanical tensile tests were carried out on the tensile specimens, using the Z100 (ZwickRoell, Genova, Italy) tensile machine (*Figure 2.35*).

In particular there were tested:

- For aluminum: Al_H_SR, Al_H_SR_HT; Al_V_SR, Al_V_SR_HT;
- For titanium: Ti_H_SR, Ti_V_SR, Ti_V_machined_SR.

For each typology 2 specimens were tested. Prior to the tensile test, all machined specimens were sanded with the abrasive papers to reduce the typical roughness created during EDM operation and the risk that it could be the point of crack nucleation, altering the test values.

Figure 2.35 – Zwick Z100 tensile machine.

After the tensile tests, the fractured specimens were subjected to surface fracture analysis. Studying the topology of the surface fracture is useful to know if it is ductile or brittle, and if the porosities distribution generates a path that can cause the tensile specimen to rupture.

The stereomicroscope and FESEM instruments were used for this purpose.

2.3.9.2   Surface fracture analysis at stereomicroscope

Images of the surfaces were taken using the EZ4W stereomicroscope (*Figure 2.30*) at 12x magnification to cover all surface fractures.

2.3.9.3   Surface fracture analysis at FE-SEM

Images of the fracture surfaces were taken using the TESCAN S9000G FSE-SEM (Atomikateknik, Ankara, Turkey) (*Figure 2.36*) to know the topology. The chamber dimensions are 340 mm (width) × 315 mm (depth) × 320 mm (height), making it suitable for large sample analysis. It can achieve a resolution of 0.7 nm at 15 kV acceleration voltage.

The images were taken in Secondary Electron (UH resolution) using 200x, 1200x, 2000x, 5000x, 20000x 50000x magnifications and only the most significant were selected.
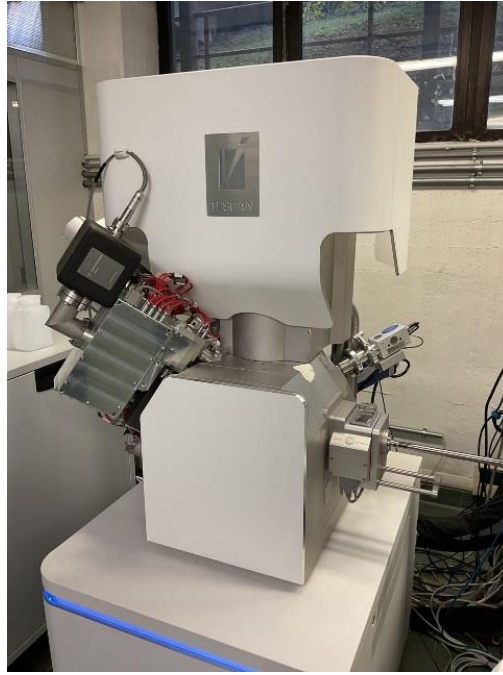
Figure 2.36 – UHR FE-SEM microscope.

2.3.9.4   Hardness tests

The hardness test was executed using the MGU 025 durometer (EMCO-TEST GmbH, Hallein Osterreich) (*Figure 2.37*) on the *parallelepiped 3* samples (*Figure 2.21*) for:

- Al_SR
- Al_SR_HT
- Ti_SR

Figure 2.37 – MGU 025 durometer.

For this test, a Hardness Vickers (HV) diamond tip was selected in accordance with the ASTM E92 standard [30] and by measuring the lengths of the two diagonals (*Figure 2.38*), it was possible to obtain the HV values. The calculation of the hardness is done according to the following formula:

$$HV = \frac{1.8544}{9.80665} \times \frac{F}{d^2}$$

Where 'F' is the force applied [N] and 'd' is the diagonal mean length [mm].
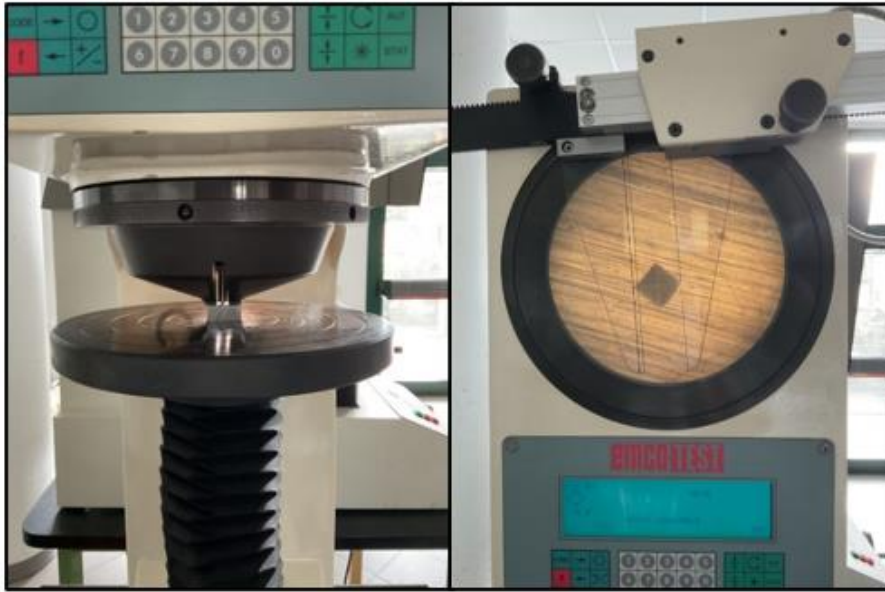
Figure 2.38 – Sample indentation (left); diagonals measurement (right)

2.3.10   Roughness test

Roughness was measured by using contact methods using the T1000 profilometer (Hommel Etamic, Tonisvorst, Germany) (*Figure 2.39*).
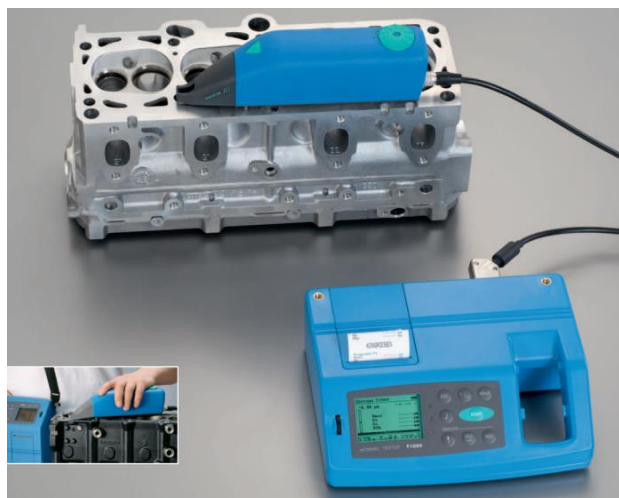
Figure 2.39 – T1000 profilometer.

In particular the *Roughness Average* (*Ra* or *Rq*) and Roughness *Ten Point Height of Irregularities* (*Rz*) were calculated. They are defined as follows:

- Ra: arithmetic average of the absolute values of the profile heights over the evaluation length.
- Rz is the average value of the absolute values of the heights of five highest-profile peaks and the depths of five deepest alleys within the evaluation length.
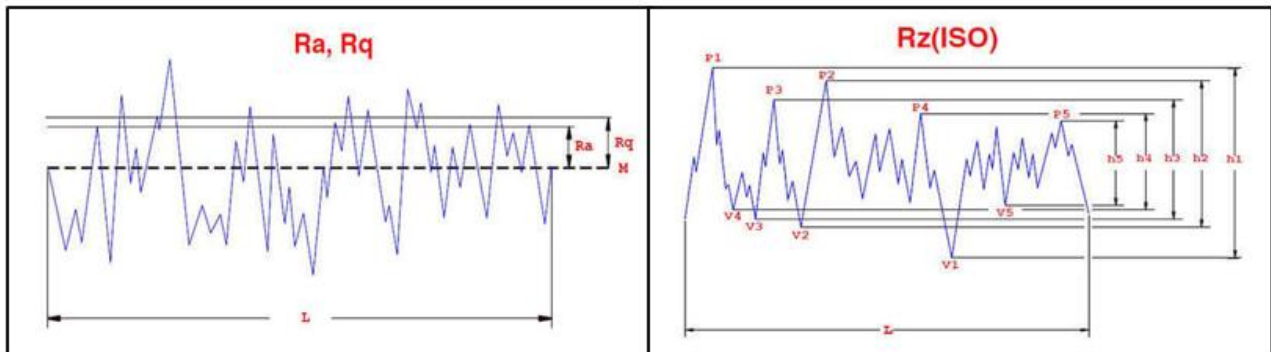
Figure 2.40 – Ra (left) roughness; Rz (right) roughness. [31]

The Rz definition is reported for completeness but is not considered in the analysis of results. Roughness measurements were performed on XY, XZ and YZ surfaces of Al and Ti cubes and on some selected surfaces of the use cases

Chapter 3
RESULTS AND ANALYSIS
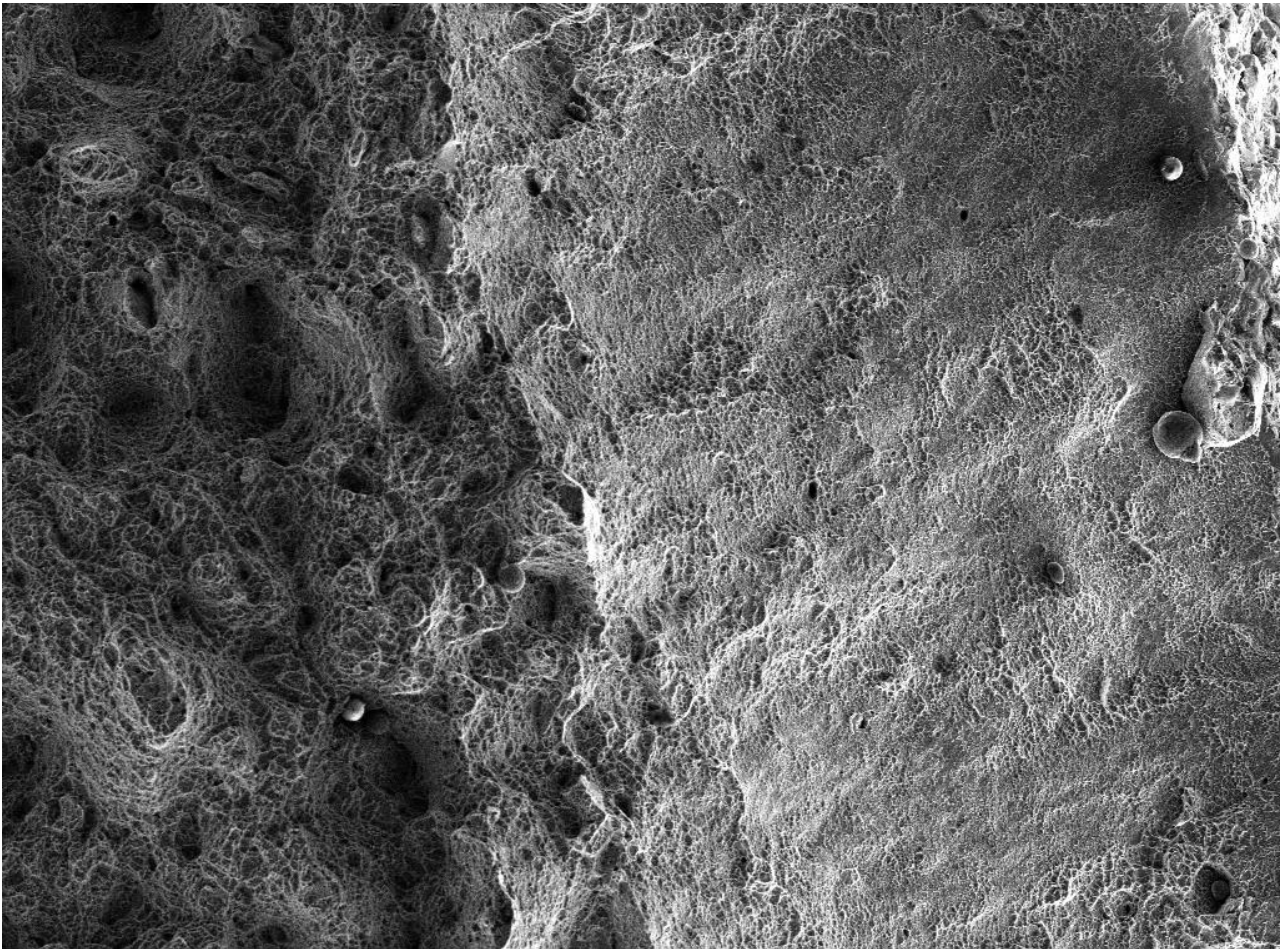
3. RESULTS AND ANALYSIS

3.1 Aluminium

3.1.1   Bracket dimensional inspection

The dimensions of the Bracket are not disclosed as they are the intellectual property of Leonardo S.p.A. *Figure 3.1* shows technical drawing and use case dimensions. In *Table 3.1* the dimensions that correspond to those in the technical drawing are marked with a ✓, if compliant or ✗, if not compliant.
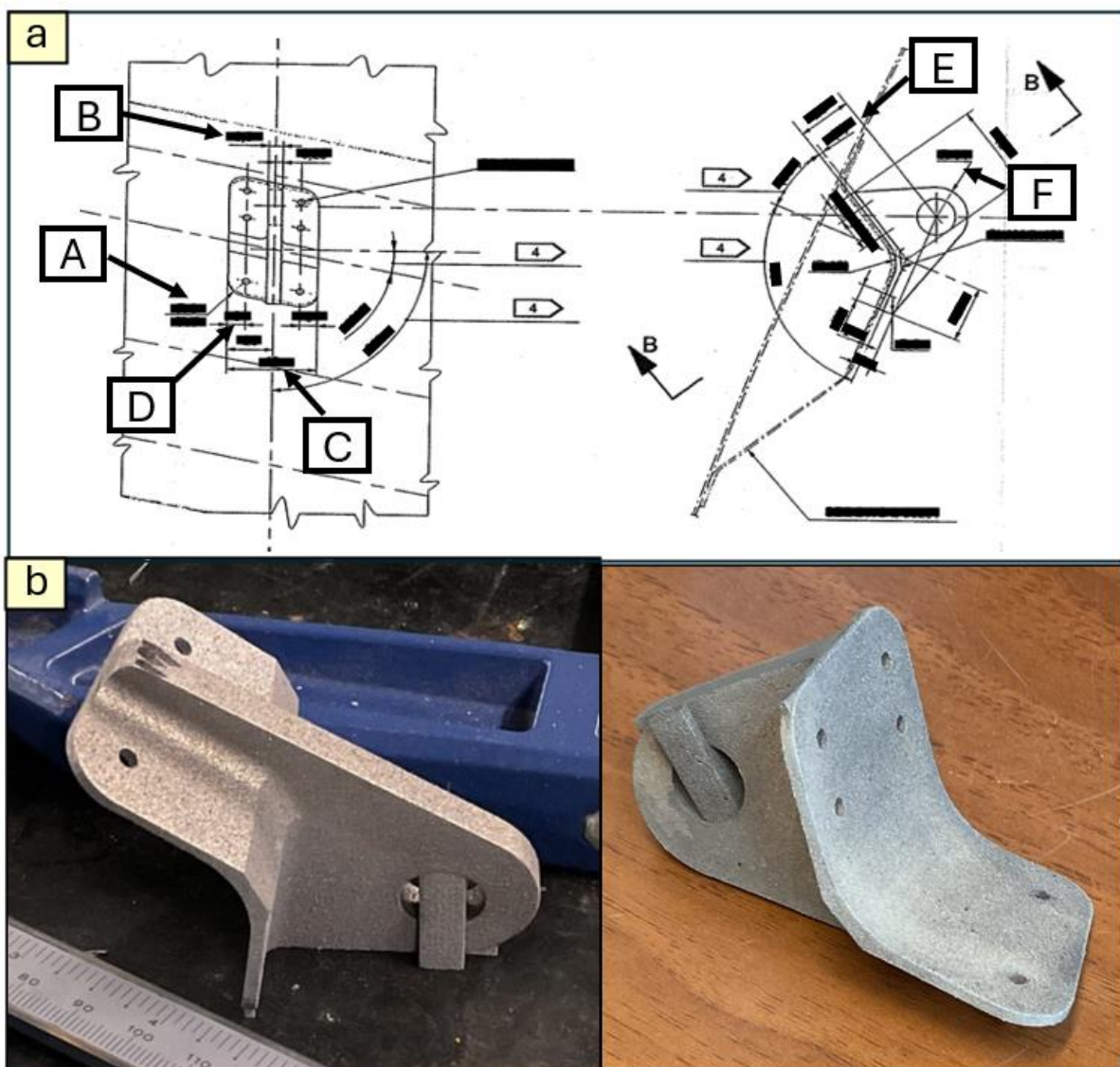
Figure 3.1 – (a) Technical drawing dimensions (© Leonardo S.p.A.) (b) Bracket prospective.

Table 3.1 – Bracket dimensional checking.

Bracket dimensions	Compliant
A	✓
B	✓
C	✓
D	✓
E	✓
F	✗

Only the 'F' dimension does not correspond to the technical drawing. That is because the CAD model, which the part was built from, was purposely design in such way to allow for precise subsequent machining of the main hole in order to accurately install the bearing that connects it to the rod. For this reason, the as-built use case can be considered fully compliant.

3.1.2 Tensile test
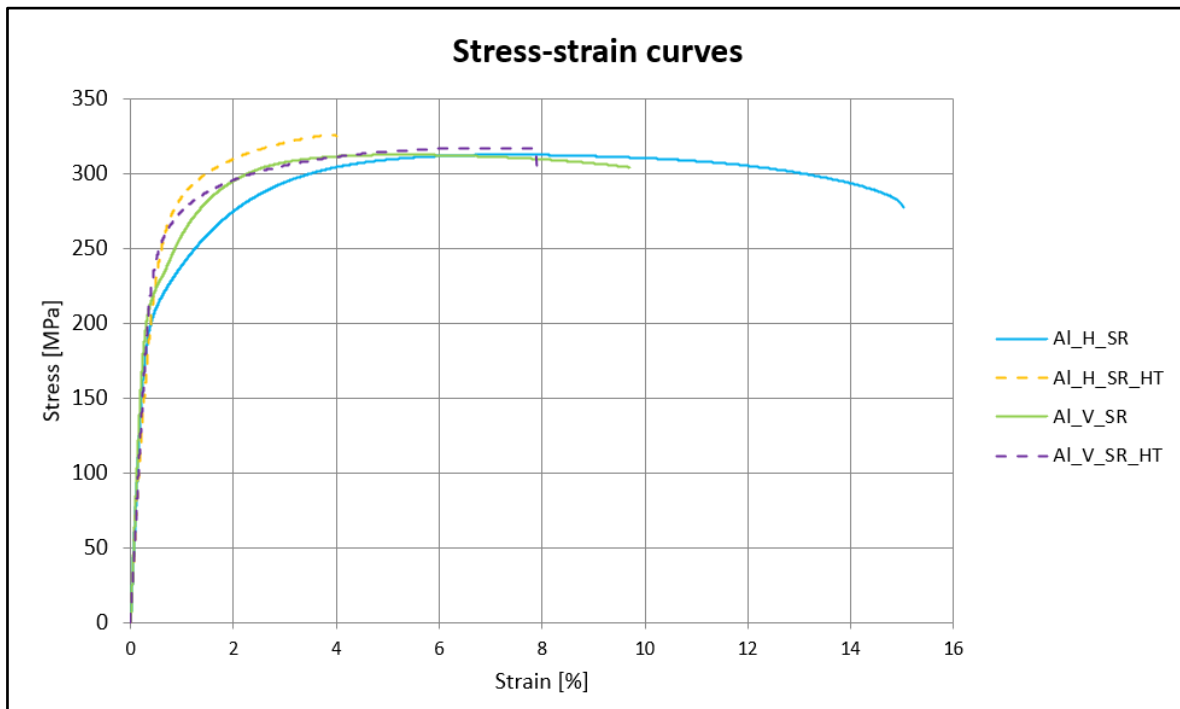
Figure 3.2 – AlSi10Mg Stress-strain curves.

Figure 3.3 – AlSi10Mg (a) YS (b) UTS (c) A% histograms.

Figure 3.2 shows the stress-strain curves of tensile specimens. The curves show that considering samples of the same typology (the 2 horizontals and the 2 verticals), the YS and UTS increase after the HT. This is confirmed by the values reported in *Figure 3.3a* (YS) and *Figure 3.3b* (UTS). In general, there is an increase of about 50 MPa for YS and 10 MPa for UTS. This confirms the goodness of the T6 heat treatment in improving the strength. The strength values obtained by this thesis work are in linear with those shown for EOS and higher with respect PoliTO in *section 1.5.9*. On the other hand, as shown in *Figure 3.3c* the A% is reduced. Although this reduction of A% was not reported in the EOS datasheet, it is in line with the general rule according to which an increase in YS and UTS is generally associated with a reduction in A%. This is due to the precipitation of strengthening phases (Mg$_2$Si) that reduce the dislocation motion. The A% reduction observed in the case of Al_H_SR_HT suggests however that the sample might contain some pores that cause a premature failure during the tensile tests. Moreover the Al_H_SR has the highest value of ductility.

3.1.3   Hardness test

The hardness and tensile properties have direct proportionality. As reported in [32] the relationship between HV and the yield strength YS approximately follows the equation

$$HV \sim 3 \cdot YS$$

As can be seen from the tensile test (*section 3.1.2*), the HT improves the mechanical properties. This is confirmed by the hardness test: in *Table 3.2* it can be seen that the Al_SR_HT hardness values are about 10 points higher than those of Al_SR.

Table 3.2 – Comparison of AlSi10Mg HV-hardness before and after the HT.

Test	Al_SR hardness [HV]	Al_SR_HT hardness [HV]
1	102	116
2	100	113
3	103	114
4	101	113
Average	101.5 (±1.3)	114 (±1.4)

3.1.4   Roughness test

There is a strong interdependence between surface orientation and laser incidence, resulting in different roughness values on surfaces with different orientations. *Figure 3.4* compares the roughness along the 3 directions of the cube faces and that of the Bracket. The roughness along the XY plane, i.e. the plane parallel to the bed of molten powder, has a lower roughness value than those on the XZ and YZ faces. This is justified by [33] which reports the influence of surface orientation in relation to laser incidence on the surface roughness. Modifying the laser relation angle ζ, i.e. the angle between the surface normal vector ($\vec{n}$) and laser incidence vector ($\vec{l}$), (*Figure 3.5*) changes the roughness and consequently surfaces with different orientations have different roughness. In addition, gravity can increase the roughness of overhanging surfaces. The Bracket has value of roughness that can be confronted with XY a XZ plane roughness, taking into account the standard deviation. All values of roughness presented in the histograms are slightly higher than preferred, it is therefore recommended to polish all surfaces down to below 10 μm.
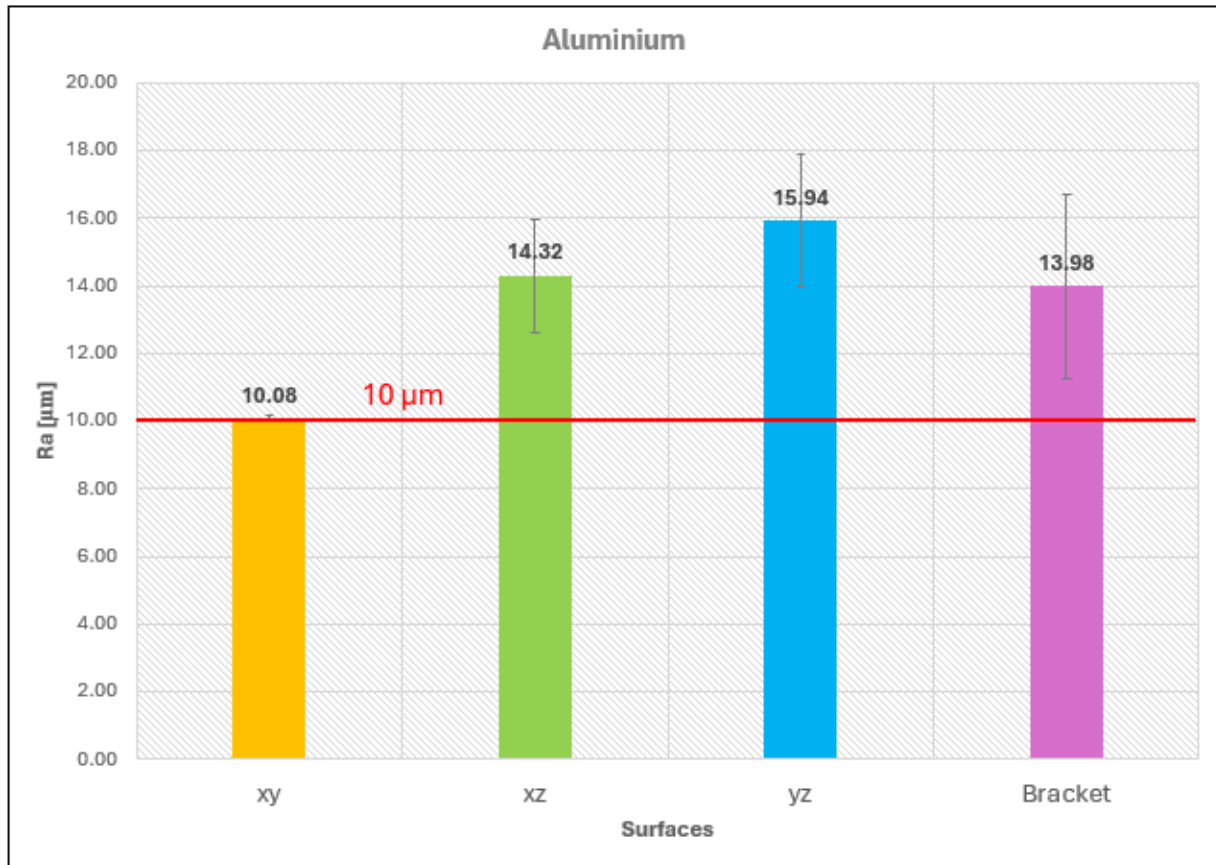
Figure 3.4 – Ra comparison among xy.xz,yz planes and the Bracket surfaces.
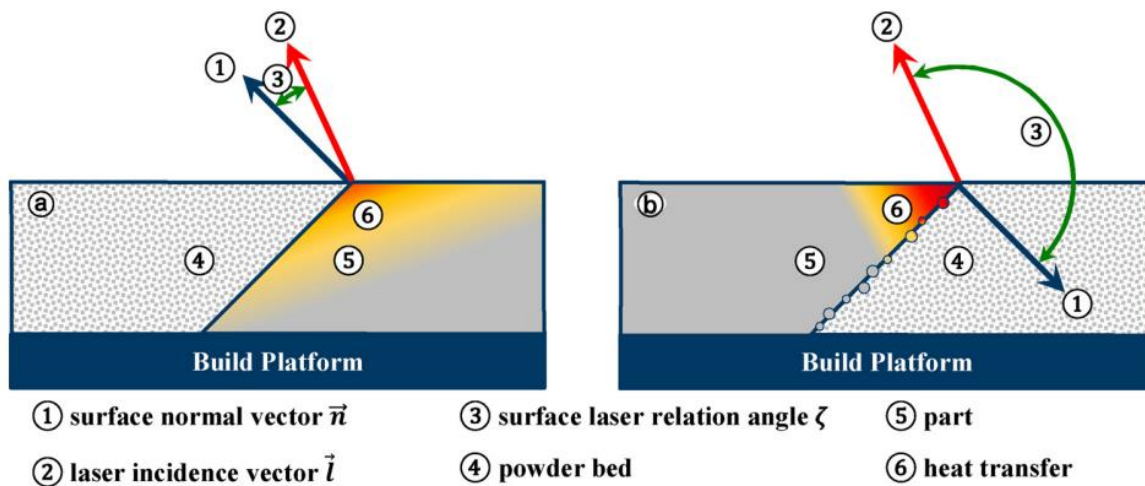
Figure 3.5 – Laser relation angle ζ.

3.1.5 Porosity and Aspect Ratio

The buoyancy method provides a practical estimate of porosity but does not give accurate results due to the presence of closed pores, water adsorption, material solubility and air trapped in pores. For this reason, porosity was also calculated using image analysis software, *ImageJ* after capturing images from the OM.

Using the first method the data of porosity percentage (P%) of parallelepiped 3 and cylinder 5 (*Figure 2.21*) are shown in *Table 3.3*.

Table 3.3 – AlSi10Mg porosity percentage by buoyancy method.

	Al_SR, P%	Al_SR_HT, P%
Parallelepiped 3 (polished)	0.79 (± 0.07)	0.95 (± 0.07)
Cylinder 5 (unpolished)	1.17 (± 0.07)	1.21 (± 0.12)

Two main considerations can be made: the polished sample (parallelepiped 3) has lower values than the unpolished sample (cylinder 5), this is since the roughness of the surface can adsorb the water molecules and alter the measurements; the heat treatment does not affect the porosity as it is not high enough to start the sintering process.

Figure 3.6 shows micrographs of the porosity of Al_SR taken by using OM. Two main types of porosity are highlighted: the circular shape (green circled) and the irregular shape due to the lack-of-fusion phenomenon (red circled) which is typically present along the growth layers (XZ plane).
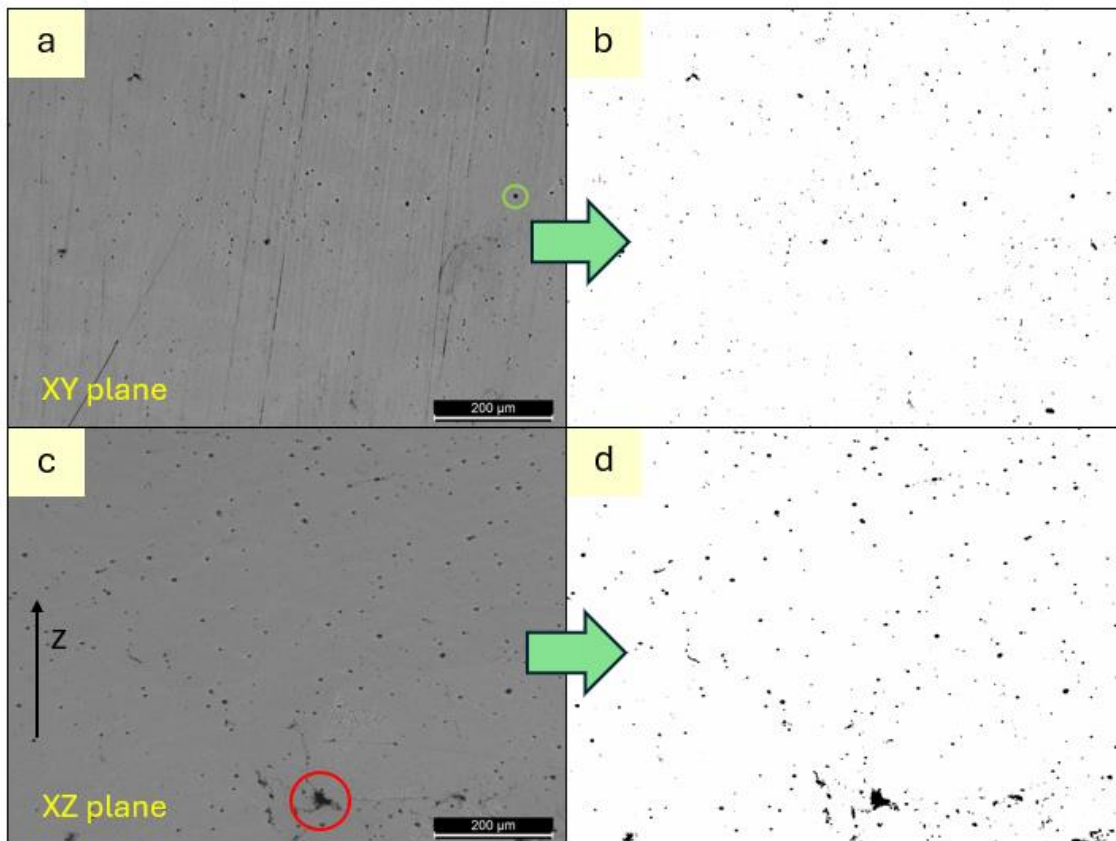
Figure 3.6 – Porosity images on the Al_SR (a) XY plane (b) XY plane after ImageJ elaboration; (c) XZ plane; (d) XZ plane after ImageJ elaboration.

Table 3.4 shows the values of P% obtained using the ImageJ software; the values, considering the standard deviation, are at least equal to those previously obtained using the buoyancy method. The aspect ratio values found reveal that there is a higher amount of more elongated pores in the XY-plane than in the XZ-plane.

Table 3.4 – Al_SR Porosity and Aspect Ratio by optical microscope.

	P%	**Aspect Ratio (l/L)**
XY plane	0.40 ($\pm$ 0.12)	0.56 ($\pm$ 0.06)
XZ plane	0.72 ($\pm$ 0.07)	0.62 ($\pm$ 0.02)

These values are in linear with those found by [34].

3.1.6   Phases

The study of the phases that compose the AlSi10Mg alloy LPBF T6 HT has been carried out by means of an XRD analysis. *Figure 3.7* shows the XRD peak features of the alloy considered.
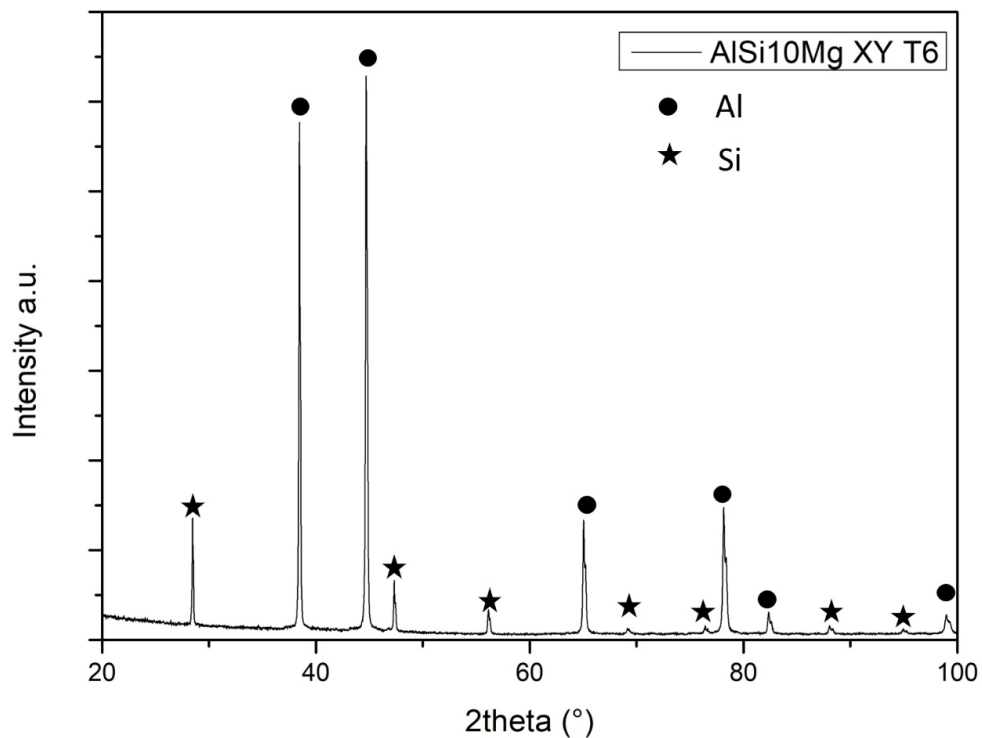
Figure 3.7 – AlSi10Mg XRD spectrum.

The characteristic peaks of Al and Si are visible. Those of aluminum are the diffraction peaks of the α-Al phase forming the matrix and have the highest intensity values, while those of silicon do not have high intensity values because they represent the Si particles dispersed in the α-Al matrix. The presence of these phases is confirmed by microstructure, see *section 3.1.7*, and chemical composition analysis, see *section 3.1.8* .

3.1.7   Microstructure analysis

The characterization of the microstructure is important to get an indicative idea of the properties of the material. In this thesis a general analysis of the microstructure has been done using *Stereomicroscope*, *OM* and *SEM* instruments (*Figure 3.8*). The main characteristic that has been investigated is the effect of the T6 HT modifying the AlSi10Mg silicium network microstructure to a more homogeneous one. The dispersion of Si is due to the increase in diffusivity during solutioning.
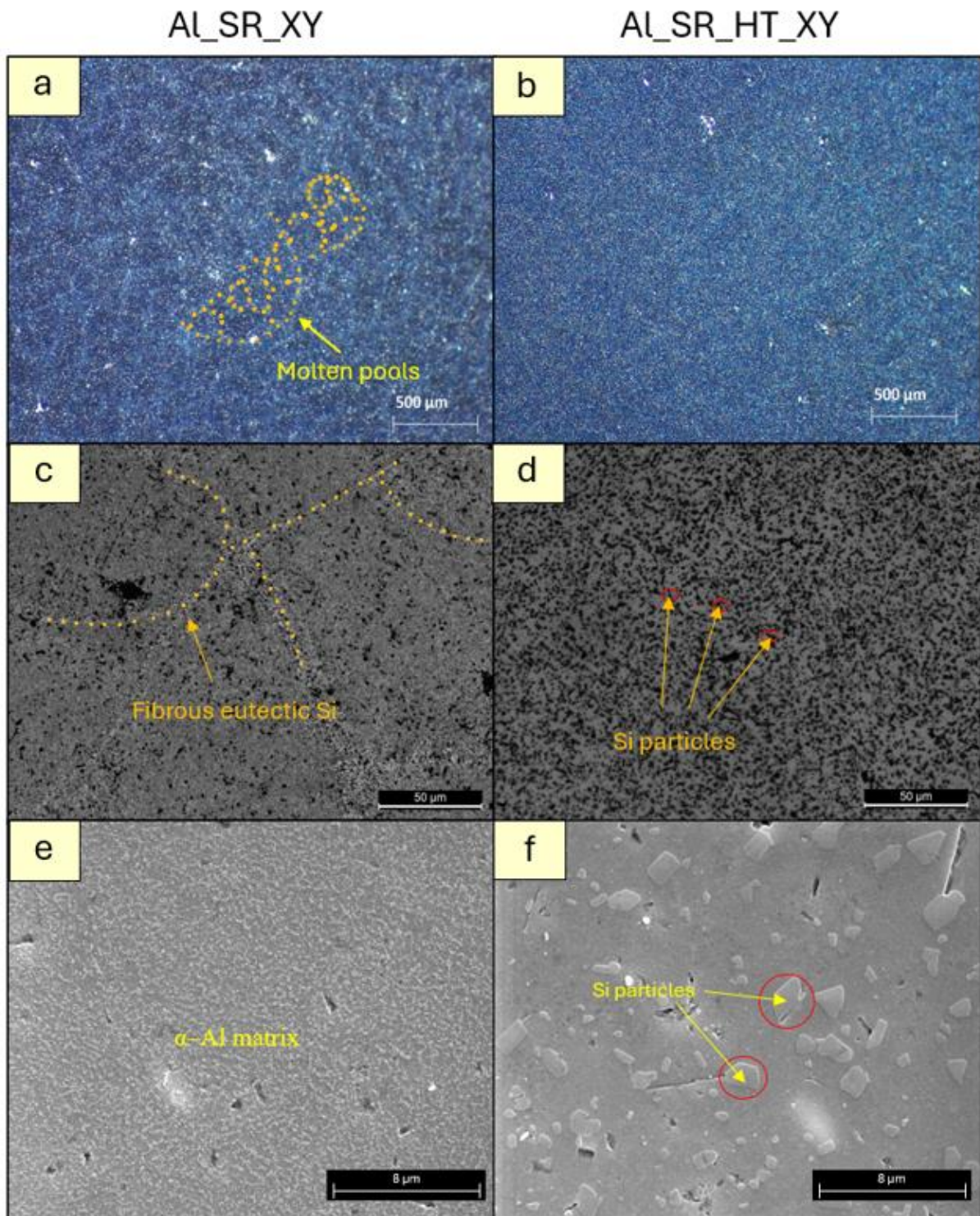
Figure 3.8 – AlSi10Mg microstructure : a) SR at stereomicroscope, b) SR_HT at stereomicroscope, c) SR at OM, d) SR_HT at OM, e) SR at SEM-SED, f) SR_HT at SEM-SED along the XY plane.

Considering stereomicroscope and optic microscope images (*Figure 3.8(a-c)*), it is evident that the molten pools, which were visible in the SR state , disappeared after the T6 HT (*Figure 3.8(b-d)*). This process is clearly visible in the SED images where the microstructure changes from an α-Al cells

surrounded by reticular Si (*Figure 3.8e*) to an α-Al matrix with Si particles of 2-3 μm size inside due to the coalescence phenomenon (*Figure 3.8f*). The same conclusion is supported by [15].

3.1.8 Chemical composition

An EDS mapping analysis was carried out to confirm the formation of Si agglomerates after the T6 HT. An EDS linear analysis was then performed on a specific area of the image to further confirm the chemical nature of these agglomerates.
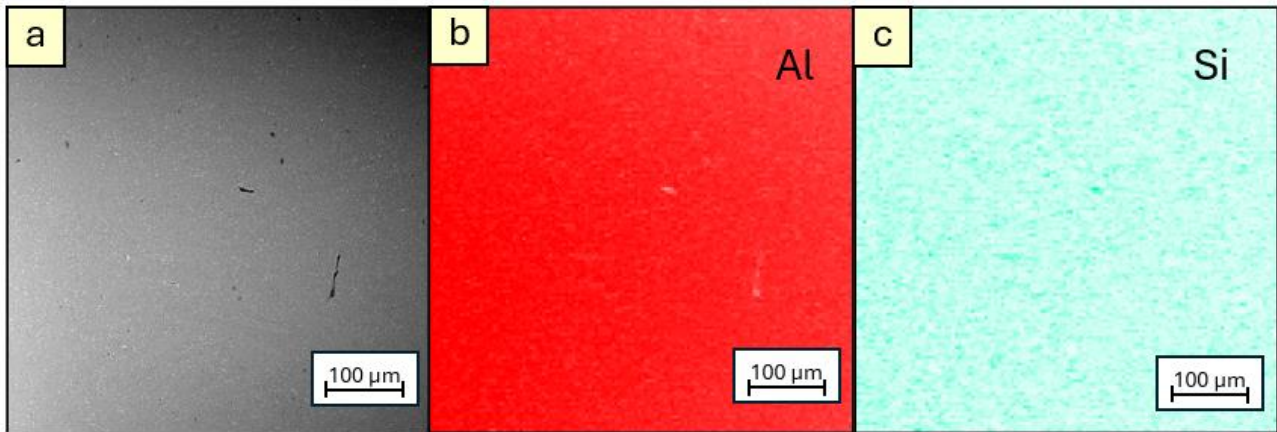
Figure 3.9 – EDS mapping of Al_SR: (a) area considered (b) Al mapping (c) Si mapping.
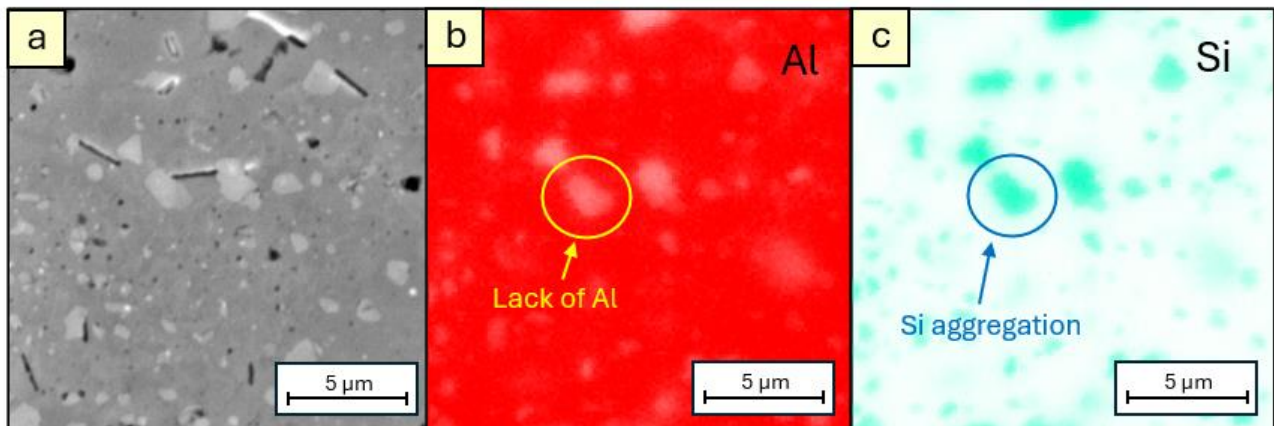
Figure 3.10 – EDS mapping of Al_SR_HT: (a) area considered (b) Al mapping (c) Si mapping.

Figure 3.9 shows the distribution of the alloying elements of the sample before it was subjected to HT. At this magnification, there is a homogeneous distribution of Al and Si elements throughout all the sample. *Figure 3.10* shows the chemical distribution of Al and Si of the sample after HT. The coalescence phenomenon of Si particles occurs during T6. The Si particles are indicated by a higher blue intensity, blue circled (*Figure 3.10c*), which corresponds to a lighter red color intensity in the aluminum mapping, yellow circled (*Figure 3.10b*).

An EDS linear image analysis was carried out considering the same area that was circled in the EDS mapping analysis. There is the contemporary dip of the Al intensity curve value and the peak of the Si intensity curve (*Figure 3.11*). This confirms the results of the previous analysis.
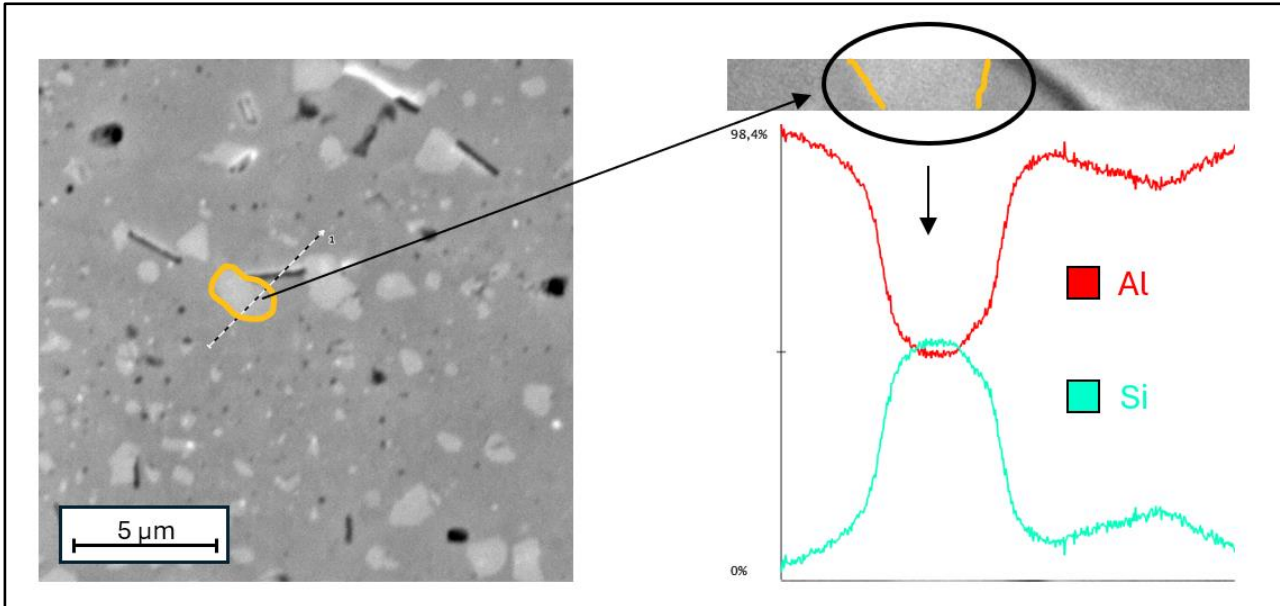
Figure 3.11 – EDS linear analysis: Si intensity peak in correspondence of yellow particle.

3.1.9   Fracture surface analysis
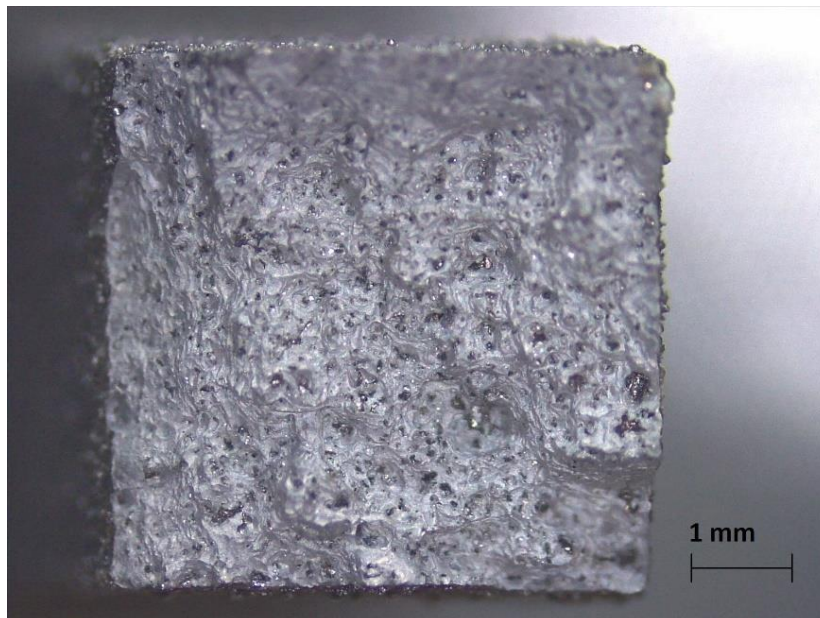
Figure 3.12 – Fracture surface of a AlSi10Mg tensile specimen by stereomicroscope.

As a metal, aluminum is subject to plastic deformation. During deformation, new voids are formed in the material, in addition to those already present from the LPBF process, in specific areas of higher

stress, such as around inclusions, defects, or grain boundaries. Deformation causes these cavities to grow and coalesce, resulting in fracture. FESEM micrographs were used to study this.
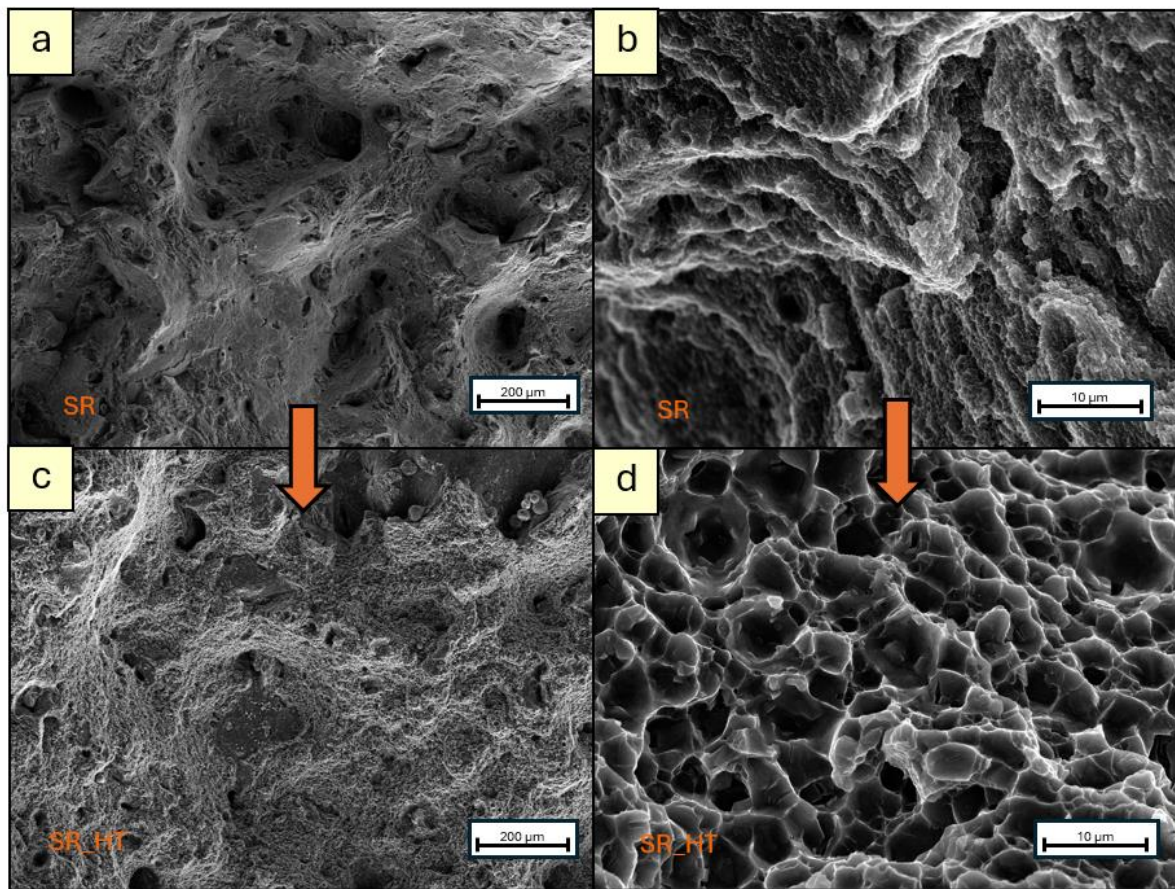
Figure 3.13 – Surface fracture of a) Al_H_SR 200x b) Al_H_SR 5000x c) Al_H_SR_HT 200x d) Al_H_SR_HT 5000x at FESEM.

Figure 3.13 shows a comparison of the microstructures of the horizontal tensile specimens before and after HT: in fact, two FESEM micrographs at different magnifications are shown in the upper part and compared with those in the lower part. The SR material presents a microstructure very similar to the as-built one, i.e. the dimples are small (~ 1 µm) and irregularly shaped due to the rapid cooling during the LPBF process (a-b), whereas after HT a smoother surface with larger dimples (~ 5 µm) formation can be observed (c-d).
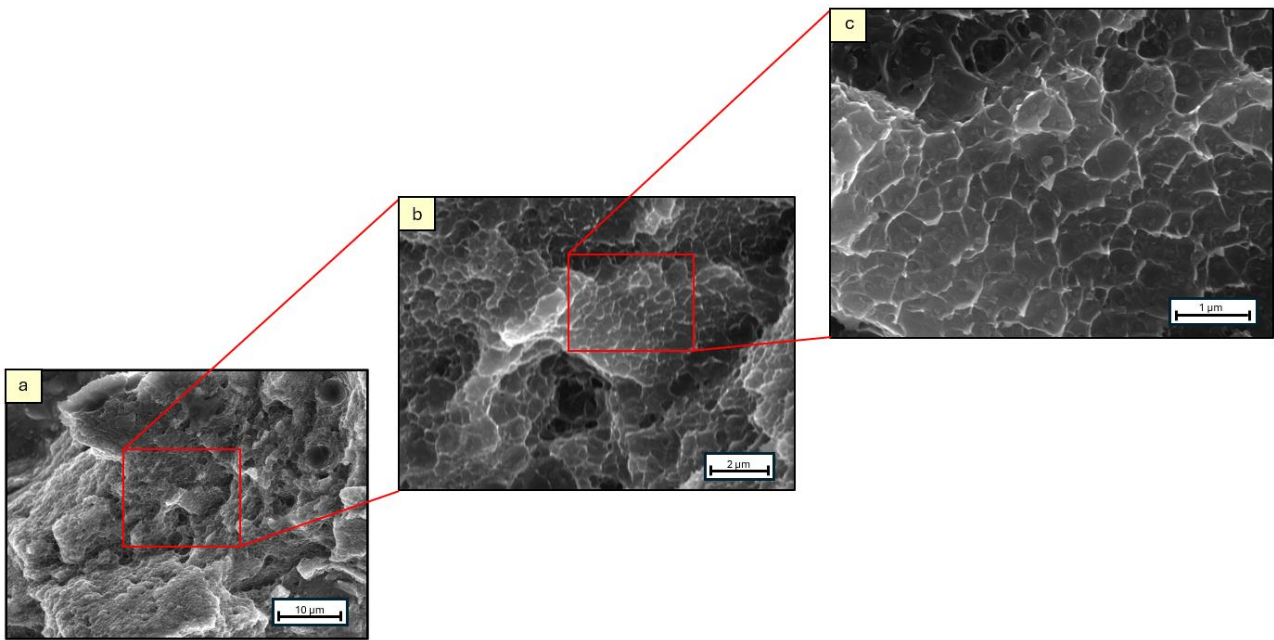
Figure 3.14 – Surface fracture of a) Al_V_SR 5000x b) Al_V_SR 20000x c) Al_V_SR 50000x.

Figure 3.14 shows the surface fracture of the vertical tensile specimen. Comparing the surfaces fracture in *Figure 3.13b* with respect *Figure 3.14a* there are no particular visual differences, this means that the topology surface fracture does not depend on the direction of growth of from the surface condition.

3.1.10   Bracket in cross section

The Bracket has been sectioned, considering the plane passing through the use case in half. In this way it is possible to obtain a vision of the whole internal area and in particular the section of the hall where the beam is attacked by means of the hinge. This was done using OM and stereomicroscope images to check the homogeneity of the internal porosity distribution and the absence of critical porosity near the hole or in other areas. The use case cross section is shown in *Figure 3.15*.
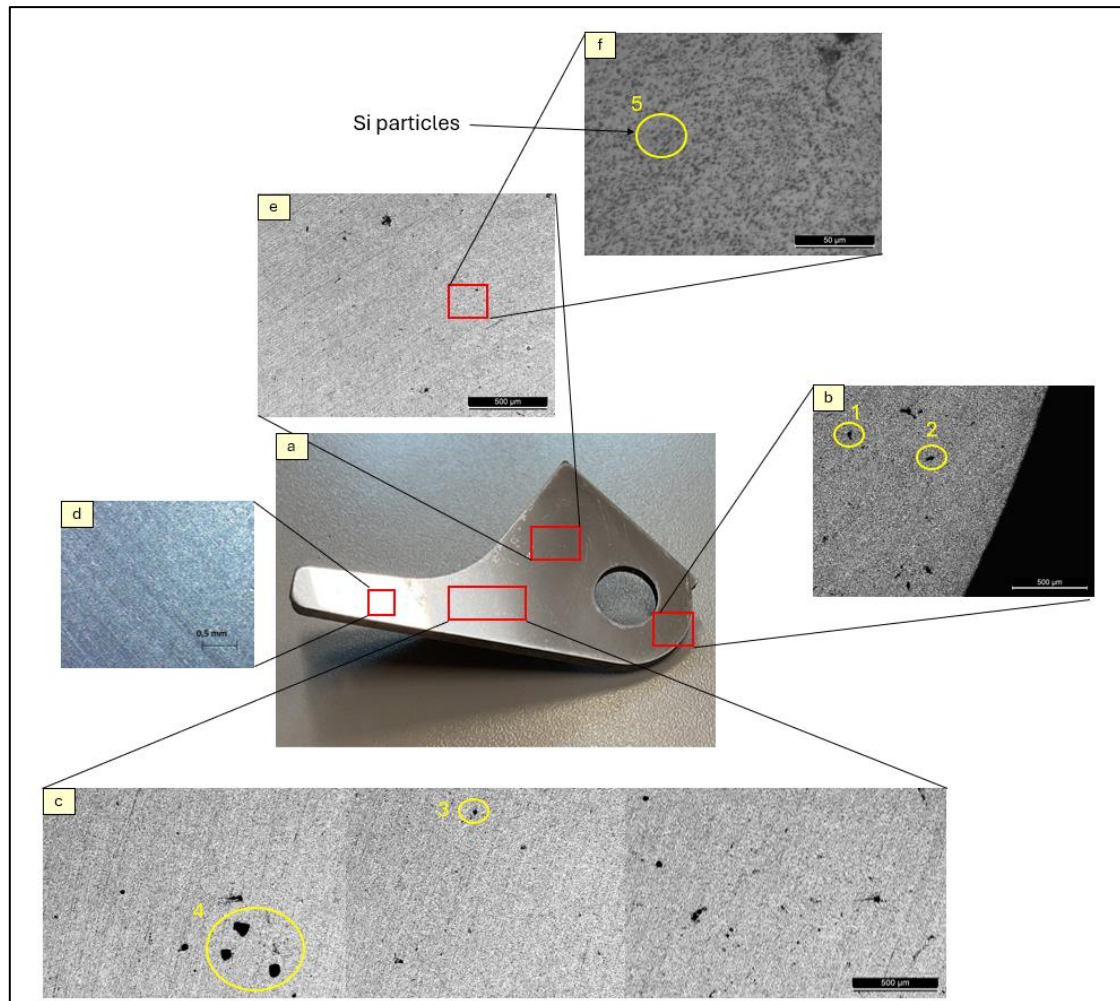
Figure 3.15 – a) Bracket cross section b) OM micrograph of the edge near the hall c) OM micrograph of a side zone d) Stereomicroscope micrograph of a side zone e) OM micrograph of centered zone f) OM micrograph where the presence of Si particles is highlighted.

The images confirm the results shown in *section 3.1.5*: as in the control sample, irregular porosities (1-2) and circular porosities (3-4) can be seen. Furthermore, considering the complex shape of the use case, there are no areas where porosity is particularly concentrated. As discussed in *section 3.1.7*, the HT T6 causes the formation of Si agglomerates of 2-3 µm sizes (5) (*Figure 3.15f*)

3.2 Titanium

3.2.1   Clevis and Connector dimensional inspection

As for the Bracket, the dimensions for the Clevis and the Connector are not shown. In particular in *Table 3.5*, the dimensions that correspond to those on the technical drawing (*Figure 3.16*) and to CAD (*Figure 3.17*) for Clevis and Connector respectively, are marked with a ✓ if they conform or ✗ if they do not.
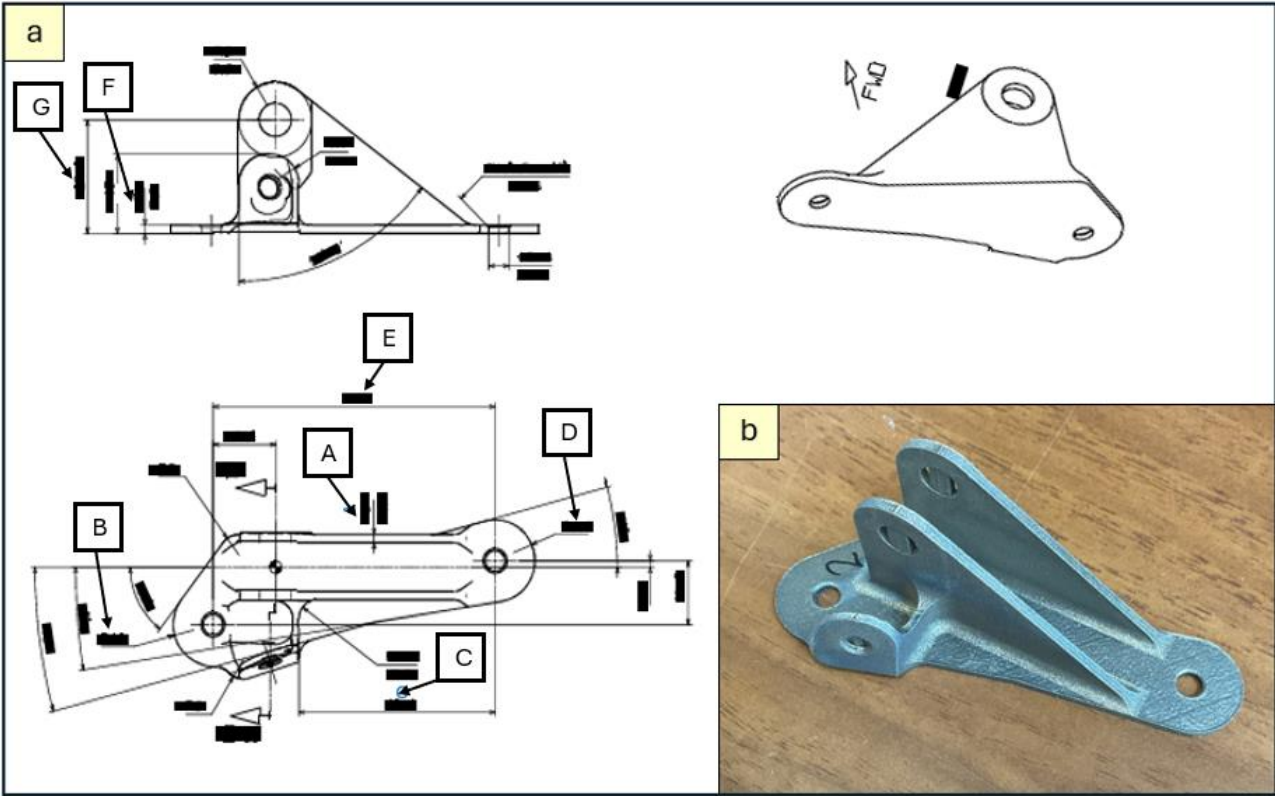
Figure 3.16 – a) Clevis technical drawing (© Leonardo S.p.A.) b) Clevis prospective.
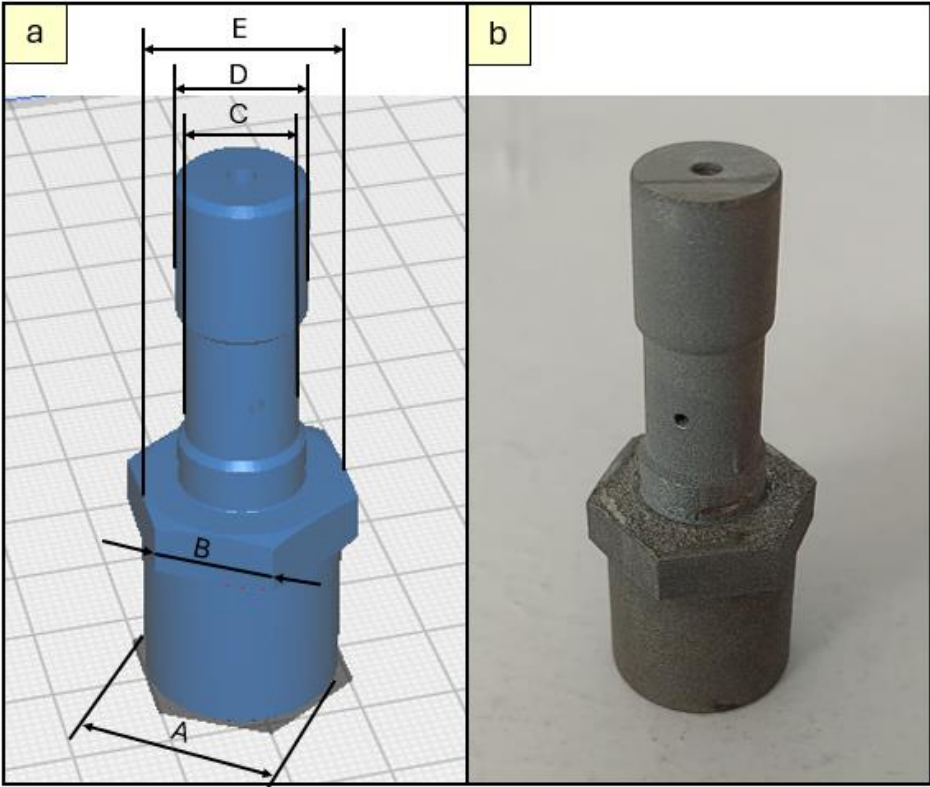
Figure 3.17- a) Connector CAD drawing (© Leonardo S.p.A.). b) Connector prospective.

Table 3.5 – Clevis and Connector dimensional checking.

Clevis dimensions	Compliant	Connector dimensions	Compliant
A	✓	A	✓
B	✓	B	✓
C	✓	C	✓
D	✓	D	✓
E	✓	E	✓
F	✓	-	-
G	✓	-	-

For both applications, all the dimensions checked correspond to those on the technical drawing and the CAD drawing. This is very important because they belong to systems, ECS for the Clevis and LEFAS for the Connector, which have many components that are interlocked with the parts under consideration.

3.2.2   Tensile test
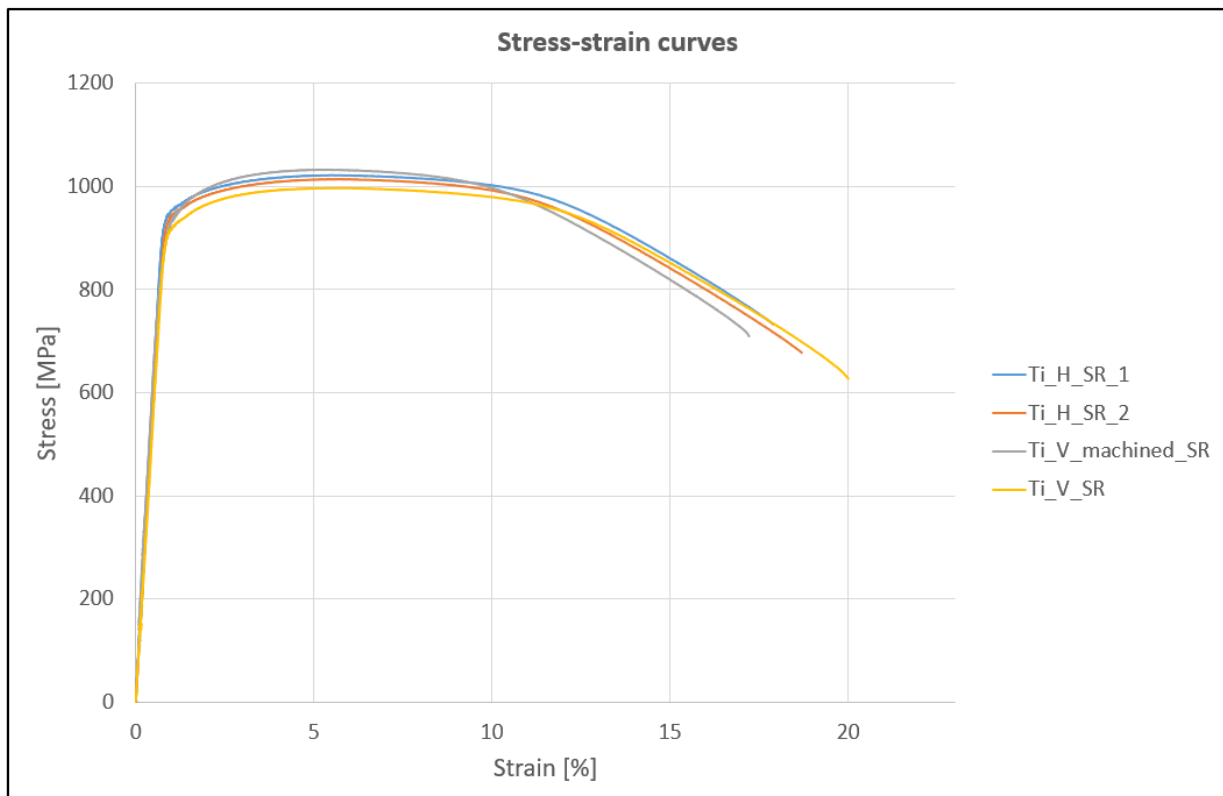
Figure 3.18 – Ti6Al4V stress-strain curves..
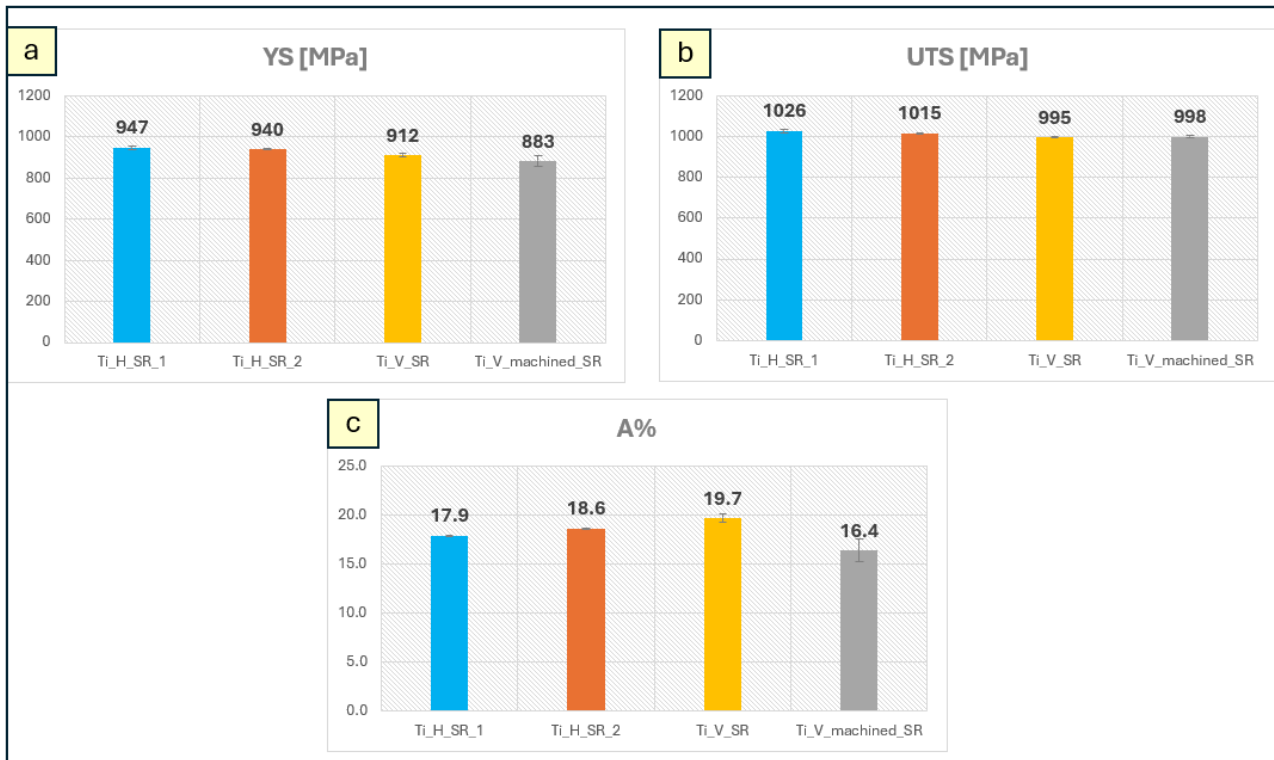
Figure 3.19 – Ti6Al4V (a) YS (b) UTS (c) A% histograms.

In addition to testing the specimens belonging to the 3 types mentioned in *section 2.3.9.1*, a comparison was made between horizontal tensile specimens belonging to 2 different jobs in order to further confirm the reproducibility of the results obtained by the LPBF process.

Figure 3.18 shows the stress-strain curves of tensile specimens. A first analysis of these curves shows that the values of YS and those of UTS are very similar among the 4 typologies of specimens. This is confirmed by the values in the histograms, which show that the difference between the maximum and minimum value is 64 MPa for YS (*Figure 3.19a*), and 30 MPa for UTS (*Figure 3.19b*). Comparing tensile specimens machined or non-machined, the maximum value is achieved by non-machined considering the YS and machined considering the UTS.

The strength values obtained by this thesis work are in linear with those shown for EOS and PoliTO in *section 1.5.9 .*

3.2.3   Hardness test

The HV hardness values are those given in *Table 3.6*.

Table 3.6 – Ti6Al4V hardness.

Test	Hardness [HV]
1	368
2	398
3	380
4	373
Average	379.8 (±13.1)

In general, the hardness of Ti6Al4V alloy is mainly given by the α-HCP phase due to its crystal structure, which has only 3 slip planes with respect to the 48 non-closed packed of a CCC β-phase; this is an obstacle for dislocations movement and consequently an intrinsic increase of hardness.

3.2.4   Roughness test

As said for the aluminum the roughness values are function of the surface orientation due to the strong influence of the overhang angle. *Figure 3.20* compares the roughness along the 3 directions of the cube faces and those of Clevis and Connector.
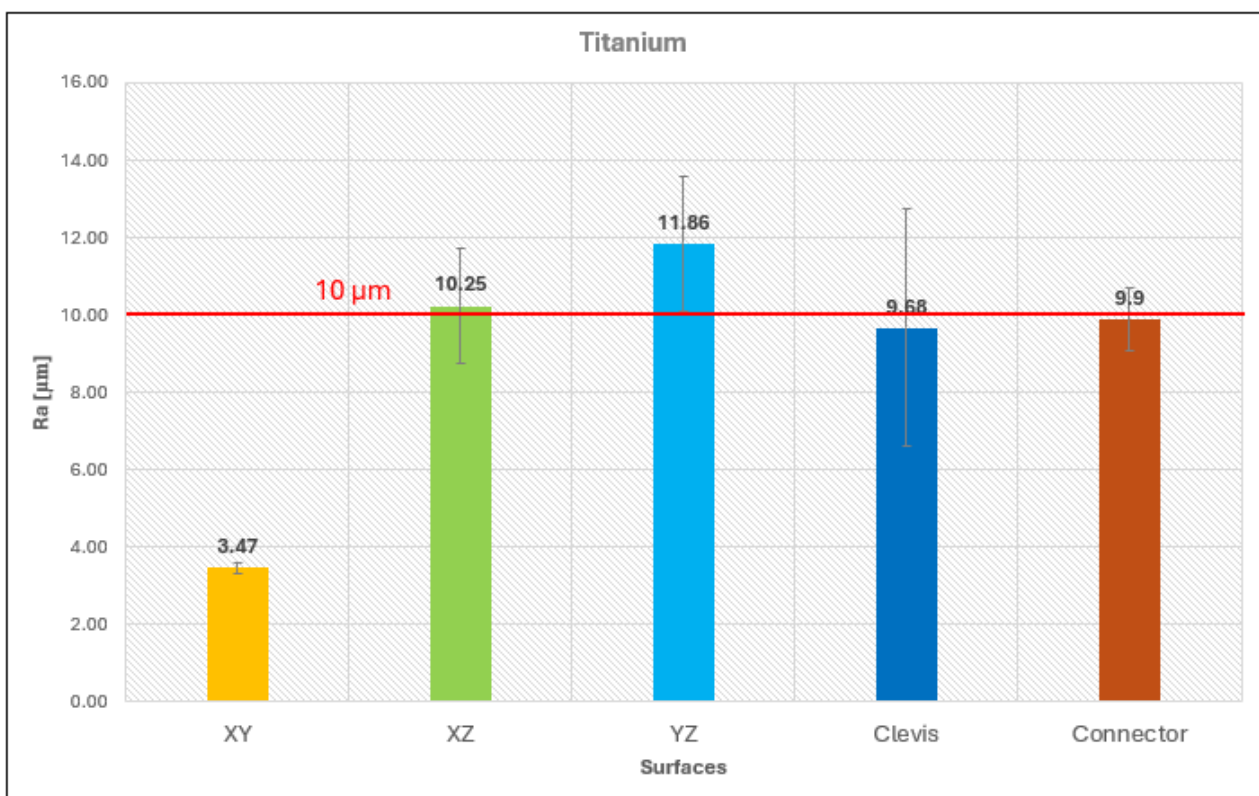
Figure 3.20 – Ra comparison among XY, XZ, YZ plane, Clevis and Bracket surfaces.

As a first analysis, considering the standard deviation, some values of roughness are slightly higher than preferred. However, values for the use cases are to some extent within range of 10 μm suggesting that polishing for titanium material produced by LPBF shall be evaluated case by case. The roughness trend is similar to that of Al, see *Figure 3.4*, with values being the lowest for the XY surface and the highest for the YZ surface. Clevis and Connector have values similar to XZ plane.

3.2.5   Porosity and aspect ratio

As stated in *section 2.3.1*, the buoyancy method is not the most effective method for obtaining accurate measurements of porosity. The OM method allows to obtain better results.

Considering the buoyancy method the data of P% of parallelepiped 3 and cylinder 5 (*Figure 2.21*) are shown in *Table 3.7*.

Table 3.7 – Ti6Al4V porosity percentage by buoyancy method.

	Ti_SR, P%
Parallelepiped 3 (polished)	0.38 (±0.03)
Cylinder 5 (unpolished)	0.66 (±0.09)

As with aluminum, the unpolished sample (cylinder 5) has higher P% values than the polished sample (parallelepiped 3) because the surface roughness can trap gas bubbles and alter measurements.

Figure 3.22 shows micrographs of the porosity of the Ti_SR taken by using OM. Compared to AlSi10Mg, the titanium porosities in this case have a more circular shape (red circles). This is confirmed by the values of aspect ratio shown in *Table 3.8*, which also shows the P% values obtained using ImageJ software. Considering the standard deviation, the XZ values confirm those obtained by the buoyancy method, while for XY the OM analysis shows a lower percentage of porosity.
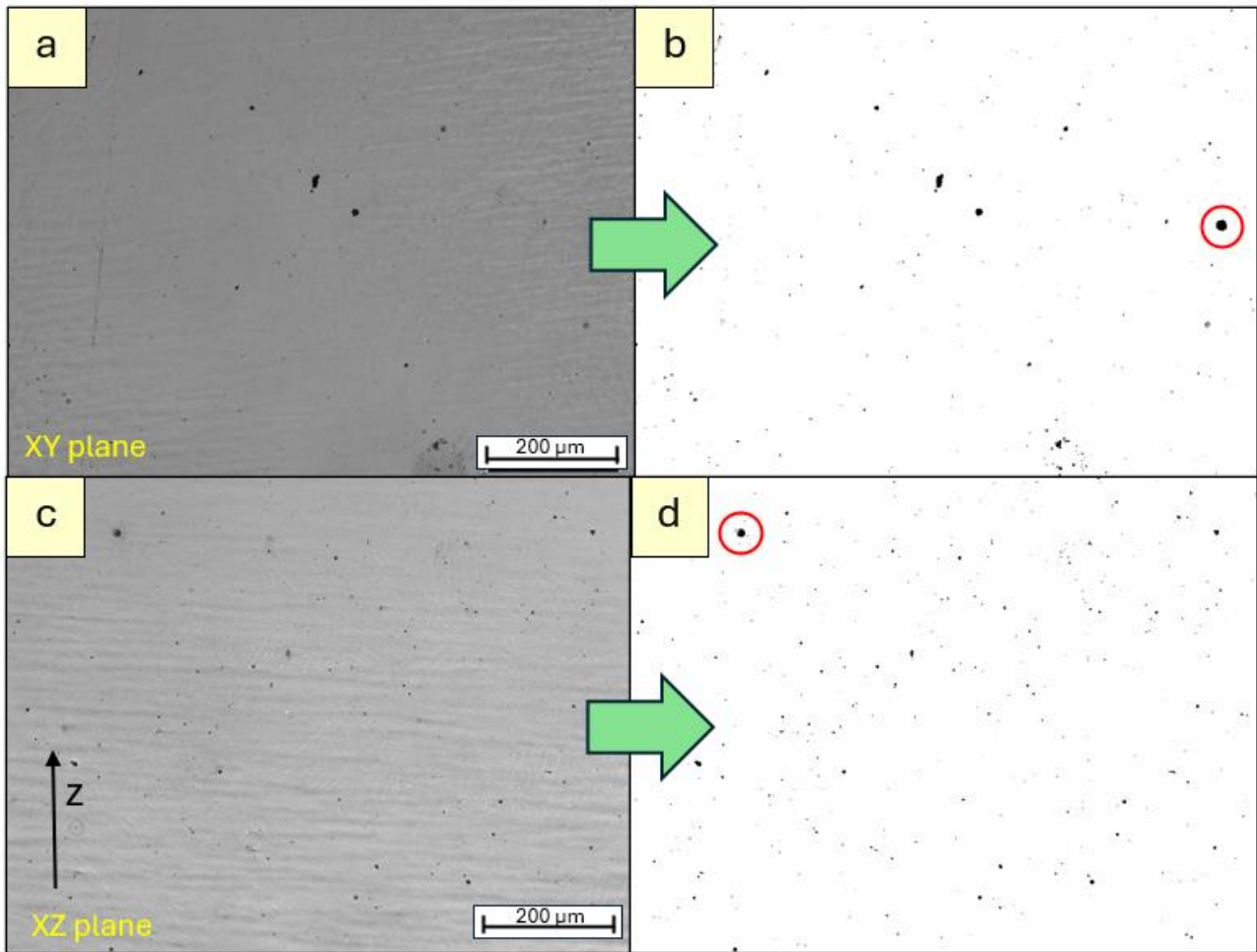
Figure 3.21 – Porosity images on: a) XY plane; b) XY plane after ImageJ elaboration c) XZ plane; d) XZ plane after ImageJ elaboration.

Table 3.8 – Ti6Al4V Porosity and Aspect Ratio by optical microscope.

	P%	Aspect Ratio (l/L)
XY plane	0.17 ($\pm$ 0.06)	0.72 ($\pm$ 0.04)
XZ plane	0.46 ($\pm$ 0.24)	0.69 ($\pm$ 0.04)

These values are in linear with those found by [35].

3.2.6   Phases

As for the aluminum, an XRD analysis of the Ti6Al4V SR alloy has been carried out for the study of the phases of which the alloy is composed. The XRD peaks features are shown in *Figure 3.22*.
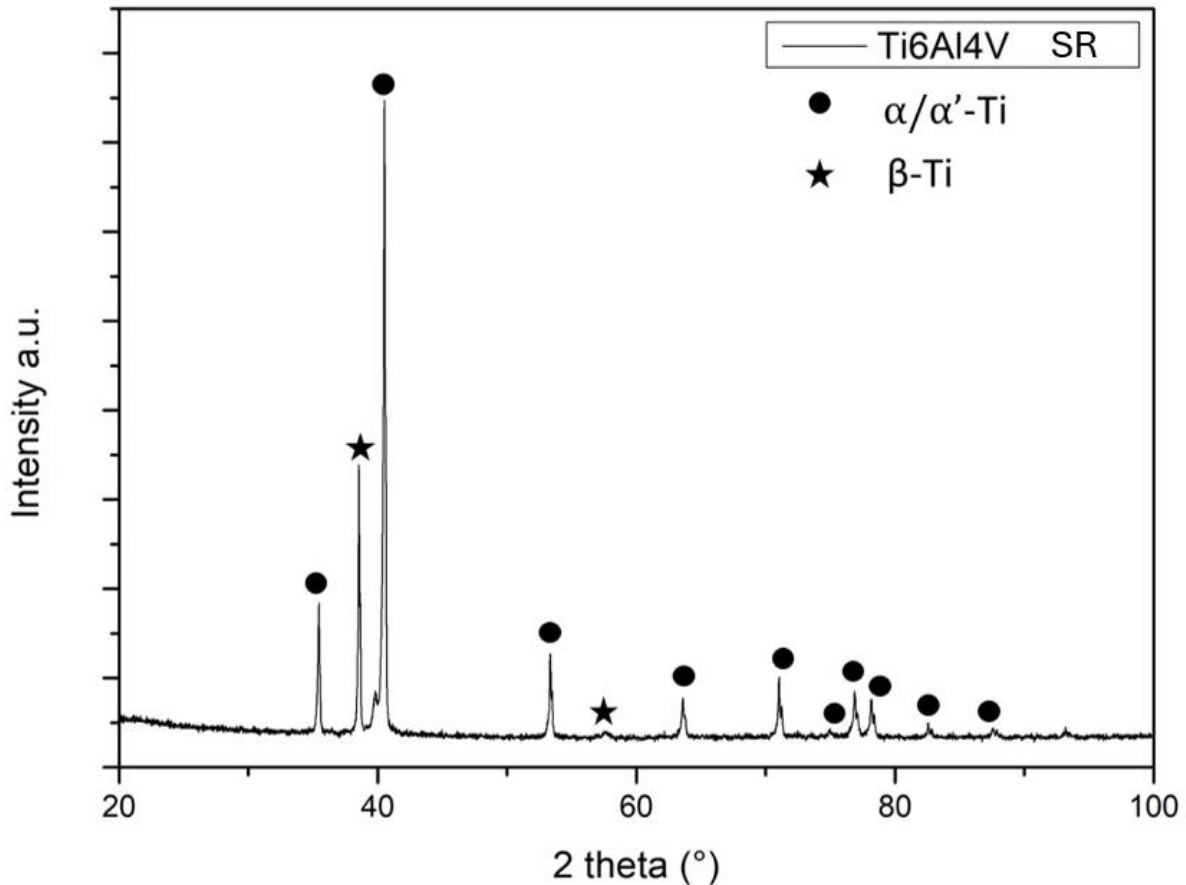
Figure 3.22 – Ti6Al4V XRD peaks spectrum.

In the XRD diagram, the characteristic peaks of α, α' and β are visible. α is the HCP phase Al stabilized, the predominant phase in the alloy, in fact its peaks are the highest; the α' is the residual martensite formed during the cooling phase of LPBF process; β is the BCC phase V stabilized and present in a lower percentage, in fact the peaks are shorter. The presence of these phases is confirmed by microstructure (*section 3.2.7*) and chemical composition analysis (*section 3.2.8*).

3.2.7   Microstructure analysis

As for the aluminum, the microstructure analysis has been done using *Stereomicroscope*, *OM* and *SEM-SED* instruments (*Figure 3.23*). The main characteristics studied are the difference in microstructure in XY and XZ planes.
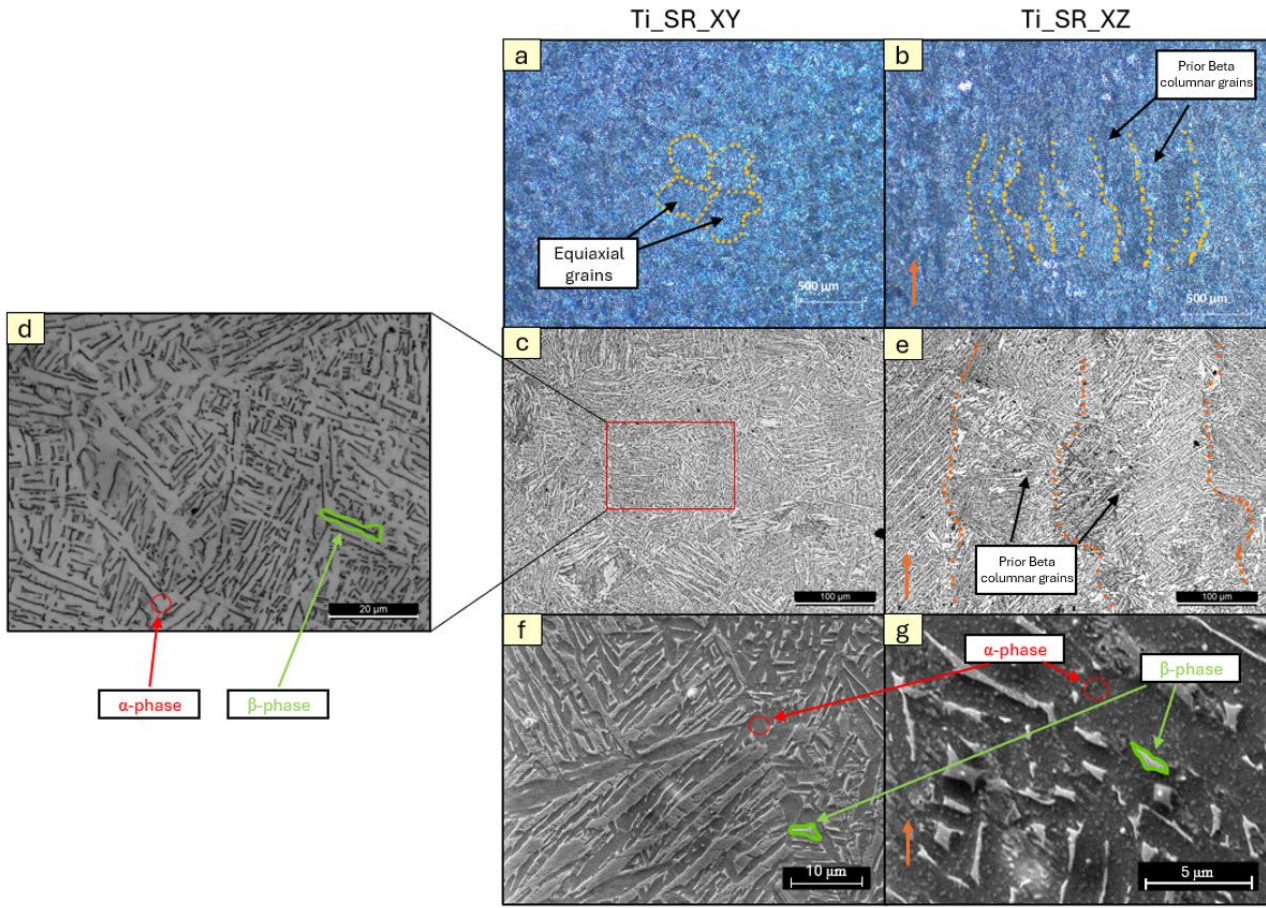
Figure 3.23 – Ti6Al4V microstructure: a) XY-plane at stereomicroscope b) XZ-plane at OM c) XY-plane at OM d) Magnification of XY-plane at OM e) XZ-plane at OM f) XY-plane at SEM-SED g) XZ-plane at SEM-SED.

Stereomicroscope images show equiaxial grains along the XY plane (a) and columnar grains along the XZ plane (b). Along the growth direction, the grains have a thickness of about 150 μm. In the OM image, α (light) and β (dark) phases are highlighted in red and green, respectively (d). A magnified view of the β-phase within the α-phase is shown in the SEM-SED images (f-g).

3.2.8   Chemical composition

An EDS mapping analysis was performed to evaluate the alloying element distribution. A linear EDS analysis was also carried out to clearly see the Ti, Al, V distribution.
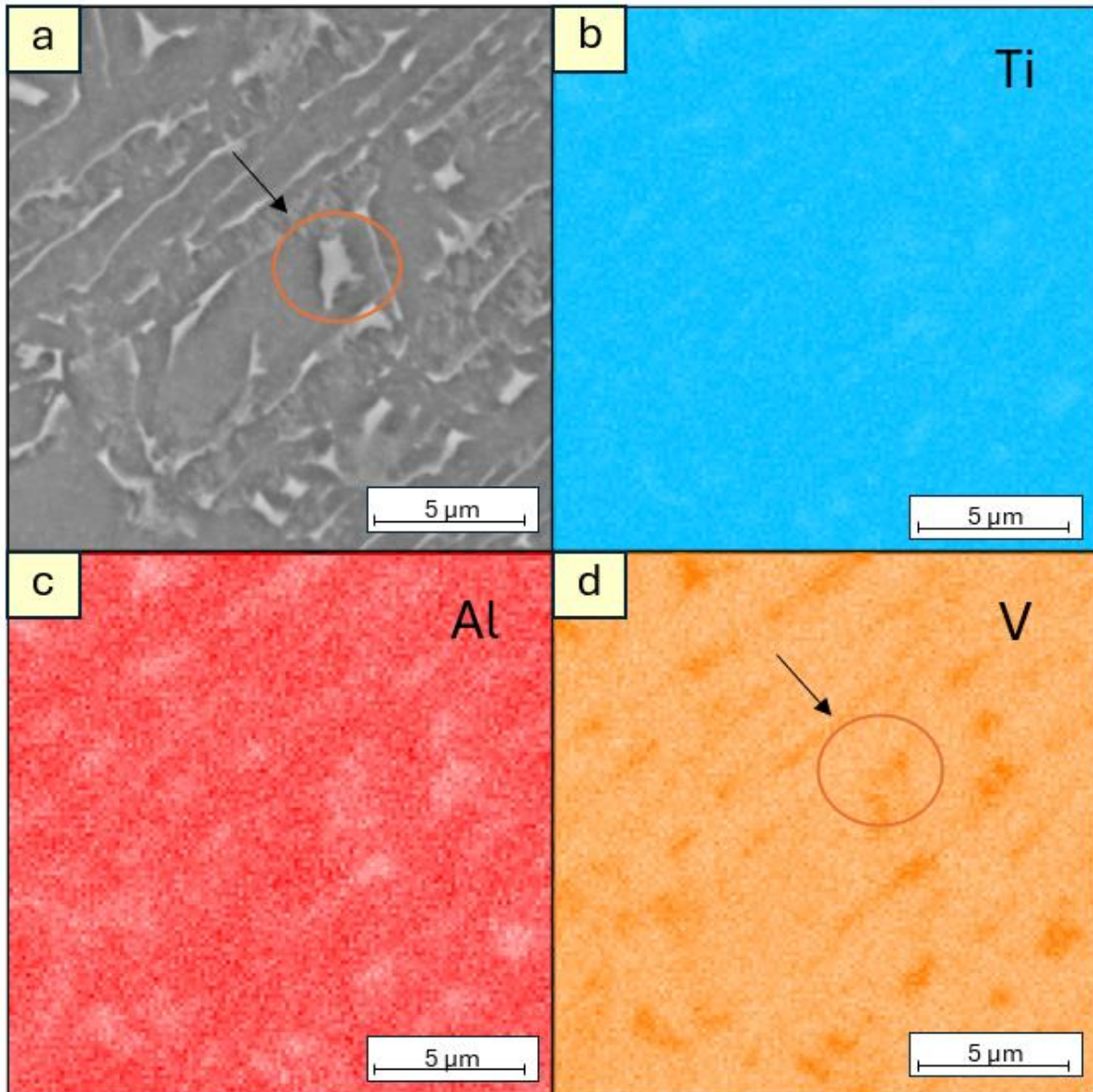
Figure 3.24 – EDS map of Ti_SR: (a) area considered (b) Ti map (c) Al map (d) V map.

Figure 3.24 shows the distribution of alloying elements in the sample. At this magnification, there is a global homogeneous distribution of Ti, Al and V throughout the sample. Considering (d), the zones where the color is more pronounced are the region where there is a higher presence of V. A specific area was selected (orange circle) to perform a linear EDS analysis.
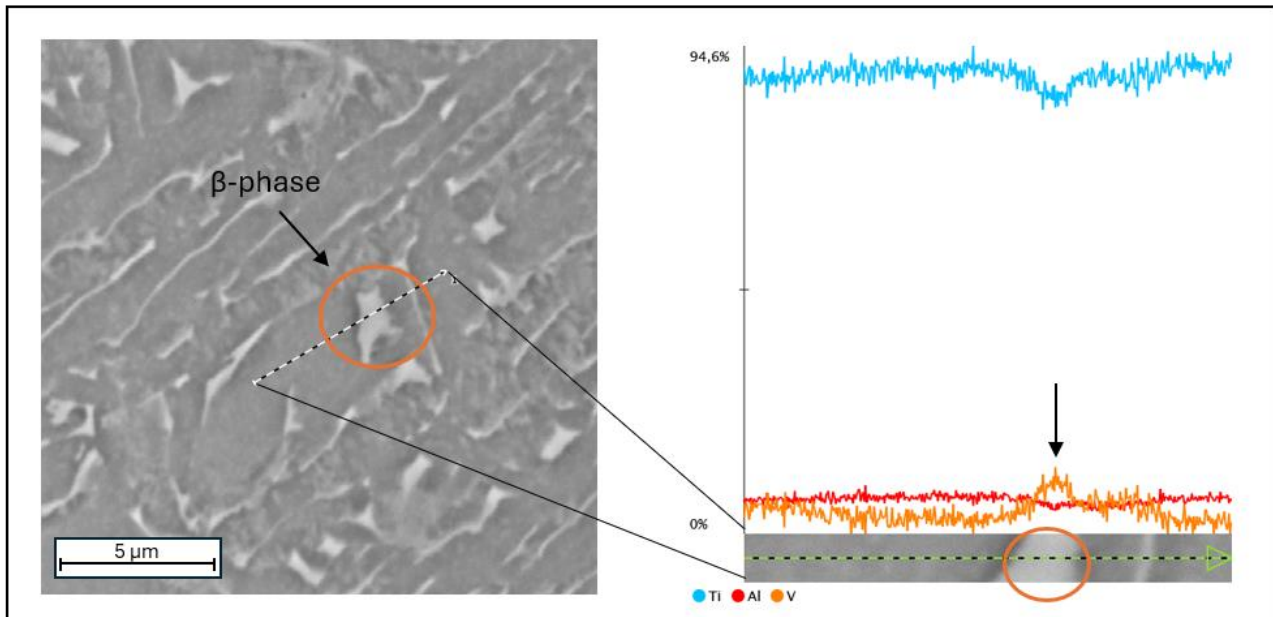
Figure 3.25 – EDS linear analysis: V intensity peak corresponding to β-phase (orange circle).

An EDS linear image analysis (*Figure 3.25*) was performed considering the same area circled in the EDS mapping analysis. Corresponding to the lighter area (orange circle) there is the presence of a V peak in the intensity chemical composition diagrams, confirming the result obtained by EDS mapping. V is a β-stabilizer, so this is a β-phase surrounded by α-phases.

3.2.9   Fracture surface analysis
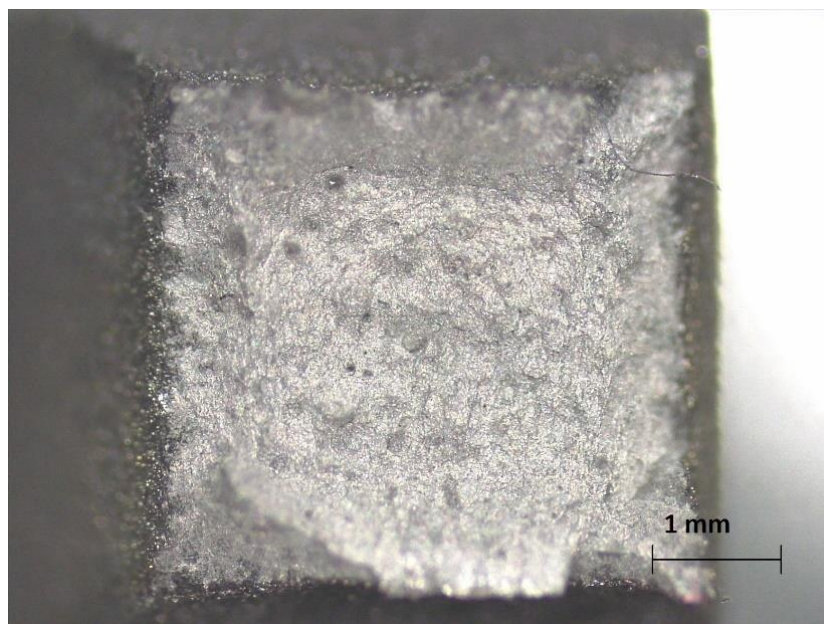
Figure 3.26 – Fracture surface of Ti6Al4V tensile specimen by stereomicroscope.

Titanium, as for the Aluminum, is subjected to plastic deformation and consequently to a ductile fracture. *Figure 3.27* and *Figure 3.28* show the fracture surfaces of Ti_H_SR and Ti_V_machined_SR respectively.
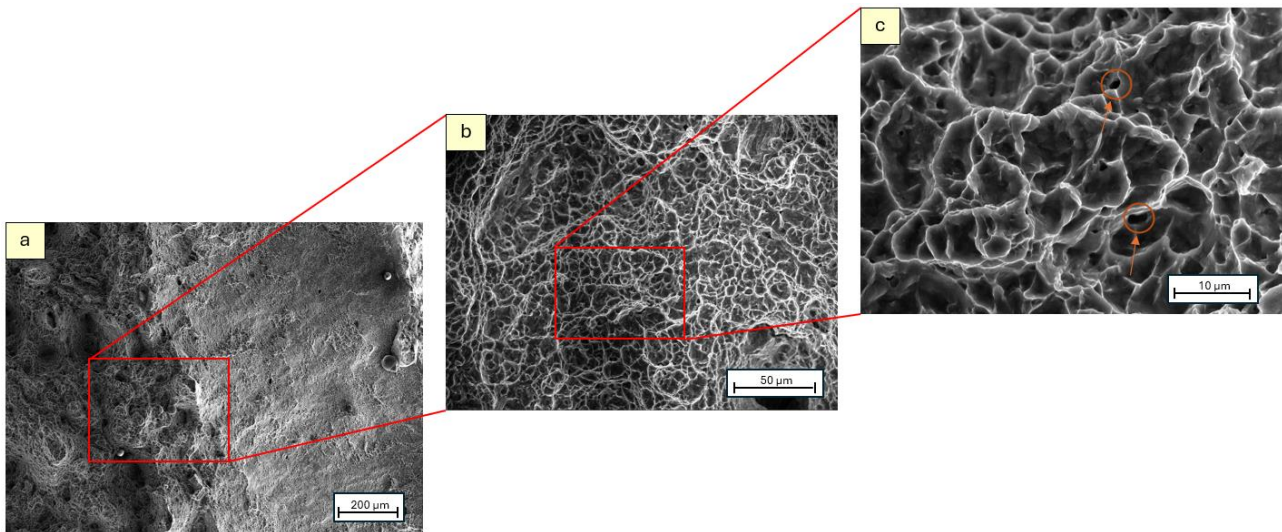
Figure 3.27 – Fracture surface of Ti_H_SR at a) 200x b) 1200x c) 5000x magnifications.
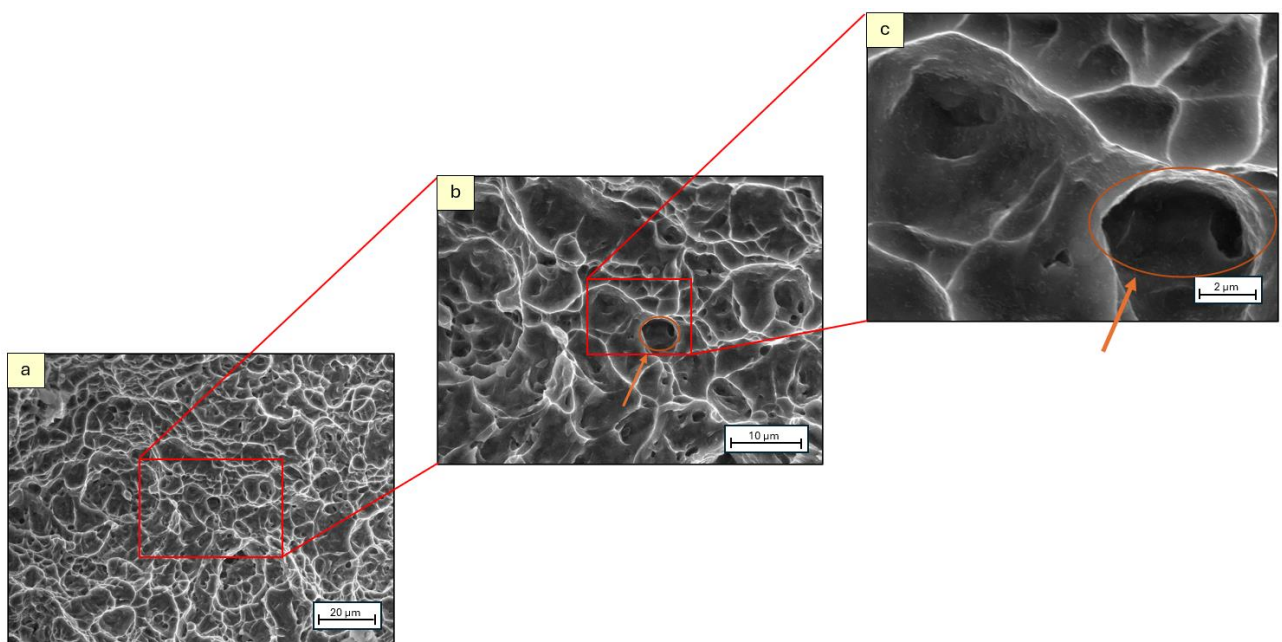
Figure 3.28 – Fracture surface of Ti_V_machined_SR at (a) 2000x (b) 5000x (c) 20000x magnifications.

For both Ti_H_SR and Ti_V_machined_SR tensile specimens, the fracture is ductile, it can be seen by the presence of dimples. There are no particular differences with Ti_H_SR and Ti_V_machined_SR, which means that the typology or fracture does not depend on the direction of growth or from the surface conditions. In both figures, a specific area is magnified to highlight the formation of microcavities (orange circles), which have a dimension of approximately 4 µm.

3.2.10   LECO analysis

The result of the analysis is reported in the *Table 3.9*.

Table 3.9 – Chemical interstitial elements % after EDM machining process.

Samples	Oxygen (O) [wt%]	Nitrogen (N) [wt%]	Hydrogen (H) [ppm]
A*	0.0611	0.00249	34.9 (0.00349 wt%)
B*	0.0125	0.000447	29.2 (0.00292 wt%)

*For samples configuration see *Figure 2.34*

As expected, Sample A, which is taken at the point of contact with the EDM cutting surface, has a higher percentage of H, N, H than Sample B. Comparing the sample A, which has the highest values of interstitial elements, with (chemical requirements) of Standard specification of Ti6Al4V wrought alloys [36] we have:

- 0.0061 < 0.13 (O)
- 0.00249 < 0.05 (N)
- 0.00349 < 0.012 (H)

The percentage of interstitial elements in the control sample is below the maximum levels required by the specification, so the EDM is not considered to be hazardous to the maintenance of mechanical properties.

3.2.11   Connector in cross section

The Connector has been cut in half, taking into account the central symmetry of the use case.
In this way it is possible to observe the channel where the oil is pumped through the LEFAS system accumulator. Taking OM and stereomicroscope images, it is possible to check the internal microstructure and porosity. These aspects are crucial in determining the mechanical properties of the connector, which must be able to withstand the high pressures reached by the oil, up to 200 bar.
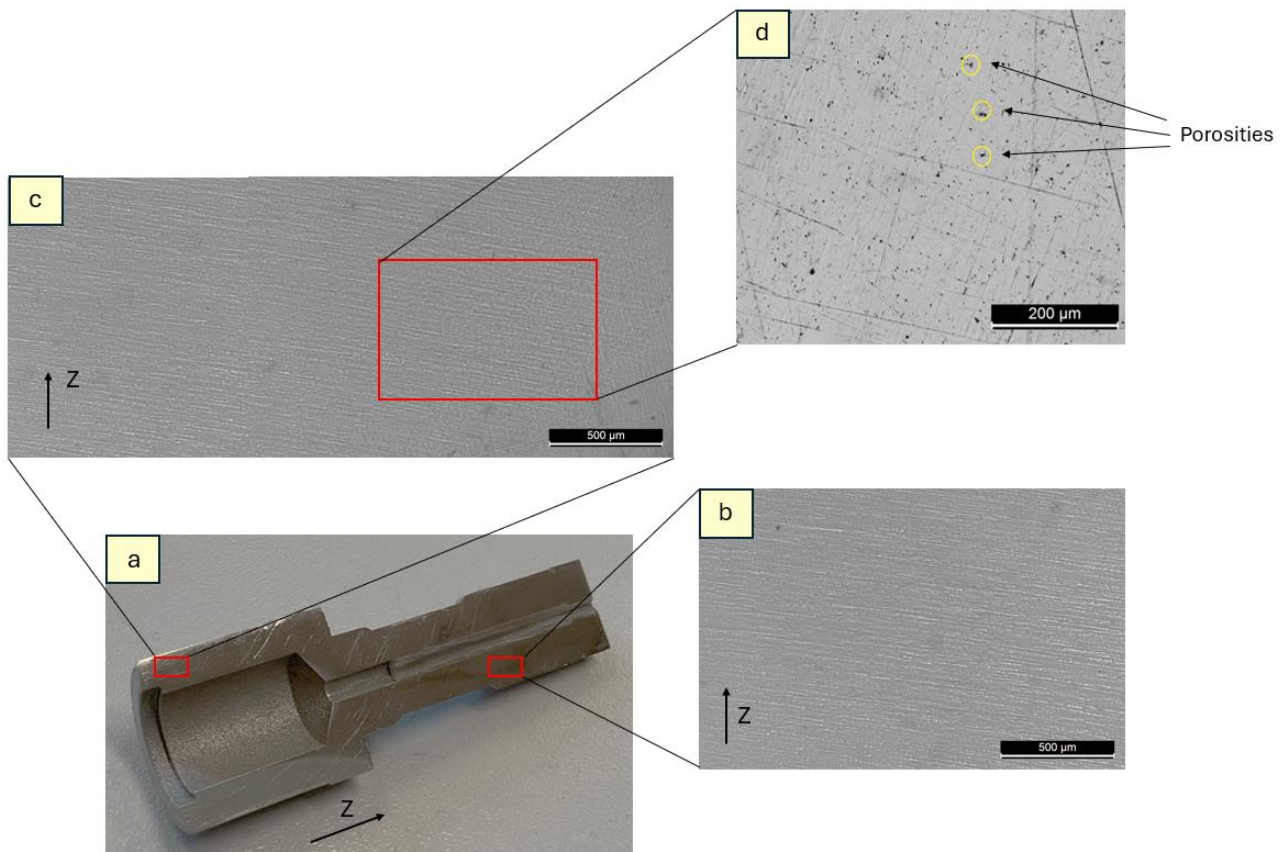
Figure 3.29 – a) Connector cross section b) OM micrograph of upper-right area c) OM micrograph of the lower left area d) OM micrograph magnification (porosities).

The images in *Figure 3.29* (*b-c*) clearly show the growth layer resulting from the LPBF process (orthogonal to the z-direction). Image d) is a magnification to highlight the porosities, which are quite homogeneously distributed on the surface considered. This means that there are no areas of concentrated porosity, which is a weak point in the component. The porosities have a fairly spherical shape which confirms the results obtained in *section 3.2.5*.

Chapter 4
POST-PROCESSING TREATMENTS

4. POST-PROCESSING TREATMENTS

As-built use cases have porosity and other defects, such as residual stresses, that can be detrimental in some applications. For this reason, the main objective of post-processing treatments is to remove these undesirable properties in order to improve the mechanical properties of the final components. In this section some suggestions have been made for both the AlSi10Mg and Ti6Al4V.

4.1 AlSi10Mg Heat Treatments

As already shown in *sections 2.2.3* and *2.2.6*, post-processing HTs consist in bringing the alloy to a predetermined temperature, holding it for a certain time and then cooling it to room temperature. *Table 4.1* lists the 4 main heat-treatments which are usually done on the AlSi10Mg as-built alloy LPBF-manufactured and the temperatures reached, as shown by [37].

Table 4.1- Post-processing HT and specific thermal cycle.

Post-processing HT	Thermal cycle*
(1) Stress Relieving (SR)	Temperature: 300°C, Time: 2 h
(2) T6	1. HT Temperature: 500°C, time: 0.5-4 h 2. Aging Temperature: 180°C, time: 6 h
(3) Hot Isostatic Pressing (HIP)	Temperature: 500°C, time: 2 h; P = 100MPa
(4) T5	Temperature: 200°C, time: 2 h

* The temperature and time values here are specific, but fall within a range that is commonly used:
- SR: temperature: 300°C; time: 1 - 4 h;
- HT: temperature: $\geq$ 500°C; time: 30 min - 4 h;
- Ageing: temperature: 160 - 190 °C.

Table 4.2 shows how the mechanical properties of *YS*, *UTS*, *A%*, *Hardness* and *Fatigue Strength* are affected by different HTs. Mechanical properties that are improved, with respect to the as-built state, by the specific HT are indicated by an '↑', while those that are reduced are indicated by an '↓'.

Table 4.2 – Effect of HTs on the main AlSi10Mg mechanical properties.

Post-processing HT	UTS	YS	A%	Hardness	Fatigue Strength
SR	↓	↓	↑	↓	↑
T6	↓	↓	↑	↓	↑
HIP	↓	↓	↑	↓	↑
T5	↑	↑	↓	↑	↑

As shown in *Table 4.2* fatigue strength appears to improve after each HT. The increase in fatigue is particularly evident in the case of HIP where it is due to the sealing of pores generated during the building process. HIP can be therefore recommended for components that are particularly subject to cyclical loads and need to improve their life cycle. The main drawback is the reduction of UTS and YS properties, so the ability to withstand high loads. On the contrary, the T5 HT, also called direct aging, shows a counter trend. This HT can be taken into account if you want to achieve the improvement of UTS, YS and fatigue strength simultaneously. However, this results in a reduction in ductility.

In addition, HTs can be applied one after the other, for example SR to reduce the residual stress inside the component when it is still on the building platform, HIP to close porosities and finally T6 to improve the properties with respect to the part only SR. For more details consult [37].

4.2 Ti6Al4V Heat Treatments

Table 4.3 lists the 4 main heat-treatments which are usually done on the Ti6Al4V as-built alloy LPBF-manufactured and the temperatures reached, as shown by [38].

Table 4.3 – Post-processing HT and temperatures reached.

Post-processing HT	Temperature (T)
Stress Relieving (SR)	$400 < T_{SR} < 800$ °C
Annealing (ANN)	$700 < T_{ANN} < 940$ °C
Solution Heat Treatment (SHT) + Artificial Ageing (AA)	$940 < T_{SHT} < 970$ °C or $T_{SHT} > \beta\text{-transus*}$ & $T_{AA} \leq 700$ °C
Hot Isostatic Pressing (HIP)	$900 < T < 1050$ °C

*β-transus = 995 °C

Table 4.4 shows how the mechanical properties of *YS*, *UTS*, *A%*, are in As-Built (AB) condition and after the HTs.

Table 4.4 – Mechanical properties after HTs for Ti6Al4V.

HT condition	YS [MPa]	UTS [MPa]	A%
AB	1110 ± 9	1267 ± 5	7.3 ± 11
SR	1118 ± 39	1223 ± 52	5.4 ± 2
ANN	1026 ± 35	1082 ± 34	9.1 ± 2
SHT + AA	899 ± 27	948 ± 27	13.6 ± 0.3
HIP	-	1086 ± 26	13.8 ± 1.3

As shown in the table above, the mechanical properties of AB-Ti6Al4V show high value in terms of YS and UTS due to the fully α' martensitic microstructure. The high strengths correspond to low A% (<10%) so that the HTs provide a good balance between tensile strength and ductility. In particular the SR allows to obtain the highest values of strengths but not so high ductility value which, on the contrary are reached by SHT+AA and HIP HTs. For more details consult [38].

Chapter 5
ALTERNATIVE ALLOYS FOR ALSI10MG

5. ALTERNATIVE ALLOYS FOR ALSI10MG

Considering AlSi10Mg LPBF manufactured in this thesis work, see *section 3.1.2*, and considering the previous research about this alloys, see *section 1.5.9*, does not meet the Leonardo's internal specification, it has been concluded that AlSi10Mg does not guarantee the same mechanical properties of the Al2024-T3.

Therefore, some alternative alloys, that offer better properties, are proposed:

- **A20X**: derives from the aerospace A205 castable aluminum alloy. It comprises 4 wt% of Cu and 3 vol% of TiB_2 particles as grain refiner to avoid the solidification cracking. Applications are widely varied between prototypes, aerospace functional parts and small runs of its A205 cast equivalent. The mechanical properties refer to the alloy subjected to a T7 heat treatment [39] .

- **Al 2139**: is part of the 2000 series of aluminum alloys which are primarily alloyed with copper. It is subjected to hot tearing but the addition of AlTiB particles grain refiners shows a clear effect in reduction this phenomenon [40]. This allows to obtain an alloy with good buildability, productivity and excellent mechanical properties after a T4 heat treatment [41].

- **Scalmalloy**: is a powder product designed specifically for LPBF process. Due to high cooling rates and rapid solidification, a unique microstructure is achieved. The material properties with the design freedom provided by AM processes can enable high performance parts with a high level of functionality. The mechanical properties refer to the alloy heat treated [42].

- **AlSi9Cu3:** is commonly prepared by high-pressure die casting. It may benefit from the refined microstructure commonly induced by LPBF techniques.
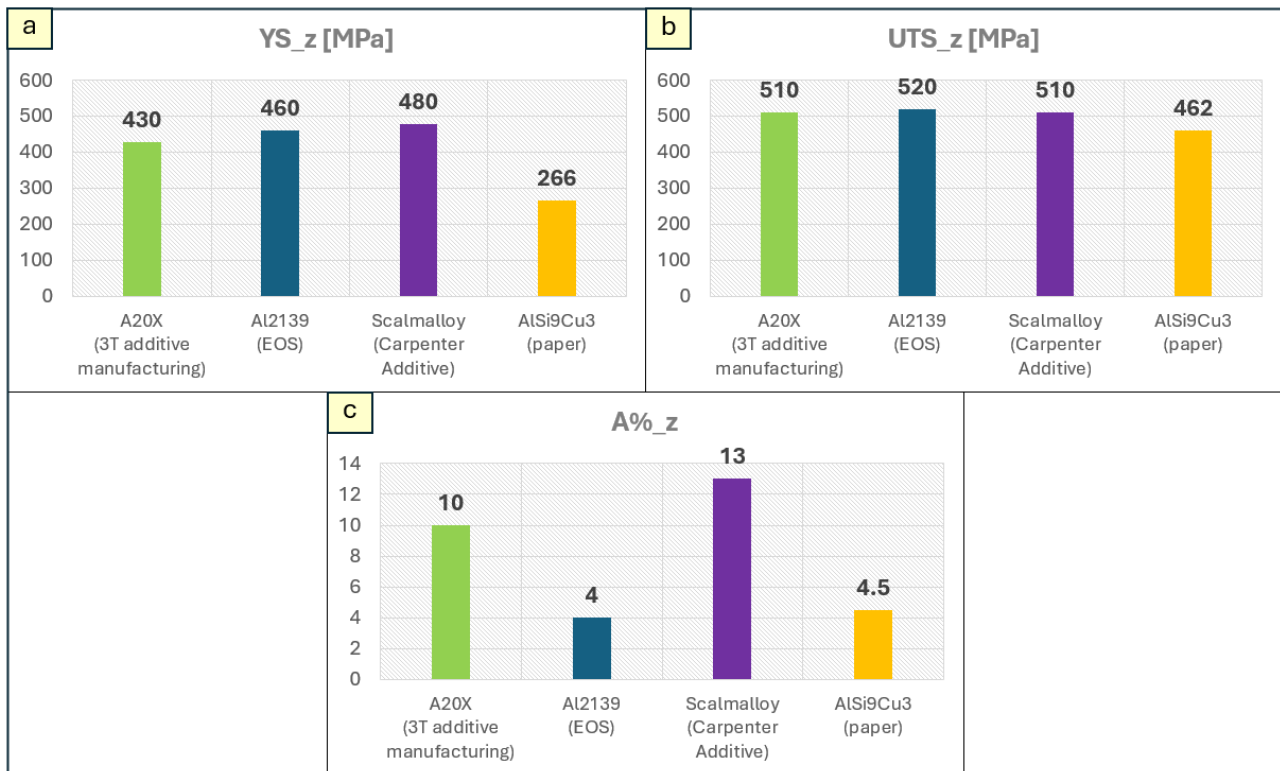
Figure 5.1 – a) YS_z b) UTS_z c) A%_z of the alternative alloys for AlSi10Mg.

The histograms shown in *Figure 5.1* illustrate that Scalmalloy is the alloy that offers the best combination of YS (480 MPa), UTS (510 MPa) and A% (13%), for this reason it can be the most interesting if there is an intention to produce a new internal company specification. Al20X and Al2139 are fascinating because they offer a very similar YS to Scalmalloy and the same UTS values. The A% is lower than Scalmalloy. The AlSi9Cu3, among the others, is the one that offers the lowest values of strength, so it is the least to be considered in case of replacement. Finally, all alloys presented in this section have higher strength and ductility comparable to AlSi10Mg, see *section 3.1.2*.

6. CONCLUSIONS

This master's thesis has focused on confirming that AM processes can be effectively exploited from a logistic support point of view to produce components with the required properties. In particular, it has been produced metallic parts, considered as 'perfect candidates', from several of Leonardo's aircraft platforms after assessing the feasibility from a manufacturing standpoint and suitability from a logistic standpoint. The feasibility of the LPBF process has been evaluated together with the properties of the components, in AlSi10Mg and Ti6Al4V, obtained by this technology. For this reason, jobs with components, control and tensile samples, have been manufactured.

Initially, a stress-relieving heat treatment has been performed on the jobs to remove the residual stresses resulting from the manufacturing process.

Afterwards, EDM machining has been useful to remove all the parts from the building platform.

A first dimensional inspection has been carried out on the components. The Bracket dimensions were in accordance with the technical drawing, except for one that has been intentionally made in accordance with the CAD model. The dimensions of the Clevis and Connector were consistent with their technical drawing and CAD model, respectively. Therefore, the LPBF process must be considered reliable for building components with the required engineering dimensions.

Eventually, some of the tensile specimens and control samples of AlSi10Mg have been subjected to a T6 heat treatment, as suggested in the EOS datasheet, to improve the mechanical properties.

The porosity percentage, which is a critical factor that significantly impacts the mechanical properties of the component, has been calculated and it is linear with the values found in literature.

The tensile and control samples for both materials have been tested to evaluate the key mechanical properties such as the YS, UTS, A% and hardness. The results found for Bracket, built in AlSi10Mg due to the fact the Al2024 conventional material is not adapted to LPBF process, have shown that heat treatment is advised to improve the strength. The values for the heat-treated samples, have been in linear with those of EOS datasheet and literature (YS > 250 MPa, UTS > 315 MPa, A% ~ 10). The hardness test proves higher values for heat treated samples, confirming the effectiveness of T6 heat treatment. The values for Clevis and Connector, built in Ti6Al4V alloy, are perfectly aligned with those of EOS and literature (YS ~ 940 MPa, UTS > 1000 MPa, A% > 13). Moreover, the Ti6Al4V LPBF manufactured has higher mechanical properties than Ti6Al4V obtained with traditional methods, this is a promising incentive to use LPBF technology to produce parts for aircraft platforms. Roughness for the Bracket was a little higher than 10 μm, so it is recommended to polish the surface if is requested; on the contrary the Clevis and Connector shows values of about 10 μm, this suggest

that polishing for titanium material produced by LPBF shall be evaluated case by case.

An in-depth inspection of the microstructure and chemical composition of the alloys be concerned about has been made by means stereomicroscope, optic microscope, SEM and FESEM. In particular, it has been possible to recognize and highlight the strengthening and failure mechanisms of AlSi10Mg and Ti6Al4V.

Furthermore, a cost estimation has been made, taking into account the full production and trying to optimize the AM production.

Post processing heat treatments for both as-built alloys are suggested and some alternative LPBF Al alloys are proposed which offer better properties than AlSi10Mg, in case technical specifications properties are required.

Eventually, in view of the thorough analysis and the carefully and deeply argued results, it can be confirmed that Additive Manufacturing could be integrated in the supply chain of spare parts with great benefits.

References

(1) BEAMIT Website. https://www.beam-it.eu/it/.

(2) ATA CODE. https://itlims-zsis.meil.pw.edu.pl/pomoce/ESL/2016/ATA_Chapters.pdf.

(3) Leonardo Velivoli. https://aircraft.leonardo.com/it/?gad_source=1&gclid=Cj0KCQiAlsy5BhDeARIsABRc6ZvJC MIHAK-uhzjMhWpMykYbnDHOLseepgkbYPSWc4R_SF2hDMDNyigaApAwEALw_wcB.

(4) Greco, Consiglia. Roadmap for Additive Manufacturing of Spares in Aerospace, Politecnico di Torino.

(5) Bikas, H.; Stavropoulos, P.; Chryssolouris, G. Additive Manufacturing Methods and Modelling Approaches: A Critical Review. *Int J Adv Manuf Technol* **2016**, *83* (1–4), 389–405. https://doi.org/10.1007/s00170-015-7576-2.

(6) AM Technologies Overview. https://ecrimesagroup.com/the-characteristics-of-additive-manufacturing-and-how-to-use-it-in-the-fabrication-of-metal-pieces/.

(7) Chowdhury, S.; Yadaiah, N.; Prakash, C.; Ramakrishna, S.; Dixit, S.; Gupta, L. R.; Buddhi, D. Laser Powder Bed Fusion: A State-of-the-Art Review of the Technology, Materials, Properties & Defects, and Numerical Modelling. *Journal of Materials Research and Technology* **2022**, *20*, 2109–2172. https://doi.org/10.1016/j.jmrt.2022.07.121.

(8) Terner, M.; Ricordel, T.; Cho, J.-H.; Lee, J.-S. The Response Surface Methodology for Optimizing the Process Parameters of Selective Laser Melting. *Journal of Welding and Joining* **2019**, *37* (1), 27–39. https://doi.org/10.5781/JWJ.2019.37.1.4.

(9) Buffa, G.; Costa, A.; Palmeri, D.; Pollara, G.; Fratini, L. Defining a New Process Window for LPBF of Ti-6Al-4V Based on Micro-Warping Phenomena. *CIRP Journal of Manufacturing Science and Technology* **2024**, *52*, 1–11. https://doi.org/10.1016/j.cirpj.2024.05.012.

(10) Buhairi, M. A.; Foudzi, F. M.; Jamhari, F. I.; Sulong, A. B.; Radzuan, N. A. M.; Muhamad, N.; Mohamed, I. F.; Azman, A. H.; Harun, W. S. W.; Al-Furjan, M. S. H. Review on Volumetric Energy Density: Influence on Morphology and Mechanical Properties of Ti6Al4V Manufactured via Laser Powder Bed Fusion. *Prog Addit Manuf* **2023**, *8* (2), 265–283. https://doi.org/10.1007/s40964-022-00328-0.

(11) LPBF Building Chamber Layout. https://www.intechopen.com/chapters/83547.

(12) Mouritz, Adrian. Introduction to Aerospace Materials.

(13) Aluminum Alloys Series. https://taberextrusions.com/tag/6xxx-series-aluminum-alloys/.

(14) Giovagnoli, M.; Silvi, G.; Merlin, M.; Di Giovanni, M. T. Optimisation of Process Parameters for an Additively Manufactured AlSi10Mg Alloy: Limitations of the Energy Density-Based Approach on Porosity and Mechanical Properties Estimation. *Materials Science and Engineering: A* **2021**, *802*, 140613. https://doi.org/10.1016/j.msea.2020.140613.

(15) Aboulkhair, N. T.; Maskery, I.; Tuck, C.; Ashcroft, I.; Everitt, N. M. The Microstructure and Mechanical Properties of Selectively Laser Melted AlSi10Mg: The Effect of a Conventional T6-like Heat Treatment. *Materials Science and Engineering: A* **2016**, *667*, 139–146. https://doi.org/10.1016/j.msea.2016.04.092.

(16) MIL-HNDK-5J. http://everyspec.com/MIL-HDBK/MIL-HDBK-0001-0099/MIL_HDBK_5J_139/.

(17) EOS Aluminium AlSi10Mg Material Data Sheet. https://www.eos.info/03_system-related-assets/material-related-contents/metal-materials-and-examples/metal-material-datasheet/aluminium/material_datasheet_eos_aluminium-alsi10mg_en_web.pdf.

(18) Cao, S.; Zou, Y.; Lim, C. V. S.; Wu, X. Review of Laser Powder Bed Fusion (LPBF) Fabricated Ti-6Al-4V: Process, Post-Process Treatment, Microstructure, and Property. *gxjzz* **2021**, *2* (2), 1. https://doi.org/10.37188/lam.2021.020.

(19) Ti6Al4V AMS 6931 Datasheet. https://www.ssa-corp.com/documents/Data%20Sheet%20Titanium.pdf.

(20)   EOS Titanium Ti6Al4V Material Data Sheet. https://www.eos.info/03_system-related-assets/material-related-contents/metal-materials-and-examples/metal-material-datasheet/titan/ti64/eos_ti64_9011-0014_9011-0039_m290_mds_06-22_en.pdf.

(21)   Vrancken, B.; Thijs, L.; Kruth, J.-P.; Van Humbeeck, J. Heat Treatment of Ti6Al4V Produced by Selective Laser Melting: Microstructure and Mechanical Properties. *Journal of Alloys and Compounds* **2012**, *541*, 177–185. https://doi.org/10.1016/j.jallcom.2012.07.022.

(22)   Materialise Magics. https://www.materialise.com/en/industrial/software/magics-data-build-preparation?gad_source=1&gclid=Cj0KCQiAlsy5BhDeARIsABRc6Zsj-4-xWttbavPL7s0mP8ZsQT9MAgSwz1f-Dib8RFYcwLbrtJglEkMaAhosEALw_wcB.

(23)   Gan, M. X.; Wong, C. H. Practical Support Structures for Selective Laser Melting. *Journal of Materials Processing Technology* **2016**, *238*, 474–484. https://doi.org/10.1016/j.jmatprotec.2016.08.006.

(24)   EOS M270 Datasheet. https://www.eos.info/01_parts-and-applications/industry_different_parts_applications/metal_parts_applications/parts_metal_medical/dental/eos_m-270_dental_2017_en_web.pdf.

(25)   AMO Tool. https://amotools.com/login.

(26)   Kong, L.; Lei, W.; Han, J.; He, Q.; Li, Q.; Suorong, Z.; Wang, X.; Liu, Z. Analysis and Research on the Causes of the Inability to Use Pure Oxygen Dielectric Discharge Ablation Process on Titanium Alloy. *Int J Adv Manuf Technol* **2022**, *119* (9–10), 6103–6118. https://doi.org/10.1007/s00170-022-08691-6.

(27)   Standard Test Methods for Density of Compacted or Sintered Powder Metallurgy (PM) Products Using Archimedes' Principle. https://cdn.standards.iteh.ai/samples/116178/8a9dd339ec3142e8b86b5e4fc172c3fc/ASTM-B962-23.pdf.

(28)   Keller's Reagent Datasheet. https://www.metallographic.com/MSDS/SDS-OSHA/Kellers.pdf?srsltid=AfmBOopx1AtA8XFbv9_Ey8mIHBZc2aEmOnjyk1RKHwiMHUkPwYA4VKSk.

(29)   Kroll's Reagent Datasheet. https://www.metallographic.com/MSDS/SDS-OSHA/Krolls.pdf?srsltid=AfmBOooyxeJwI_3j59y-L2d2Cawtyq4GEnym8oRE52DtCKcuBAO3fjLd.

(30)   ASTM E 92-17 Hardness Test. https://cdn.standards.iteh.ai/samples/97184/2e9210f925ac4a208204d568be9f0a4a/ASTM-E92-17.pdf.

(31)   Ra, Rz Roughness. https://upmold.com/surface-finish-ra-rz/.

(32)   Zhang, P.; Li, S. X.; Zhang, Z. F. General Relationship between Strength and Hardness. *Materials Science and Engineering: A* **2011**, *529*, 62–73. https://doi.org/10.1016/j.msea.2011.08.061.

(33)   Rott, S.; Ladewig, A.; Friedberger, K.; Casper, J.; Full, M.; Schleifenbaum, J. H. Surface Roughness in Laser Powder Bed Fusion – Interdependency of Surface Orientation and Laser Incidence. *Additive Manufacturing* **2020**, *36*, 101437. https://doi.org/10.1016/j.addma.2020.101437.

(34)   Kempen, K.; Thijs, L.; Van Humbeeck, J.; Kruth, J.-P. Mechanical Properties of AlSi10Mg Produced by Selective Laser Melting. *Physics Procedia* **2012**, *39*, 439–446. https://doi.org/10.1016/j.phpro.2012.10.059.

(35)   Becker, T. H.; Dhansay, N. M. Influence of Porosity on the Fatigue Life of Laser Powder Bed Fusion–Produced Ti6Al4V. *Mat Design & Process Comms* **2021**, *3* (1). https://doi.org/10.1002/mdp2.141.

(36)   Standard Specification for Wrought Ti6Al4V ELI. https://cdn.standards.iteh.ai/samples/86555/d01525e23576401ba16e787b7326470d/ASTM-F136-13.pdf.

(37)   Limbasiya, N.; Jain, A.; Soni, H.; Wankhede, V.; Krolczyk, G.; Sahlot, P. A Comprehensive Review on the Effect of Process Parameters and Post-Process Treatments on Microstructure and Mechanical Properties of Selective Laser Melting of AlSi10Mg. *Journal of Materials Research and Technology* **2022**, *21*, 1141–1176. https://doi.org/10.1016/j.jmrt.2022.09.092.

(38)   Ghio, E.; Cerri, E. Additive Manufacturing of AlSi10Mg and Ti6Al4V Lightweight Alloys via Laser Powder Bed Fusion: A Review of Heat Treatments Effects. *Materials* **2022**, *15* (6), 2047. https://doi.org/10.3390/ma15062047.

(39)   A20X Datasheet. https://www.3t-am.com/sites/threeT/files/Aluminium%20A20X_Datasheet.pdf.

(40)   Elambasseril, J.; Benoit, M. J.; Zhu, S.; Easton, M. A.; Lui, E.; Brice, C. A.; Qian, M.; Brandt, M. Effect of Process Parameters and Grain Refinement on Hot Tearing Susceptibility of High Strength Aluminum Alloy 2139 in Laser Powder Bed Fusion. *Prog Addit Manuf* **2022**, *7* (5), 887–901. https://doi.org/10.1007/s40964-021-00259-2.

(41)   A2139 EOS Datasheet. https://www.eos.info/05-datasheet-images/Assets_MDS_Metal/EOS_Aluminium_Al2139AM/Material_DataSheet_EOS_Aluminium_Al2139%20AM_en.pdf.

(42)   Scalmalloy Carpenter Additive. https://www.carpenteradditive.com/hubfs/Resources/Data%20Sheets/Scalmalloy_Datasheet.pdf.